POLITECNICO DI MILANO

DEPARTMENT OF CHEMISTRY, MATERIALS AND
CHEMICAL ENGINEERING "GIULIO NATTA"

DOCTORAL PROGRAMME IN INDUSTRIAL CHEMISTRY
AND CHEMICAL ENGINEERING

NOVEL METHODOLOGIES FOR THE FLOW SYNTHESIS OF ORGANIC SCAFFOLDS

Doctoral Dissertation of:
Alessandra Sivo

Supervisor:
Prof. Dr. Gianvito Vilé

Tutor:
Prof. Dr. Valentina Busini

The Chair of the Doctoral Program:
Prof. Dr. Alessio Frassoldati

2023 – XXXV

Accepted on the recommendation of

Prof. Dr. Gianvito Vilé, examiner

Prof. Dr. Rafael Luque Alvarez de Sotomayor, co-examiner

Prof. Dr. Alessandro Trovarelli, co-examiner

If you tell me why the fen
appears impassable, I then
will tell you why I think that I
can get across it, if I try.
- Marianne Moore

Alle radici degli alberi di ulivo. Ai miei nonni.

Acknowledgments

"I misbehaved in the cosmos yesterday. I lived around the clock without questions, without surprise […]." *Distraction - Wisława Szymborska*

Towards the end of this long journey, I asked myself many times what I truly learned during my PhD. The answers are countless. But looking for one that is worth more than the others, I realized that the most important is the ability to ask questions (and to question oneself), for that is what makes us unique, driving us to learn, be critical, and improve ourselves.

For this, and many other things I learned throughout these years, firstly, I would like to thank my supervisor and mentor, Prof. Dr. Gianvito Vilé, for giving me the opportunity to be the first member joining his research group. I vividly remember the day in which prof. Luisi told me about this young professor that was going to come back in Italy after working abroad for a long time. Many years have passed from that day, but I think nobody knows, more than you, how many difficult situations we get through. Sometimes it seemed a never-ending challenge, and sometimes it was. Maybe for this reason I became the person I am today and I can't find the words to express my gratitude for all the support you give me during these years. I really appreciated the time you invested in my scientific formation, inspiring me to pursue my career. Once you told me that I should be proud of all the work I've done, and perhaps one day I will, but for now, your estimation is enough.

Finally, I would like to warmly thank my mom and my whole family, my friends, and all the people that during these years supported me, even when I did not deserve it.

Milan, July 21st 2023

Table of Contents

Summary

Continuous-flow manufacturing is an innovative approach that involves conducting reactions in a continuously flowing stream, using microreactors or microfabricated systems instead of traditional batch reactors. Here, reactants are continuously pumped into the microreactor, where they mix and react, and the product is continuously collected. This technology is radically changing the way to approach pharmaceutical and industrial organic chemistry. On one hand, the optimal performance of these kind of reactors paves the way for new possibilities from a chemical viewpoint (i.e., reactions that were not even considered as possible become now feasible); on the other hand, there is an indissoluble bond between this new technology and current themes related to process sustainability and circularity. In fact, flow processing improves mass and heat transfer and enhances mixing conditions, resulting in an increased reaction yield and productivity, with lower waste generation and cost consumption.

From a closer look at the scientific literature, it is possible to appreciate that in the past decades most continuous-flow methods have been developed for reactions in the liquid phase, often using homogeneous catalysts. Taking the steps from the gram-scale multistep synthesis of small molecules under flow conditions, the aim of this PhD thesis was to expand this technology further, developing the full potential of microreactor engineering in new and unprecedented directions. In this

context, this research has integrated multiple reaction steps for the synthesis of small molecules (i.e., azetidines, glycidyl derivatives, and trifluoromethylated pyrroles). Moreover, given the need to develop greener continuous methods that replace century-old, toxic, and expensive homogeneous catalysts, the thesis has also paid attention to the design of superior continuous-flow methods exploiting heterogeneous photocatalysts. In particular, we have studied the use of carbon nitride-based photocatalyst for organic transformations, focusing on the effect of catalyst nanostructuring on the reaction progress. These innovative heterogeneous catalysts are prepared from low-cost precursors, and have visible-light absorbing capabilities, excellent photostability, and tunable surface area.

The main limitation of traditional photocatalytic reactions is often the scale-up, mainly due to the less efficient light transmission in large batch reactors and the requirement of considerable amount of expensive metal-based photocatalysts. To bypass this challenge, we have investigated the design of novel polymeric photoreactor, functionalized with carbon nitride nanocatalyst ensures a uniform light distribution inside the reactor and ease process scale up.

All chemical reactions often require a purification step, which is often conducted using batch vessels. For this reason, the final purpose of this PhD thesis was to develop a flexible protocol for the *in-line* integration of flow synthesis and flow purification for applications in the end-to-end preparation of pharmaceutically-relevant small molecules.

The goal was achieved using continuous countercurrent chromatography simulating a "moving bed", involving the combination of sequential microreactors and twin-column system. The column loading method ensures that the product breaking through a fully loaded first column is loaded onto the second one, avoiding waste of precious material and technological complexity associated with the use of four-to-six columns typical of simulated moving bed chromatography. Compared to the discontinuous and other traditional approaches, our method leads to higher isolated yields (ca. +60%), higher productivity (ca. +30%), and reduced solvent consumption (ca. −80%). A circularity and life-cycle analysis (LCA) was also conducted to demonstrate the environmental benefits of the flow process. Overall, the protocol led to easier scalability and better suitability for industrial

applications, providing an additional tool for the design of sustainable manufacturing processes.

Sommario

La "chimica in flusso" è un approccio innovativo in cui le reazioni vengono condotte in un flusso continuo, utilizzando microreattori o sistemi in scala ridotta invece dei tradizionali reattori batch. Qui, i reagenti vengono pompati in modo continuo nel microreattore, dove si mescolano e reagiscono, e il prodotto viene raccolto in modo costante. Questa tecnologia sta cambiando radicalmente il modo di affrontare la sintesi farmaceutica e industriale. Da un lato, le prestazioni ottimali di questo tipo di reattori aprono nuove possibilità da un punto di vista chimico (ad esempio, reazioni che prima erano considerate impossibili diventano ora fattibili); dall'altro lato, c'è un legame indissolubile tra questa nuova tecnologia e i temi attuali legati alla sostenibilità e alla circolarità dei processi. Infatti, la chimica in flusso migliora sia il trasferimento di massa e calore, sia le condizioni di mescolamento, con conseguente aumento della resa e della produttività delle reazioni, riduzione della generazione di rifiuti e dei costi.

Da un'analisi approfondita della letteratura, è possibile apprezzare che, negli ultimi decenni, la maggior parte dei metodi a flusso continuo è stata sviluppata per reazioni in fase liquida, spesso utilizzando catalizzatori omogenei. Prendendo spunto dalla sintesi multistep su grande scala di piccole molecole, l'obiettivo di questa tesi di dottorato è stato quello di approfondire ulteriormente le applicazioni di questa tecnologia, sviluppando il pieno potenziale dei microreattori in nuove e inaspettate direzioni. In questo contesto, la ricerca ha integrato diversi step di reazione per la sintesi di piccole molecole (ad esempio, azetidine, derivati glicidilici e pirroli trifluorometilati). Inoltre, data la necessità di sviluppare metodi

in continuo più ecocompatibili, che sostituiscano i tradizionali sistemi catalitici omogenei, tossici e costosi, la tesi ha prestato attenzione alla progettazione di metodi in continuo che sfruttino fotocatalizzatori eterogenei di maggiore efficienza. In particolare, è stato studiato l'uso di fotocatalizzatori a base di nitruro di carbonio per trasformazioni organiche, concentrandosi sull'effetto che il design nanostrutturale del catalizzatore ha sull'andamento della reazione. Questi innovativi catalizzatori eterogenei, preparati a partire da precursori a basso costo, presentano capacità di assorbimento della luce visibile ottimali, eccellente fotostabilità e superficie regolabile.

La principale limitazione delle reazioni fotocatalitiche tradizionali è spesso la scalabilità, principalmente a causa della minore efficienza di trasmissione della luce nei grandi reattori batch, e della necessità di una considerevole quantità di costosi fotocatalizzatori a base di metalli. Per ridurre questo problema è stata studiata la progettazione di un nuovo reattore polimerico, funzionalizzato con nanocatalizzatori di nitruro di carbonio, che assicura una distribuzione uniforme della luce all'interno del reattore e facilita la scalabilità del processo.

Tutte le reazioni chimiche spesso richiedono una fase di purificazione, che spesso viene effettuata in batch. Per questo motivo, lo scopo finale di questa tesi di dottorato è stato quello di sviluppare un protocollo flessibile per l'integrazione degli step di sintesi e purificazione in continuo per applicazioni nella preparazione di molecole di interesse farmaceutico.

L'obiettivo è stato raggiunto utilizzando la cromatografia controcorrente in continuo che simula un "letto mobile", basato sulla combinazione di microreattori sequenziali e un sistema a doppia colonna. Il metodo di caricamento della colonna garantisce che il prodotto che attraversa completamente la prima colonna caricata venga caricato sulla seconda, evitando sprechi di materiale prezioso e la complessità tecnologica spesso associata all'uso di quattro o sei colonne, tipici della cromatografia a "letto mobile". Rispetto agli approcci discontinui e ad altri approcci tradizionali, il nostro metodo consente di ottenere rese isolate più elevate (circa +60%), maggiore produttività (circa +30%) e minor consumo di solvente (circa -80%). È stata anche condotta un'analisi di circolarità e di valutazione del ciclo di vita (comunemente noto come LCA) per dimostrare i benefici ambientali

del processo in flusso. Complessivamente, il protocollo ha permesso di ottenere una maggiore scalabilità e una maggiore idoneità per applicazioni industriali, fornendo uno strumento aggiuntivo per la progettazione di processi di produzione sostenibili.

Chapter 1

Introduction

1.1.   The Continuous-Flow Technology

Chemists and chemical engineers have seen over and over the emergence of technologies that promised to modernize materials and process development (e.g., parallel and combinatorial chemistry, microwave synthesis, computational methods). These technologies have often failed in the transition from the research lab to the industrial world, as they did not provide significant improvements in the way we perform chemistry. On the other hand, over the past 15 years, chemists around the world have demonstrated remarkable potential in the use of continuous-flow reactors for chemical synthesis and in the transition from batch to flow processes in manufacturing.[1–4] Even though fine chemical processes are often carried out in batch pilot plants (particularly when the production volumes are small, as in the case of pharmaceuticals and agrochemicals), flow chemistry has forced the industries to rethink their processes and consider this technology as a real and meaningful alternative to standard practices. As a result, pharmaceutical
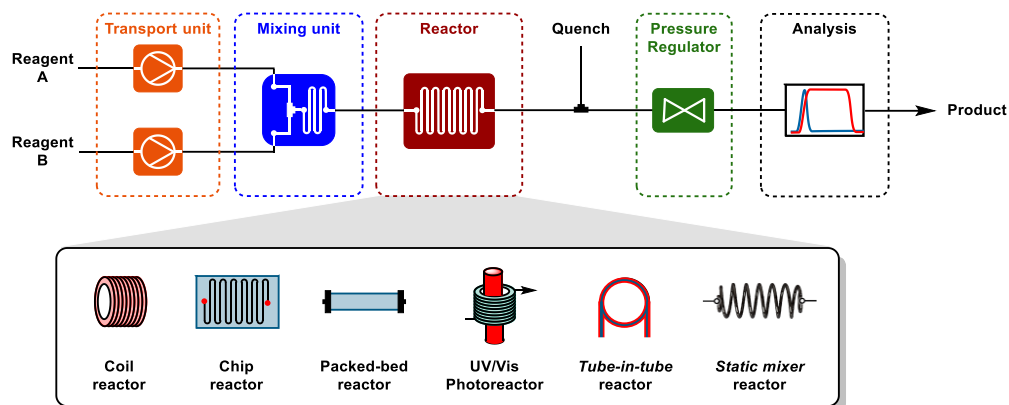
Figure 1.1. *General scheme of a flow chemistry setup.*

companies have been the first to take steps towards the implementation of flow chemistry, also driven by the need to reduce their environmental impacts, increase process safety, and modernize their facilities. Flow chemistry is the technique that enables carrying out standard reactions in continuous-flow mode (Figure 1.1), using microreactors (such as a coil or a chip reactor).[5] These are small-volume flow cells that are optimized for the continuous and consistent production of a target compound.

Their volumes and channels can range from microliter to mesoliter scale and are thus optimal for pharmaceutical and biomedical manufacturing. More specifically, in a flow reactor, the components are pumped together in a mixing junction and flow through a temperature-controlled unit where the reaction takes place.[6] Compared to batch processing, continuous-flow systems offer several advantages such as more efficient mixing schemes, rapid heat and mass transfer, and increased safety.[7,8] Moreover, a temperature range between −80 °C and 250 °C and a pressure range of 1–10 bar represent the conventional limits in traditional synthetic chemistry.[9–12] In flow mode, significantly higher temperatures (up to 500 °C) and pressures (100 bar) are possible, and alternative heating methods (such as inductive, microwave, and flash heating) have been developed to attenuate the sensitivity of molecules at severe reaction conditions. This permits the use of solvents above their boiling points, at supercritical conditions. It also allows process intensification, which leads to lower operation, maintenance, and capital expenditures as well as increased modularity and minimized physical footprints.[13]

Flow chemistry represents one of the key enabling technologies that have brought sustainability into drug discovery and drug manufacturing. Within the past ten years, this technology has found applications in the whole pharmaceutical value chain, from compound libraries in drug discovery[14] to chemical development and drug delivery.[15] One of the most exciting ways in which flow chemistry has positively impacted drug discovery is through the exploitation of new and previously unexplored chemical space. This includes chemical reactions that were previously considered out-of-scope in organic synthesis laboratories due to safety concerns (e.g., carbonylation or halogenation).[7,8] In addition, flow chemistry has simplified the scalability of scaffolds and building blocks and improved reaction yields, significantly supporting medicinal chemistry programs during initial hit-to-lead phases.[16–20] At process scale, flow chemistry has enabled the rapid synthesis of active pharmaceutical ingredients (APIs) by the integration of multiple reaction and purification steps into one single cascade. The entire synthesis of drugs could be automatized, and multicomponent reactions could be performed by introducing reactants at any point in the flow path.[21,22] More recently, the possibility to synergistically combine reaction, purification (for example, through a series of immobilized scavengers and crystallization units), and formulation steps has assisted in the generation of integrated refrigerator-sized platforms capable of producing hundreds of individual doses of APIs within 24 h.[23] It has been proposed that such compact chemical miniplants will provide opportunities for the regional synthesis of pharmaceuticals and agrochemicals in developing economies based on the needs and demands of each country, opening unforeseen avenues for drastic changes in local commercial manufacturing. Finally, due to the possibility to quickly implement in-line spectroscopic process analytical technology (PAT) tools to monitor continuous campaigns, it has been shown that chemical runs often exceed standard quality assurance specifications, providing a proof that the technology is eminently suitable for the efficient manufacturing of pharmaceutical products.[24] It is not surprising that in February 2019, the US Food and Drug Administration (FDA) has released a new Good Manufacturing Practice draft guideline,[25] encouraging and fostering the use of flow chemistry to modernize and accelerate manufacturing lines, reducing

material handling, allowing better process control, and building quality-bydesign (QbD) into the complete product life cycle. Finally, for clinical phase I, II, and III, the excellent mixing and heat transfer of microreactors have allowed the production of kilogram-quantities of the material in a very straightforward manner. Based on the multiple advantages above, pharmaceutical giants have readily adopted this technology. GSK, for example, has invested over 95 million USD to build two continuous manufacturing facilities in Singapore. The hypoxia-inducible factor (HIF) prolyl-hydroxylase inhibitor daprodustat (GSK1278863) will be the first drug to be manufactured under a continuous-flow regime.[26] The company has also an ambitious target of one third of its API portfolio being produced in flow regime within 2030.[27] Eli Lilly was the first to synthetize kilograms of a cancer drug candidate (prexasertib) under continuous-flow conditions in 2017.[28] Later on, in 2019, the company was awarded for their small-volume continuous facility located in Kinsale, Ireland.[29] Companies such as Syngenta, Novartis,[30] Sanofi,[31,32] AstraZeneca,[33] and Johnson & Johnson[34] are also incorporating continuous manufacturing strategies at various stages.

There are, however, sectors other than pharmaceutical, which can benefit from continuous manufacturing, and where the advantages of flow chemistry and microreaction engineering have not yet deeply infiltered. Smart and functional materials such as biomedical nanoparticles, electronic nanostructures, and heterogeneous catalysts (even those used for pharmaceutical manufacturing) are often prepared in batch mode, using deposition–precipitation, impregnation, colloidal, or hydrothermal methods. This leads to broad particle size distributions, which affect the possibility to discriminate the intrinsic material behavior due to the lack of structural uniformity. The adoption of flow chemistry in the synthesis of nanoparticles and catalysts allows a novel process control window.[35,36] Circular chemistry is another sector which could benefit from the progress made in the flow processing arena. For example, we envision the use of carbon dioxide and other 'waste' molecules as an alternative feedstock for chemical processes. From these 'waste' materials, useful products can be made under flow conditions, including plastics and pharmaceutical building blocks. In this subfield, we can consider as well the efforts of those developing continuous-flow processes that make use of

bio-based starting materials.[37,38] For example, the Australian Licella Pty Ltd has devoted the equivalent of 75 million USD for the development of a circular continuous-flow platform (Cat-HTR™) to convert non-food biomass residues into biocrude oil.[39,40] The Norwegian Steeper Energy named their continuous hydrothermal liquefaction plant as Hydrofaction™ and a project worth 59 million USD was recently announced.[41–43] A continuous pilot plant to convert municipal waste into oil with a productivity of 700 kg per day has been announced by the Italian oil-and-gas multinational ENI. The bio-oil can be obtained in a range of 3–16% depending on its constituents.[44,45] Further to the hydrothermal liquefaction process, commercial continuous pilot plants for pyrolysis can also be found.[46,47] Most of these industrial studies are, however, still at the infancy stage.[48,49] Bearing this in mind, this review analyses the key achievements to date in adopting continuous-flow technologies in new, key research areas, including circular synthesis and material manufacturing, critically highlighting current challenges and future directions. We devote a significant emphasis to demonstrate the enhanced characteristics of products prepared under continuous-flow mode (compared to standard batch technologies). Moreover, we discuss the novel opportunities given by automation and 3D printing in translating traditional methods into flow mode.

1.2. Continuous Synthesis for Circular Chemistry

A circular economy is a systemic approach to development designed to benefit society, companies, and the environment. In contrast to the linear 'take-make-waste' model, a circular economy aims at gradually decoupling growth from the consumption of finite resources. Circular chemistry goes hand in hand with circular economy, as it focuses on the sustainability and life cycle of chemical processes. Similar to green chemistry, twelve principles have been coined to define circular processes, and these are detailed in Table 1.1.[50,51] It is immediate that flow chemistry, as an enabling tool with unprecedented potential, can meet all of the goals of circularity. For this reason, this section reviews recent literature examples where continuous processes have been employed to recover chemicals, convert 'waste' materials, and use 'biobased' reactants. Vanraes and co-workers

Table 1.1. The 12 principles of circular chemistry.

Principle	Definition	Application to flow chemistry
i	Collect and use waste.	Develop continuous processes that employ 'waste' materials as reagents.
ii	Maximize atom circulation.	Recover precious compounds (*i.e.*, C, N, Cl, I, Br, transition metals) from the 'waste' and recycle them.
iii	Optimize resource efficiency.	Maximize use of raw materials in flow-mode, reducing costs.
iv	Strive for energy persistence.	Develop continuous processes with low energy requests and use, if possible, renewable energy sources.
v	Enhance process efficiency.	Enhance reaction yield by developing optimal reactor geometries.
vi	No out-of-plant toxicity.	Ensure no generation of toxic compounds after reaction. Minimize byproduct formation. Prepare and use in-situ toxic compounds.
vii	Target optimal design.	Optimize flow processes.
viii	Assess sustainability.	Design continuous processes in which the reduction of pollutants, solvents, and energy consumption leads to environmental and economic benefits.
ix	Apply ladder of circularity.	Reuse reactor and reaction components which are still in good condition and fulfils their original functions, avoiding discharging.
x	Sell services, not products.	Support the process industry developing flow chemistry roundtable and services to expand the adoption of these technologies.
xi	Reject lock-in models.	Ensure machine integration and exploit systems capable of standardization.
xii	Unify industry and provide coherent policy framework.	Exploit potential of integrating several concepts together, for example preparing catalysts and polymers for synthesis and manufacturing also in continuous mode.

recently reported a new process for the removal of alachlor in water by non-thermal plasma, making a comparison between the removal efficiency and reactor performance for the recirculation method and single pass mode (referring to the ozonation process).[52] Oehlmann and co-workers studied the enzymatic degradation of hormones and endocrine disrupting compounds (EDCs) in wastewater using fungal-derived laccases.[53] In their study, immobilized laccase was stacked in a column and subjected to a continuous flow of wastewater. The system was able to remove EDCs impurities with high leaching resistance and the

activity and mechanical stability of the immobilized laccase was better compared to the 'free' enzyme. The exploitation of CO_2 as a reactant is also important for circular flow applications. Carbon dioxide may be used as C1 feedstock for both organic synthesis and fuel engineering, resulting in several important products such as CO, CH_4, methanol, olefins, hydrocarbons, higher alcohols and others.[54] CO_2 hydrogenation is currently a major topic of research, with the aim of generating syngas (CO/H_2) for organic synthesis or C_2H_4 for polymer and fuel production.[55] Ren et al. reported a selective electrochemical method for CO_2 reduction to CO mediated by cobalt phthalocyanine in a flow electrolyzer, achieving > 95% CO selectivity.[56] Jeng and Jiao developed a single-pass CO_2 conversion in a flow electrolyzer, composed of silver nanoparticles as cathode and iridium oxide as anode. The authors attained a gas steam from the cathode containing approximately 80% CO, 15% H_2 and 5% unreacted CO_2; the product steam was then used as syngas for organic synthesis.[57] Another example is the upgrade of epoxides to carbonates in the presence of CO_2. Bui et al. prepared a novel mesoporous melamine formaldehyde resin as heterogeneous catalyst for cyclic carbonate synthesis in flow regime. The authors obtained carbonates in yields that varied from 76% to 100% at 120 °C and 13 bar, under solvent-free and catalyst-free conditions. The flow method demonstrated as well excellent recyclability and stability for more than 13 days of continuous run.[58] The above-mentioned examples highlight the practicality of taking advantage of waste chemicals and converting them into new marketable products. Along these lines, Browne and co-workers demonstrated the valorization of food waste by the metathesis reaction of cocoa butter triglyceride under a flow regime.[59] The targeted compound, 1-decene, is a widely used intermediate in the manufacture of surfactants. A tube-in-tube gas–liquid flow reactor was employed to deliver ethylene for the ethenolysis reaction of triglycerides containing mainly the alkene oleic acid. Yields up to 41% for 1-decene were reported. One of the major drawbacks in carbohydrate chemistry is the formation of humins, an alternative 'waste' compound. These species are commonly formed during the acid-catalyzed hydrolysis of C5–C6 sugars and result in a lower process efficiency. In a pioneering contribution, Luque and co-workers demonstrated that humins could

be valorized in flow mode by extraction of its components, such as 5-methoxymethylfurfural (MMF).[60] MMF was first obtained from humin by column chromatography and was subsequently hydrogenated to produce tetrahydrofuran derivatives in continuous mode using a packed-bed reactor containing 5% Ru/C and 5% Pd/C as catalysts. Biomass research fits nicely with several principles of circular chemistry. For example, biomass is an unlimited source of organic carbon due to its renewable character (principle iii). Carbon dioxide released by its combustion is balanced by the amount of CO_2 consumed during biomass growth (principles i and ii), meeting the United Nations Sustainability Goal of zero waste. Thus, biomass conversion can play a central role in the development of a circular flow platform. From a chemical perspective, lignocellulosic biomass is a polymeric material mostly composed of three primary units: (i) cellulose (a crystalline polymer made up of glucose units; (ii) hemicelluloses (amorphous polysaccharides composed of C5 and C6 units); and (iii) lignin (a three-dimensional polymer made up of coumaryl, coniferyl, and synapyl alcohols). From these compounds, a series of valuable chemicals can be obtained by physical, chemical, or biological transformations.[61,62] While biomass can be directly converted into a mixture of pyrolysis oil or syngas through high-temperature, unselective thermochemical processes, their components (i.e., lignin, cellulose/hemicellulose, proteins, and salts) can be separated only via physical, chemical, and biological treatment. Physical delignification produces aromatic compounds from lignin, hydrolysis converts cellulose/hemicellulose into C5–C6 sugars, and protease enzymes degrade proteins into amino acids. Finally, the obtained aromatic rings, C5–C6 sugars, and amino acids can be chemically or biologically transformed into a diversity of chemicals.[63–68] In this perspective, syngas was used by Kappe and coworkers for the synthesis of aryl aldehydes by formylation of C6 sugars under a flow regime.[69] The process was run in a gas–liquid segmented flow regime and 17 examples were demonstrated using (hetero)aryl bromides as starting materials. The optimized condition required 1 mol% $PdCl_2$, CO/H_2 in a ratio of 1:3, a reaction temperature of 120 °C, and a residence time of 45 min. One of our groups recently demonstrated the synthesis of monomers from biomass derivatives under a flow regime.[70] Using terpenes as

staring materials, a small library of saturated and unsaturated monomers was produced in excellent yields (up to 96% for two steps). The process was composed of two steps and started with a Diels–Alder reaction followed by catalytic hydrogenation using a tube-in-tube reactor in a recycling system. Scale up was also demonstrated and, using α-terpinene as starting material, 10.6 g of terpene were prepared over 3 h (3.53 g h^{-1}) in the first step and 10.15 g over 16 h (0.634 g h^{-1}) in the second step. Many other strategies have been developed in flow for the synthesis of fine chemicals from biomass or its derivatives.[71] For example, lactic acid can be converted into a series of compounds including 2,3-pentanedione, propanoic acid, lactamide, and acrylic acid. Glycerol can be transformed into glycolic acid, nitroglycerine, dihydroxyacetone, acetol, propene, and epichlorohydrin. Glucose into gluconic acid, 5-HMF, and sorbitol. Furfural into N-heterocycles. Several other bio-based starting materials can be precisely converted into valuable chemicals.[72–76] Several organic transformations can be mediated as well by biotechnological tools, such as biocatalysts. Biocatalysis is considered a green technology for organic synthesis due to its high activity and selectivity under mild conditions.[77–80] For this reason, flow biocatalysis has been growing as a trend over the years and, probably, flow chemistry will help in the wider adoption of biocatalysis by the synthetic organic chemistry community. The implementation of enzymes and/or whole cells in flow regimes relies on their immobilization, regardless of whether the method to do so is based on physical adsorption or chemical binding.[81] Weiser et al. reported an advanced sol–gel system for the immobilization of lipases, the most used enzyme in organic synthesis due to its ability to catalyze a wide range of reactions, such as esterification, transesterification, hydrolysis, aminolysis, and polymerization.[82] Remarkably, using just 1 g of native Candida antarctica lipase entrapped on a silica-based resin, 2.2 kg of product in the alcohol kinetic resolution with high enantiomeric purity (99.4% *ee*) and 3.3 kg of product in the amine kinetic resolution, also with high enantiomeric purity (99.8% *ee*), were successfully obtained. Similarly, Britton and co-workers reported a vortex fluid device to drive formation of thin films that can be applied in multi-step transformations, such as biocatalysis and protein purification, in a single reactor.[83] The authors used a fused

histidine tag for purification through complexation with an immobilized metal affinity chromatography bed. Firstly, the reactor was eluted with Ni^{2+} to charge the resin. Next, the protein solution entered the flow system for purification. After that, residual Ni^{2+} was washed out with a phosphate-buffered saline solution. The reactor was eluted with imidazole for protein recovery or used directly for the biocatalytic transformation. To demonstrate the ability of multi-step biocatalysis, the authors reported a two-step production of *p*-nitrophenoxide from bis(*p*-nitrophenol)phosphate mediated by phosphodiesterase and alkaline phosphatase. The reactor division into stripes allows rapid substrate transformation with less product inhibition due to the proximity of the different sections. Cofactors play an important role in enzymatic bioreactions; however, the recycling of cofactors is often a drawback, making bioredox reactions difficult for industrial operation. Velasco-Lozano et al. developed a methodology for cofactor and enzyme immobilization for a self-sufficient heterogeneous biocatalysis.[84] The main enzyme was immobilized on agarose microbeads activated with aldehydes followed by polyethyleneimine (PEI) coating (step 1). The recycled enzyme was co-immobilized by ionic adsorption on PEI and cross-linked with 1,4-butanediol diglycidyl ether for irreversible attachment (step 2); the cofactor was then adsorbed to the cationic bed (step 3). Under an optimal asymmetric reduction flow rate (50 μL min^{-1}), the reactor worked for 92 h with a ketone conversion higher than 90% and the corresponding alcohol was obtained with high enantiomeric excess (>99% *ee*) without lixiviation of the cofactors. The examples prove that by carrying out enzymatic reaction on a fixed-bed system, several advantages are possible, including avoidance of toxic and rare/abundant transition metal catalysts and easier separation of the reagents/products from the biocatalyst. However, there are also some unsolved challenges. For example, the enzyme often loses considerable activity after immobilization. Complications with enzyme leaching and denaturation in organic solvents also pose some limitations in some transformations. Another challenge is their specificity, making them unsuitable for broad substrate scope screenings. Despite these challenges, flow biocatalytic methods will continue to play an important role in increasing process efficiency and reducing carbon dioxide emissions into the environment, and we expect that

these tools will be complementary to more traditional synthetic methods to recover materials from water and valorize CO_2 and waste chemicals in order to obtain value-added compounds for a fully circular economy.

1.3. Lessons Learned

Now that we enter into a new decade of research needs, new (old) technical challenges might come back: how to we translate batch methods into flow mode to meet the standards of circular chemistry? How do we perform nanomaterial manufacturing avoiding channel blockage? Is there a general method to select optimal reactor and pumping systems? To address these questions, it is important to review what a decade of flow chemistry research has taught us. Hence, this section summarizes the key lessons and main technological solutions to the different problems encountered over the years.

The importance of kinetics. Understanding the kinetics of a reaction (this being the circular synthesis of chemicals, a polymerization step, or the manufacture of NPs) is critical for the determination of the reaction mechanism and for the subsequent optimization process. Based on kinetics, reactions that would benefit from continuous conditions can be classified into three categories: flash reactions (where the kinetics is in the order of a few fractions of seconds), fast reactions (where the kinetics requires between 1 and 15 min), and slow reactions (taking longer than 15 min but suffering from dangerous conditions). Within the first group (flash reactions), we have learned that we can carry out ultrafast methods with reaction time of less than one minute due to the possibility of controlling in a very precise manner the reaction time. Such reactions are typically difficult (or even impossible) to conduct in batch mode. For example, Vilé and coworkers reported a continuous-flow synthesis of 2-methylproline and derivative using a substituted D-alaninate as a starting material and LiHMDS as a base.[85] Both reagents were pumped at a flow rate of 1 mL min^{-1} into a cryogenic unit kept at -10 °C, with a total residence time of 30 s. Luisi and Nagaki provided another proof of flash technology and, by control of the residence time in a

microflow reactor, they generated reactive intermediates and quickly used them before their natural decomposition.[86] Fluoroiodomethane, in this case, reacted with MeLi in the first mixer, generating fluoromethyllithium, whose lifetime is typically within the order of a few milliseconds. This highly unstable intermediate reacted with an electrophile in a setup featuring a total residence time of 13 milliseconds and very low temperature ($-60\,°C$). Finally, Takeda Pharmaceuticals developed a process for the synthesis of TAK-117, a selective PI3Kα isoform inhibitor.[87] In this case, both the lithiation and the borylation are ultra-fast steps and were conducted in microreactors with a yield of more than 85%. Within the second group, we have rapid reactions whose residence time is between 1 and 15 min. Here, flow chemistry can be applied due to the better control of the mass and heat transfer. In this regard, we want to highlight the example from Mitsuda and co-workers, who developed a continuous-flow synthesis protocol for a N-carboxy anhydride, a key intermediate for the synthesis of the antihypertensive drug imidapril, using phosgene as a building block, with a residence time $\tau = 3$ min.[88] This procedure not only allows an optimal reaction yield but also prevents safety issues bound to phosgene toxicity. Continuous-flow approaches could also be useful to carry out slow or very slow reactions, with $\tau > 15$ min, when the reaction involves hazardous reagents or dangerous gases (*e.g.*, H_2, CO, phosgene, etc.). These gases could be safely prepared and consumed in situ under flow conditions. Examples of transformative flow applications of hazardous reactions include high-pressure hydrogenations,[89–91] fluorinations,[31,92] carbonylations,[93] syntheses of unstable azides[94] and their exploitation in heterocycle synthesis.[95]

The importance of pressure. Differently from batch reactors, flow systems can be easily pressurized, working at supercritical solvent conditions. This is possible using a back-pressure regulator typically applied near the exit of the stream. In 2016, Monteiro et al. developed a continuous-flow synthesis of the hydantoin scaffold, whose major challenge was the solubility of the starting materials and the formation of explosive gaseous bubbles as a result of reagent evaporation.[96] These issues were solved in flow mode by using back-pressure regulators of 20 bar total pressure to avoid evaporation and keep the reagents in solution.

The importance of 'solution–diffusion'. Reactions involving heterogeneous gas–liquid mixtures (such as those employing 'waste' CO_2 as a reactant) could be conveniently carried out in tube-in-tube reactors. These peculiar reactors are made of two tubular channels, one inside the other, separated by a polymeric membrane. Common membrane polymers are cellulose triacetate, polyisoprene, polycarbonate, polystyrene, polysulfone, and polytetrafluoroethylene (Teflon). In tube-in-tube reactors, the gas phase can thus flow in the external tube (conventional tube-in-tube configuration, Figure 1.2 a) or in the gas-permeable internal tube (reverse tube-in-tube reactors, Fig. 1.2 b).[97–99] In both cases, the working principle of these membranes is called 'solution–diffusion', since the solute (the gas) dissolves in the polymer (solution) and moves then through the polymer chain gaps (diffusion). Kappe and co-workers used a tube-in-tube reactor for the generation, separation, and usage of anhydrous diazomethane in a continuous-flow process.[100] The gaseous diazomethane was generated in the inner gas-permeable tube, permeated outside through the membrane, and reacted with the other substrates in the liquid phase. Similarly, O'Brien, Ley, and Polyzos developed a continuous-flow process for the CO-mediated methoxycarbonylation reactions, using a tube-in-tube reactor with Teflon AF-2400 tubing.[101] The utility of this reactor configuration was proven by the possibility to safely handle hazardous gases like CO, making it an ideal carbonyl source in C–C bond formation reactions.

The importance of mixing. Many important reactions within the field of circular chemistry and material manufacturing are affected by mixing. Typically, the fluid dynamics in microreactors is laminar, with a Reynolds number of less than 2300; hence, mixing occurs by diffusion. In the case of biphasic reactions, when the reagents are immiscible liquids or we have a suspension, mixing can be improved, creating local turbulent conditions using micromixers. Static micromixing structures increase mass transfer, allowing turbulent flow conditions. Multilamination of streams in a channel with corrugated walls increases the contact surface of lamellar streams and leads to fast mixing. There are a lot of configurations for static micromixing structures, like tangential, SZ shaped, and caterpillar (Figure 1.3). Reactors with static mixers can also be 3D-printed with

the possibility to obtain intricate details in mm-sized channels. Blacker and Jolley reported a continuous-flow synthesis of N-chloro-N,N-dialkylamine solutions in a nylon–PTFE tubular reactor, presenting static mixers that improved phase transfer between biphasic solutions.[102] Both organic and aqueous phases were pumped simultaneously with equal flow rates into a T-mixer, forming a well-
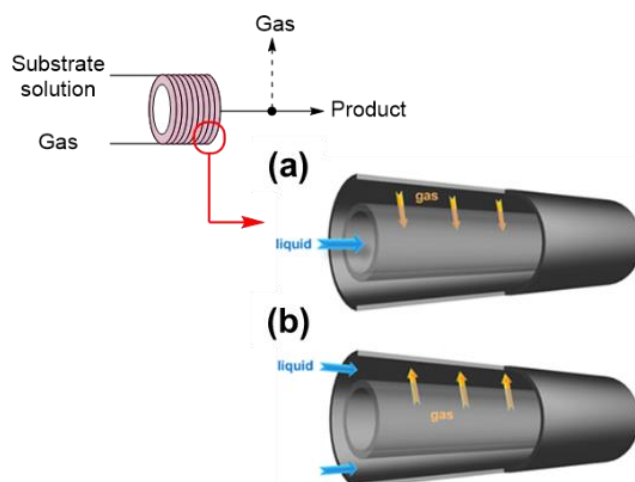
Figure 1.2. Structure and function of tube-in-tube reactor configurations.
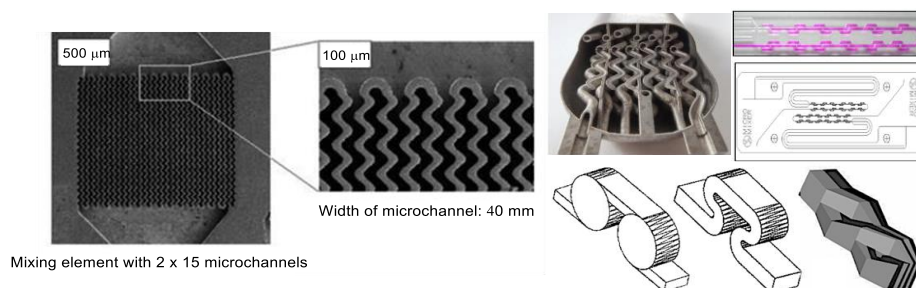
Figure 1.3. Details and 3D-models of conventional static micromixing structures.

mixed emulsion as long as solutions flow into the static mixers and rapidly separate shortly after emerging from the mixing region. Such configurations could find useful applications in polymerizations.

The importance of selecting the right pump. The assembly of a flow process for a specific reaction is strongly affected by the choice of the pumping system, which provides a continuous stream of reagents and avoids clogging of the system. The choice of the pump depends not only on the operating pressure, temperature,

and flow rates but also on the volumes that must be injected and the features of the substances that must be pumped (*i.e.*, viscosity and chemical compatibility among others). There are several types of pumps, and these are typically classified into three macrogroups: reciprocating pumps, rotary-type pumps, and pneumatic pumps. Among reciprocating pumps, there are piston (syringe) pumps that have been widely used in the past and are still used in more than 90% of all chemical processes. They consist of a small chamber in which substances are pumped by the back/forth motion of a motor-driven piston made of inert material like ceramics or stainless steel. These types of pumps can operate at high output pressures (up to 10 000 psi) and ensure constant flow rates, but they are not suitable for emulsions and slurries. Among the rotary types, we have peristaltic pumps. These units are suitable for a broad range of fluids, including viscous materials that cannot be pumped by common pumps; they also enable contamination-free fluid transfer. Peristaltic pumps are positive displacement pumps in which the fluid passes through a flexible tube fitted inside a circular cavity. In this chamber, rollers rotated by suitable motors push the fluids through the tube by physically compressing it. Differently from every other system, these pumps can be used for slurries, but the common issues are pulsations and limitations with reaching flow rates over 10 mL min^{-1}.[103] Pneumatic pumps, which use compressed air to create force that is used to move fluids through a piping system, are not often used to process fluids in flow microreactors.

The importance of novel process windows. The use of flow technologies has provided a platform for the resurgence of interest in photochemistry and electrochemistry due to a more efficient energy transfer within the narrow reaction channels.[104–109] This is allowed by the easy modularity and the possibility to obtain customized reactors for every kind of reaction, solving the low homogeneity of reaction conditions, and opening up a whole range of novel and scalable transformations for the bench chemist. Examples include, among others, cycloadditions, C–C couplings and alkylations via photoredox catalysis in flow regime, and the electrochemically driven formation of sulfonyl fluorides, sulfoxides, and sulfones.[105,106,110–112] We expect that in the near future such methods can also be implemented to recover waste chemicals (such as H$_2$S) and

obtain polymers and new nanocatalysts via photochemical and electrochemical routes.

1.4.   Current Challenges in Continuous-Flow Chemistry

Despite all the above-mentioned advantages resulting from the use of flow technology, there are still some limitations that restrict its widespread industrial utilization, mostly related to the processes scale-up and lack of availability of flow equipment. Firstly, the introduction of new methodologies in manufacturing plants has always been difficult, due to the batch mind set, still tied to the conventional established batch protocols. Despite this attitude, the use of flow technology has been strongly supported by several international agencies (like the United States Food and Drug Administration and the European Medicines Agencies), as well as from the evident economic benefits. Life cycle assessment (LCA)[113] studies conducted by comparing batch and flow conditions for the same process show that, besides the traditional advantages deriving from the transition to a flow protocol, the implementation of this new methodology can positively affect the throughput of a single process, *e.g.* by increasing the catalyst recyclability or by reducing the required amount of the same.[114–117] Also, in some multistep synthesis, the no longer needed intermediate isolation resulting from the increased selectivity for the target products, prevent time and solvent consuming purifications, as well as the storage of large amount of toxic or hazardous intermediates, with consequent benefits in terms of safety, sustainability, and costs.[118]

The expensive commercial flow equipment forced chemists and chemical engineers all over the world to fabricate their own chip homemade set ups, with tailored features for each process, leading to a lack in availability of commercial devices for specific applications.[119–121] Among these applications, it's worth to cite the scale up under flow conditions, particularly in photocatalytic processes, in which the reactor parameters need to ensure equal flow distribution, mixing efficiency, and uniform light penetration.[122] The failure to improve commercially available devices for a largest number of applications limits the integration of flow technology with several other chemical fields, such as heterogeneous catalysis, whose benefits are well-established in the entire scientific community.[123,124]

Besides the use of static micromixing structures, already discussed in the previous paragraph, the main strategies rely on the increase of channels diameter[125] and the use of continuous stirred-tank reactors (CSTRs),[126–128] that negatively affect heat and photon transfer. A different innovative approach consists in fixing the catalyst on a surface, as for packed-bed configurations,[129,130] coated microchannels,[121,131] and structured reactors.[132,133] Beyond the classical drawbacks, such as scalability, (homemade) reactor assembly, and efficient catalyst use, the main advantages of this approach are the increased heat transfer, the optimal light distribution, and the easy catalyst recovery and recyclability, leading to an improvement of the process sustainability.

Finally, the flow integration of all the downstream operations is still a crucial challenge to be faced. Some examples of sequential flow work up steps have been reported, in which the potential decrease of required time and optimal product recovery have been demonstrated.[134–136] Nevertheless, the incorporation of these purification units in manufacturing plants is still not widespread, due to the limited number of investigations conducted so far.

1.5. Aim of the Thesis

The general goal of this work is to address these challenges and develop new methods for the flow synthesis of organic scaffolds. The integration of continuous-flow chemistry with several other techniques, namely photocatalysis, nanostructured reactor design, and downstream purification has expanded the scope of this thesis, paving the way for more efficient applications in thermo- and light-driven chemical processes under flow conditions.

1.6. Outline of the Thesis

The scientific results of this thesis are presented in six scientific chapters (**Chapters 2-7**), followed by the Conclusions and Outlook (**Chapter 8**).

The thesis starts with the investigation of multistep non-catalytic processes, with the goal of identifying a general strategy for the development of efficient flow conditions. The key role of continuous-flow technologies to affect the kinetics of a reaction and make synthetic protocols ultrarapid and more efficient was

demonstrated in **Chapter 2**, where a rapid flow process for the on-demand synthesis of azetidinium salts is described. These compounds are important motifs in organic synthesis but are difficult to obtain in large scale due to extremely long synthetic protocols. A systematic comparison between batch and flow conditions enabled us to verify that the use of a flow reactor leads to a better control of mass and heat transfer during reaction.

A similar approach was used in **Chapter 3**, in which the telescoped and gram-scale flow synthesis of gycidol is presented. The study was then extended to producing further functionalized derivatives, with potential applications in the field of medicinal chemistry and polymer science. This work highlights once again the potentiality of continuous-flow chemistry to revolutionize organic synthesis.

Since the integration of continuous-flow technology with heterogeneous photocatalysis has emerged as one of the most promising strategies to develop sustainable processes, the next part of this thesis focuses on the design of visible light-driven catalytic processes. A rapid and simplified continuous-flow method for the trifluoromethylation of a variety of functionalized heteroaromatics, which have numerous applications in the pharmaceutical and fine chemical industries, is presented (**Chapter 4**). In this chapter, the role of carbon nitride nanostructuring on the catalytic performance was elucidated, unlocking the interplay between physicochemical features of photocatalysts used in this process and the corresponding effects on the reaction, and using it to design a continuous-flow process that maximizes catalyst–light interaction, facilitates catalyst reusability, and enables intensified reaction scale-up.

Chapter 5 reports the outstanding performance of an innovative catalytic formulation, known as "single-atom catalysts", with a superior metal utilization compared to conventional metal-based catalysis. In this study, the effectiveness of an Ag-based single-atom catalyst in promoting the direct photocatalytic oxidation to benzoic acids, using visible light and in the absence of ligands or organic additives, was shown. The results demonstrate promising potential for the continuous-flow synthesis of the target benzaldehyde, which is also a building block for biomass valorization.

In the search for less conventional reactor design, **Chapter 6** discusses the

design and preparation of a new class of solid polymeric material, by combining structured carbon nitride with a polymeric material. The fabricated catalytic material has been extensively characterized with physico-chemical methods to obtain important information on its structure and properties and has shown outstanding performance towards several flow photocatalytic processes.

Chapter 7 extends the acquired knowledge to the integration of flow chemistry with in line chromatography. It involves the integration of sequential microreactors with a twin-column counter-current chromatography system that utilizes commonly employed C18 columns. The loading technique employed in the columns ensures that the product, after saturating the first column, is subsequently introduced into the second column. Thus, this strategy prevents the wastage of valuable materials and mitigates the technical complexity typicallt associated with the usage of a larger columns number. The system was employed to synthesize biphenyl via Suzuki–Miyaura reaction and was also demonstrated for other structurally-different compounds. An improved approach for applications in the end-to-end preparation of pharmaceutically relevant small molecules was finally reported.

Chapter 8 summarizes the key results of the research introduced though the thesis, elaborates on the strategies for the design of optimized flow protocols integrated with several technology, and identifies the lessons for future works.

Each chapter of this thesis was written based on one or more separate publications and can be read independently. Accordingly, some overlap between the chapter introductions may occur.

Chapter *2*

Gram-Scale Domino Synthesis in Batch and Flow Mode of Azetidinium Salts

2.1. Introduction

Fragment-based drug design is becoming a paradigm for pharmaceutical synthesis.[137] However, the lack of molecular rigidity intrinsic to a majority of small molecules appears to be critical for the implementation of this approach. One of the most popular ways to limit molecular conformational flexibility relies on the introduction of saturated three- or four-membered nitrogen heterocycles. In this context, azetidinium salts are widely known for their versatility and peculiar reactivity: because of the ring strain, they are commonly used for alkylation via ring opening reactions with C, N, S, and O nucleophiles, and are also employed in the generation of substituted pyrrolidines via ring expansion reaction.[138–140] The usefulness of azetidinium salts has been proven in several fields, from

pharmaceutical synthesis to polymer branching.[141] In particular, they have been employed in the synthesis of 3-aryloxy-3-aryl-1-propanamines, key intermediates to make selective serotonin reuptake inhibitors such as fluoxetine.[142] Several studies have examined the development of synthetic protocols for the production of azetidiniums, following principally three pathways: the first via amide formation and subsequent reduction forming an amine that undergoes a ring-closing rearrangement,[143] the second via a ring-closure reaction to give the azetidine, which is then treated with methylating agents (MeOTf,[141] LiHDMS, or CH3I) to give the corresponding azetidinium salt,[144] and the last via epoxide aminolysis using secondary amines.[138] In particular, epoxide aminolysis has been extensively studied and various conditions have been developed, including those based on microwave- and ultrasound-assisted methods, on the use of lanthanide or aluminum triflates and Lewis acids reagents, and on solid acid supports.[145–151] Among epoxides, epichlorohydrin presents a chlorine atom as a substituent of the epoxy motif and is an essential building block for pharmaceutical and fine chemical synthesis, due to its peculiar reactivity toward nucleophiles. The possibility of easily obtaining from it β-aminoalcohols as key intermediates for β-blockers, like atenolol and propranolol, is one of the most attractive applications of this compound, which today is used also in polymer synthesis to prepare cellulose-based materials.[152–154] The principal issues for all of these synthetical pathways are the need for harsh conditions (cryogenic and/or reflux), hazardous reagents as starting materials (*i.e.*, SOCl2 or DIBAL-H), long and expensive purifications, and potential exothermic steps. In this direction, it is well established that continuous-flow chemistry, in which common batch reactors are replaced by microreactors with tailored geometry, materials, and dimensions, enables better control of the reaction parameters and driving forces, such as temperature, pressure, heat, and mass transfer.[20,155–158] In the case of the highly exothermic epichlorohydrin aminolysis, the better control of temperature operated by microreactors allows one to carry out the reaction in a safer way, with important consequences for the reaction yield. Finally, the use of a flow reactor meets the need for a safer, environmentally sustainable, and circular chemistry.

By exploiting this technology, we have developed a flow route to synthesize

azetidinium salts, elucidating the kinetics of the reaction and optimizing the process to understand the reaction mechanism and the effect of solvation and temperature.[159] We have also compared batch and flow data under optimized conditions to study the effect of the reactor geometry on the kinetics of the process. Finally, we have tested the flexibility of the protocol using different amines, from primary to secondary, evaluating the generality of the method with reactants having steric and electronic substitutions. Overall, the route presented herein is facile and rapid, and enables the synthesis of azetidiniums in gram quantities, making it possible to further explore the chemical space around them for pharmaceutical and fine chemical applications.

2.2. Experimental

Characterizations. Various amines and epichlorohydrin were purchased from Sigma-Aldrich. ^{1}H and ^{13}C NMR spectra were recorded on a Bruker 400 MHz spectrometer. ^{1}H and ^{13}C NMR chemical shifts are reported in parts per million downfield from tetramethylsilane in the Appendix A.

Batch Synthesis of 3-Hydroxyazetidinium Chloride. Epichlorohydrin (1 equiv, 28 mmol, 2.6 g, 2.8 M) was added dropwise to a stirred solution of amine (1 equiv, 28 mmol) in the appropriate solvent (5 mL), shown in Table 2.1, stirring at the desired temperature for 1 h. The crude mixture obtained was concentrated under vacuum and analyzed by NMR, using dibromomethane as an internal standard. No further purification was needed.

Continuous-Flow Synthesis of 3-Hydroxyazetidinium Chloride. A solution of epichlorohydrin (2.8 M in EtOH, flow rate of 0.5 mL min^{-1}) and a solution of amine (2.8 M in EtOH, flow rate of 0.5 mL min^{-1}) were introduced into the reactor by HPLC pumps, with a residence time of 60 min. The crude mixture obtained is concentrated under vacuum and analyzed by NMR, using dibromomethane as the internal standard. No further purification is needed.

Continuous-flow reactions were conducted in a UNIQSIS FlowLab unit, consisting of two HPLC pumps, a stainless-steel T-mixer, a HotCoil heater reactor station, and a back-pressure valve regulator of 10 bar. All of the reactions were

carried out in a 60 mL stainless steel coil reactor, with an internal diameter of 1 mm.

Kinetic Study. Epichlorohydrin (1 equiv, 28 mmol, 2.6 g, 2.8 M) was added dropwise to a stirred solution of diethylamine (1 equiv, 28 mmol, 2 g) in D_2O (5 mL), stirring at 25 °C for 48 h. Aliquots of the reaction mixture were withdrawn at the indicated time and immediately analyzed by ^{1}H NMR, using MeCN as the internal standard.

Reactor Modeling. The reactor simulation was performed using the COMSOL Multiphysics (version 6.3) suite, employing the Chemical Reaction Engineering, the Heat Transfer modules, and the physics-based meshing algorithm with a triangular mesh element size set to extremely fine to discretize the reactor. The kinetic parameters were determined by interpolating the experimental batch and flow data. A sinusoidal tube was constructed in lieu of a coil to reduce the computational complexity, given that the effects of the curvature of the coil on velocity, concentration, and temperature are minimal. The equations were solved numerically using Newton's method, and convergence was ensured by achieving an absolute error estimate of $<5 \times 10^{-4}$.

2.3.   Results and Discussion

Batch Optimization. We have initiated the work by conducting preliminary tests in batch mode, carrying out the aminolysis of epichlorohydrin using diethylamine, at room temperature, for 48 h in water. After dropwise addition of epichlorohydrin **1** to a stirred solution of diethylamine, the obtained 1-chloro-N,N-(diethylamino)propan-2-ol intermediate **2** spontaneously undergoes an intramolecular cyclization via bimolecular nucleophilic substitution (SN2) at C1, giving the corresponding N,N-(diethyl)-3-hydroxyazetidinium salt **3** in 75% yield. The formation and subsequent disappearance of the intermediate have been elucidated by ^{1}H NMR analysis, through the determination of the intensity of the characteristic peaks assigned to this product (dd, δ 3.64–3.70). This approach was the only one that could monitor the reaction, because the degree of conversion of

the two reactants could not be calculated given that both epichlorohydrin and diethylamine are volatile species and evaporate during concentration of the samples. The effects of the solvent (acetonitrile, hexane, ethanol, and water) and temperature (25, 60, and 80 °C in H_2O) are listed in Table 2.1. In particular, the yield of **3** increases with temperature from 2% at 25 °C to 51% at 80 °C in EtOH. The effect demonstrates that higher temperatures are needed to activate the nucleophilic addition and the subsequent intramolecular N-cyclization. The solvent can also make a major contribution to the reactivity. In fact, at 60 °C and 60 min, the reaction in EtOH gives a 30% yield and the reaction in H_2O gives an 71% yield. However, at 60 °C and 60 min, the reaction in acetonitrile gives a 11% yield and the reaction in hexane gives an 19% yield. These results confirm that,

Table 2.1. *Solvent and temperature screening for azetidinium synthesis under batch conditions[a]*

Entry	solvent	T (°C)	t (min)	yield[b] (%)
1	MeCN	60	60	11
2	hexane	60	60	19
3	EtOH	25	60	2
4	EtOH	60	60	30
5	EtOH	80	60	51
6	H_2O	25	5	3
7	H_2O	25	30	7
8	H_2O	25	60	11
9	H_2O	60	5	42
10	H_2O	60	30	55
11	H_2O	60	60	71
12	H_2O	80	5	69
13	H_2O	80	30	78
14	H_2O	80	60	84

[a]Conditions: 28 mmol of epichlorohydrin, 28 mmol of diethylamine, and 5 mL of solvent. [b]Determined by NMR, using dibromomethane as the internal standard.

differently from the classical solvent effect on SN_2 reactions, polar protic solvents are the most appropriate choice for the synthesis of azetidinium salts. This can be justified considering the increased level of activation of the epichlorohydrin and stabilization of the obtained aminolysis intermediate, involving pseudocyclic structures that are more stable in polar solvents.[160] Finally, longer reaction times are also beneficial for the reaction. On the basis of these results, it was possible to identify H_2O and EtOH as the best solvents and high temperature as a driving force for the reaction, which provided **3** in 83% and 51% overall yields, respectively, at 80 °C in 60 min. Both solvents have peculiar advantages. If water enhances the reaction yield, ethanol provides a better solubilization of the reactants, effectively improving mass transfer and being easier to remove from the reaction mixture.

Development of a Continuous-Flow Process. After this preliminary batch optimization, we have considered developing a flow route for the reaction. The choice of a flow reactor is justified on the basis of two main aspects: (i) safety concerns due to the reaction exothermicity (in the batch protocol, epichlorohydrin
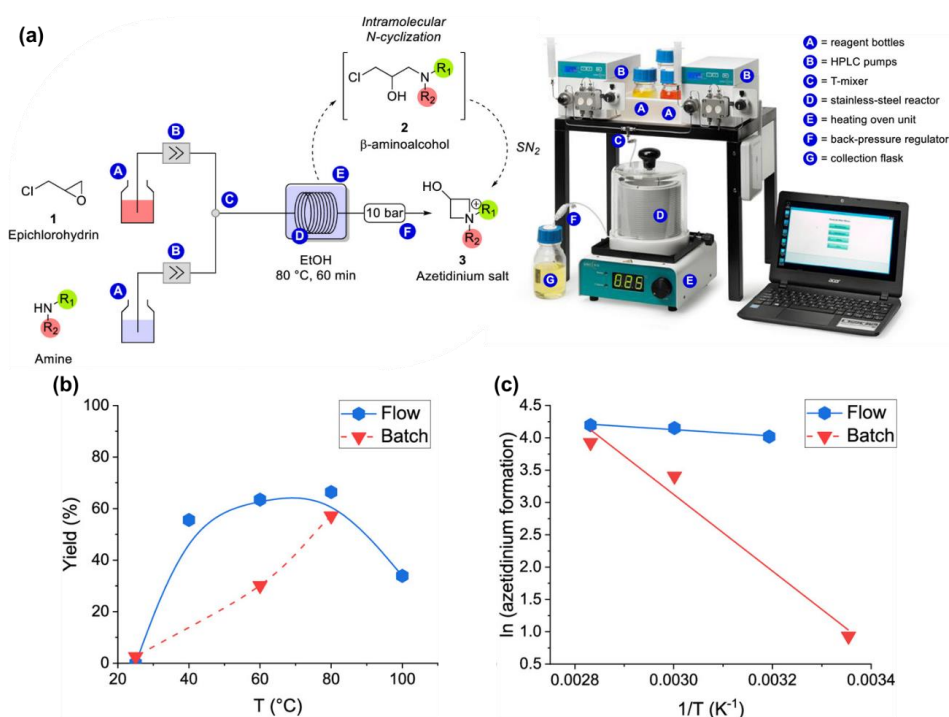
Figure 2.1. *Flow setup for azetidinium synthesis under continuous-flow conditions (a). Temperature screening under continuous-flow conditions and comparison with batch data (b and c).*

had to be added dropwise at 0 °C), addressed by the better containment upon operating microreactors as closed systems, and (ii) a more appropriate control of the reaction parameters, particularly heat transfer effects, due to the reactor geometry (Figure 2.1 a). For this reason, we have used a commercial UNIQSIS continuous-flow automated platform featuring two HPLC pumps that inject reagent solutions into the flow setup. After passing a T-mixer, reagents flow in a stainless-steel coil reactor (with an internal volume of 60 mL) under strictly controlled temperature and pressure conditions regulated by a heating module and a back-pressure regulator valve (10 bar), respectively. This intrinsic automation of the setup simplifies the synthetic protocol, avoiding the tedious and potentially harmful dropwise addition of epichlorohydrin to the amine-stirred solution. To investigate the reaction performance under flow conditions, we have decided to study the effect of temperature on the synthesis of **3**, evaluating the reaction in water and EtOH as solvents, and keeping 60 min as the residence time. Preliminary tests conducted in water led in all cases to the clogging of the reactor, mainly because of the low solubility of epichlorohydrin in water. To avoid these issues, EtOH was chosen as a solvent. This has enabled us to obtain comparative data between the batch and flow process, showing the increased yields under flow conditions (Figure 2.1 b). The enhancement of the reaction rate is corroborated by the vis-à-vis comparison of batch and flow data in Appendix A (Table A.2.1) and by the values of the activation energy determined by the Arrhenius analysis under kinetic conditions. In fact, the reaction under batch conditions requires an activation energy of 49 kJ mol^{-1}, while the same reaction under flow mode needs only 4 kJ mol^{-1} (Figure 2.1 c).

Substrate Scope and Scale-up Analysis. Finally, the influence of the reactivity of secondary amines with respect to azetidinium formation has been evaluated using different substrates (Figure 2.2 a). Aliphatic amines appear to be more suitable for azetidinium formation, due to the increased electron availability on the N atom given by the inductive effect of substituents. Product formation with noncyclic amines, like diethylamine **4** and dibutylamine **5** (66% and 29% yields, respectively), is particularly favoured, due to the absence of negative inductive effects. Moreover, steric hindrance does not appear to be prominent with alkylic

amines, as shown by product **6** (66%). Also, the ring strain of the amine appears to be a critical factor in the reactivity of the system. More constrained amines, like pyrrolidine, are suitable for the formation of the azetidinium **7**, observed in 49% yield, but unfavored if compared to azetidinium **8**, observed in a 75% yield. This kind of reactivity is probably due to the formation of an azaspirocyclic motif positively charged on the N atom, whose instability is a function of ring strain. Even if morpholine is a non-constrained cyclic amine, the low yield of **9** (28%) highlights a correlation between the basicity of amines and their reactivity: in fact, amines that furnished products from **4** to **8** have a pKa of ~11, whereas morpholine is slightly more acidic (pKa ~ 8). This trend can also be observed in **10**–**12**, where reactivity is heavily influenced by electronic factors. A negative inductive effect is prominent in the aminolysis mediated by diphenylamine, in which product **10** is not observed (0%); this effect is less accentuated with N-methylaniline, in which the positive inductive effect of the alkylic substituent is balanced by the negative one of the phenyl moiety, leading to the formation of open chain intermediate **11**
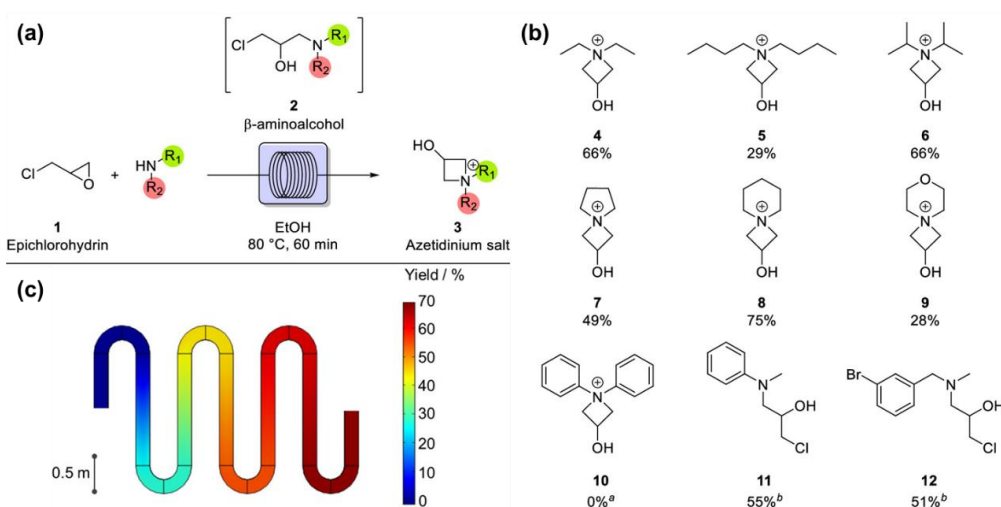
Figure 2.2. *Continuous-flow screening of substrates (a and b). CFD simulation for the continuous-flow synthesis of azetidinium salt from epichlorohydrin with diethylamine, showing the laminar flow rate and good fitting between the modeling and the experimental data (c). [a]As discussed in the text, the aminolysis is affected by the steric hindrance and negative inductive effect of diphenylamine, resulting in the absence of product formation. [b]The reaction stops at the formation of the open chain intermediate.*

(55% yield). Also using sterically hindered amines, but with favourable electronic effects and appropriate basicity, the formation of the azetidinium product is inhibited, stopping the reaction at the formation of intermediate **12** (51% yield). It has to be remarked that all of the yields reported in Figure 2.2 b refer to the compounds after flow synthesis and concentration in vacuum. In the case of incomplete conversion, the unconverted epichlorohydrin and the amine evaporate during concentration, leading to a clean product. To study the scalability of our process, all of the reactions have been carried out from 1 to 4 g scale; thus, all yields presented in this work can be considered as those for a scale-up process. This points to the efficiency of the method, which can generate azetidiniums quickly, in large amounts, and in very high purity: in fact, in all cases, only the product remains in the crude after rotatory evaporation, pointing to the high selectivity of the route. We have developed a computational fluid dynamic (CFD) model to describe this effect, as well as the fluid patterns and interfacial mass transfer in our flow reactor (Figure 2.2 c). The CFD simulation is in good quantitative agreement with the experiments, showing an ∼70% yield of **3** at the outlet of the reactor, in line with the experimentally observed 66% yield. The model indicates that the dominant transport mechanism is a laminar flow pattern, in line with previous literature data.[5]

Mechanistic and Kinetic Studies. We have finally conducted kinetic studies, carrying out the reaction in deuterium oxide as the solvent. This is possible by withdrawing and immediately analyzing the solution at 25 °C. Monitoring the reaction in time, we have observed an increase in the level of product formation, which is initially slower, due to intermediate formation, whose rearrangement to the product makes the azetidinium formation more visible at longer reaction times (Figures 2.3 a). In particular, product selectivity data confirm this hypothesis, as this parameter also decreases with time at higher temperatures; this trend can be justified considering polymerization side reactions. The high conversion data obtained from the beginning of the reaction at all temperatures demonstrate the high reaction rate of intermediate formation; moreover, the low yield and selectivity for the intermediate show the high rate of the N-cyclization reaction, for an overall fast process. This hypothesis is confirmed by following
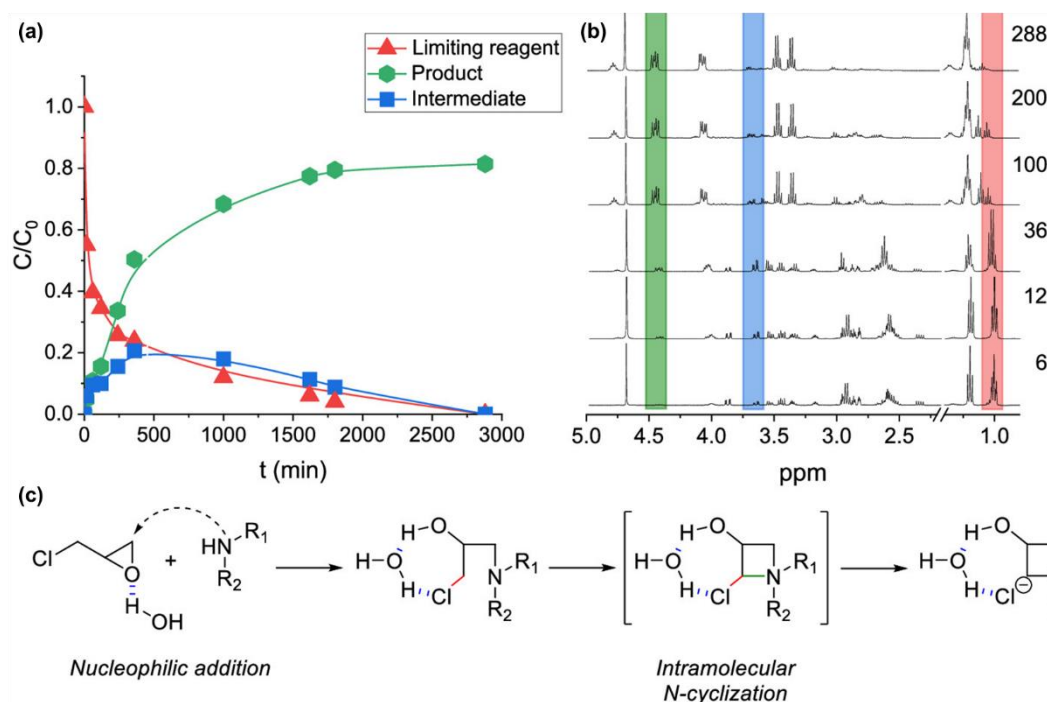
Figure 2.3. *Variation of the concentrations of species during the reaction (a). NMR analysis in operando (b) and proposed mechanism for the reaction (c).*

characteristic peaks of the reagents, product, and intermediate in NMR spectra (Figure 2.3 b), revealing a decrease in the intensity in time of the diethylamine peak (t, δ 1.00), contextual to an increase in the height of azetidinium peaks (dd, δ 4.49–4.58) and to an earlier increase and successive decrease in intensity for the intermediate signal (dd, δ 3.64–3.70). The concentrations of species have been calculated by integrating these peaks, and the variation of the concentration with time is shown in Figure 2.3 a. On the basis of these results, we can state that the reaction mechanism in batch and flow mode involves the fast formation of the 1-chloro-N,N-(diethylamino)propan-2-ol intermediate, which rearranges quickly, giving the final azetidinium product. In the reaction mechanism, an important role is played by the presence of a polar solvent (such as water or EtOH), which activates the epichlorohydrin and initiates the nucleophilic addition, stabilizing both the intermediate and the product as illustrated in Figure 2.3 c. However, for the case of a flow reaction, this mechanistic effect must be combined with practical aspects, and thus, EtOH has been selected as a solvent to avoid clogging issues in the microreactor and solubilize completely the reagents.

2.4. Conclusions

In summary, we have reported the aminolysis of epichlorohydrin with diethylamine, elucidating the role of solvation, reaction time, and temperature on the reaction yield. The flow method has proved to be highly efficient, giving the corresponding azetidinium salt **3** in higher yields compared to the batch method. In addition to that, we have shown that the continuous process is faster than the batch reaction. Moreover, the intrinsic automation of the flow setup plays a key role in the simplification of the process, avoiding time-consuming and potentially harmful operations, such as adding dropwise epichlorohydrin. The proposed continuous-flow protocol appears to be suitable for a scaled-up synthesis and for different kinds of secondary amines, showing the good flexibility of the procedure.

Chapter 3

Telescoped Flow Production of Glycidyl Derivatives Starting from Sunflower Oil

3.1. Introduction

Circularity of processes plays a pivotal role in all chemical-related areas. Recycling waste materials and recovering valuable elements from waste are fundamental aspects of contemporary industrial processes, aligning with the basic principles of green chemistry.[1,161] From this perspective, significant attention has been devoted to the valorization glycerol and glycidol (2,3-epoxy-1-propanol). These compounds are extensively examined due to their widespread presence as byproducts in processes connected to oils and fatty acid production, as well as in alimentary industrial field.[162,163] Additionally, glycidol holds exceptional importance as a building block in fine chemical and pharmaceutical synthesis, owing to its unique dual reactivity as both an alcohol and an epoxide towards nucleophilic and electrophilic species.[164–166] Therefore, several products of interest are synthesized using glycerol and glycidol as starting materials. These encompass glycerol carbonate, glycerophosphocholine, surfactants, dyes, and even drugs with

pharmaceutical applications, possessing antiarrhythmic and antiviral properties.[166–173] From a synthetic point of view, glycerol is usually recovered as byproduct from the transesterification of fats and oils *via* triglycerides hydrolysis in the production of biodiesel.[162,174,175] On the other hand, glycidol can be obtained from several reaction pathways, using glycerol or allyl alcohol as starting materials. However, in all these cases, the described methods necessitate prolonged reaction times, the use of potentially harmful reagents, high temperatures (up to 350 °C), and elevated pressure. These processes also involve the creation of unstable intermediate substances, such as 2-chloropropanediol, and require expensive catalysts and additives (notably titanium silicates).[176–181] To address the increasing demand for environmentally friendly processes, the emergence of continuous-flow chemistry is a significant advancement. This technology represents a breakthrough for developing circular processes, mainly due to its ability to finely control the parameters of chemical reactions.

Within this study, the advanced capabilities of this enabling technology were highlighted, including improved heat and mass transfer, enhanced selectivity, and the potential for consecutive reactions without the need to store unstable and hazardous intermediate compounds.[133,182,183] Additionally, the superior containment afforded by microreactors operating as closed systems leads to heightened safety levels in reactions, a pivotal factor in scaling up processes, making them suitable for industrial applications.[159] In this research work, a telescoped flow process was investigated for the production of glycidol. This process utilized cost-effective and commonly available reagents, such as hydrogen chloride, acetic acid, and self-produced glycerol. The containment feature of microreactors was harnessed to mitigate the toxicity and hazards associated with these substances. The study also outlines the optimized production of glycerol at a gram-scale under flow conditions. Notably, the upscaled synthesis of glycidol was also utilized in the creation of several value-added products arising from tosylation. These products represent essential components for applications in pharmaceuticals and polymer science.

3.2. Experimental

Batch synthesis of glycerol. 10 mL of a saturated solution of KOH in MeOH were added dropwise to a stirred solution of sunflower oil (10 mL). After 2 h, the obtained crude mixture was quenched, adding an aqueous solution of HCl 2M up to complete neutralization, and 10 mL of EtOAc to get rid of the triglycerides produced during the reaction. The aqueous phase was collected, concentrated under vacuum, and analyzed by NMR, using MeCN as an internal standard. No further purification was needed.

Flow synthesis of glycerol. A saturated solution of KOH in MeOH and sunflower oil (10 mL) were introduced separately into a stainless-steel coil reactor by a syringe pump, at different residence times. The obtained crude mixture was quenched, adding an aqueous solution of HCl 2M up to complete neutralization, and 10 mL of EtOAc to get rid of the triglycerides produced during the reaction. The aqueous phase was collected, concentrated under vacuum, and analyzed by NMR, using MeCN as an internal standard. No further purification was needed.

Batch synthesis of glycidol. HCl 13M (24 mmols, 4 equiv) was added dropwise to a stirred solution of glycerol (6 mmols, 1 equiv) and acetic acid (2 mmols, 0.33 equiv) at 120 °C. After 2 h, the obtained crude mixture was quenched, adding an aqueous solution of NaOH 9.5M up to complete neutralization, and stirred for 0.33 h. The analysis was conducted after functionalization using tosyl chloride (TsCl), following the procedure described in the following section (Batch synthesis of glycidyl tosylate).

Flow synthesis of glycidol. HCl 13M (24 mmols, 4 equiv) was added dropwise to a stirred solution of glycerol (6 mmols, 1 equiv) and acetic acid (2 mmols, 0.33 equiv). The resulting solution was introduced in a PFA coil reactor by a syringe pump, using different residence times and temperatures. The obtained crude mixture was quenched, injecting an aqueous solution of the indicated base up to complete neutralization, using 0.33 h as residence time. The analysis was conducted on the collected solution after functionalization using tosyl chloride

(TsCl), following the procedure described in the following section (Batch synthesis of glycidyl tosylate).

Batch synthesis of glycidyl tosylate. Tosyl chloride (20 mmols, 1 equiv) was added to a stirred solution of glycidol (20 mmols, 1 equiv) and triethylamine (60 mmols, 3 equiv) in the indicated solvent mixture (32 mL), at 0 °C. After 1 h, an aliquot was withdrawn from the obtained crude mixture and analyzed by HPLC.

Flow synthesis of glycidyl tosylate. A solution of glycidol (20 mmols, 1 equiv) in H$_2$O (16 mL) and a solution of TsCl (mmols, 1 equiv) and triethylamine (60 mmols, 3 equiv) in the indicated solvent (16 mL) were introduced separately into a PFA coil reactor by a syringe pump, at different residence times. An aliquot was withdrawn from the collected crude mixture and analyzed by HPLC.

3.3. Results and Discussion

Our investigation into glycidol production began with the optimization of glycerol synthesis under flow conditions, using sunflower oil as starting material. As shown in Figure 3.1, the reaction was performed in a stainless-steel coil reactor, injecting the oil phase and a saturated solution of KOH in methanol. To investigate the reaction progress in continuous-flow mode, we evaluated the formation of glycerol **1** screening different residence time conditions (Figure 3.1 b). From 30 to 60 min a reasonable yield increase, from 49 to 78%, was observed. The subsequent increase of reaction time up to 180 min (75% and 76%), results in no further rise in reaction yield, related to the achievement of the optimal reaction conditions. Choosing 120 min as residence time, comparative data between the batch and flow process with this reaction time show a substantial difference between the two conditions, obtaining only 48% of **1** in the batch case, with respect to the 75% achievable in flow. The significative improvement is attributed to the enhanced mass transfer, resulting from the higher contact between the two phases enable by the small-volume flow cells.

The study continued with the investigation on the glycidol preparation, starting from glycerol obtained using the abovementioned protocol, starting form a preliminary batch screening. Then, the reaction was conducted using a
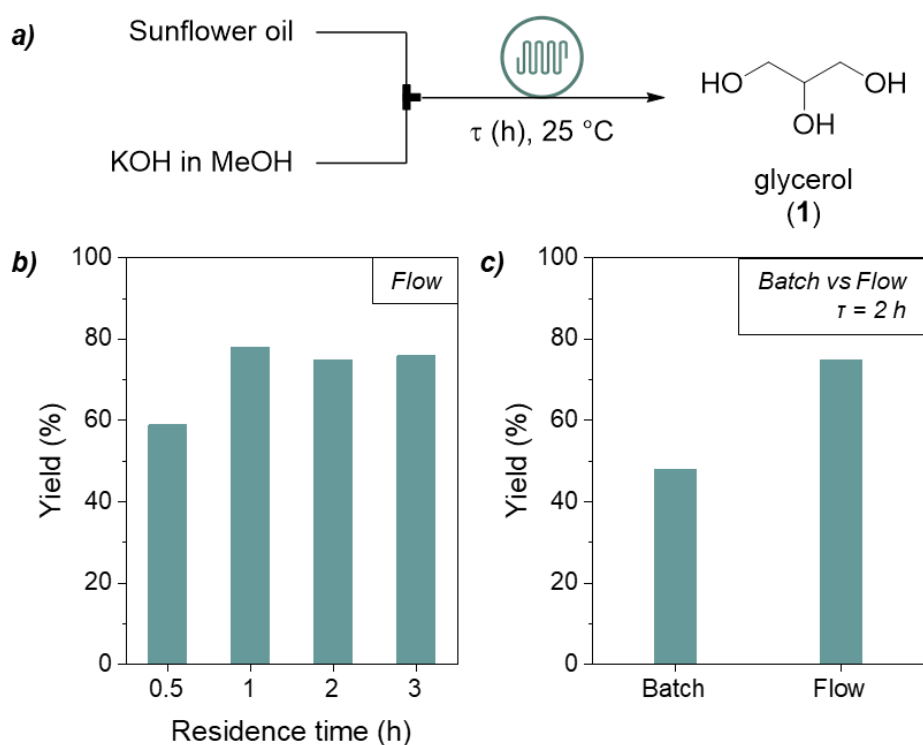
Figure 3.1. *Schematic representation of the glycerol synthesis.*

commercially available Carousel 12 Plus Reaction Station™. The standard conditions involved the use of an aqueous solution of hydrochloric acid (HCl), as chlorine source, and acetic acid (AcOH), as catalyst, at 120 °C, affording the target product **3a** in 31% and 79% yield using 0.15 equiv and 0.33 equiv respectively, after 2 h (Table 3.1, Entries 1 and 2). These results reflect the relevant effect of the catalyst amount on the reaction progress. Increasing the equivalents up to 0.66, a slight decrease in the glycidol yield occurs (Table 3.1, Entry 3), due to the further chlorination taking places, affording product **2b**. The complete reaction profile over 24 h using different equivalents of AcOH was investigated. Moreover, different organic acidic catalysts were tested. Compared to acetic acid, citric acid gave lower conversion and lower yield for **3a** (Table 3.1, Entry 4), associated with the increased formation of **2a** (15%) resulting from the poor catalytic efficiency of this catalyst, presumably further affected by its thermal instability. Adipic acid (Table 3.1, Entry 5) gave good conversion and yield for the target product **3a** (91%), and very low selectivity for all the other byproducts. These results clearly show the negative effect that steric hindrance plays on the catalytic performance.

Table 3.1. *Screening of different catalysts in batch.*
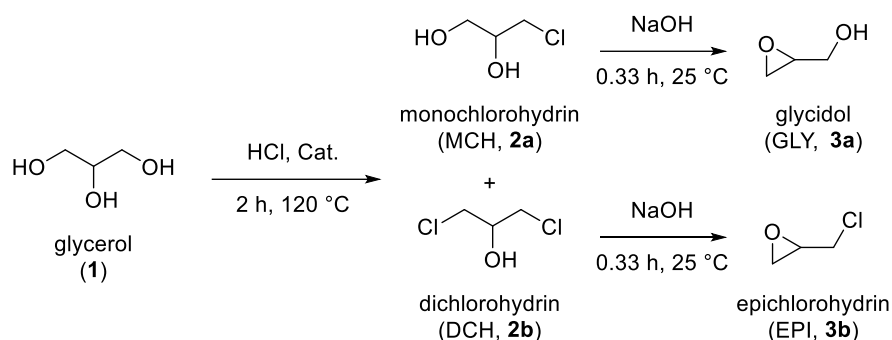
	Entry[a]	Catalyst	Catalyst equiv	Conversion[b] (%)	Yield[b] (%) 2a	Yield[b] (%) 3a
	1	AcOH	0.15	34	2	31
	2	AcOH	0.33	94	5	79
Influence	3	AcOH	0.66	>99	5	65
of catalyst	4	Citric Acid	0.33	>99	15	44
	5	Adipic Acid	0.33	>99	6	91
	6	none	-	27	1	26

[a]If not indicated otherwise, the reactions were conducted in a batch reactor, using **1** (6 mmol), HCl 13 M (24 mmol), catalyst, NaOH (24 mmol), temperature 120 °C, and reaction time 2 h; [b]Determined by ^{1}H-NMR.

Table 3.2. *Screening of different catalyst amount in flow.*
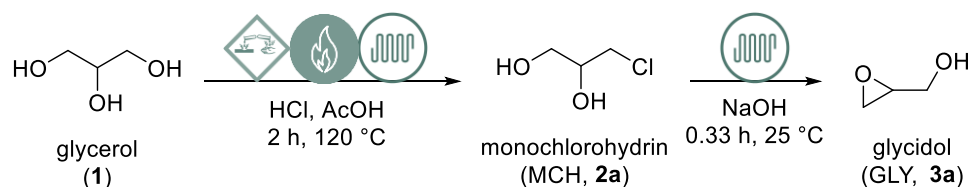
	Entry[a]	Catalyst equiv	HCl conc.	Conversion[b] (%)	Yield[b] (%) 2a	Yield[b] (%) 3a
Influence of	1	0.15	13 M	>99	5	63
catalyst	2	0.33	13 M	>99	-	>99
amount and	3	0.66	13 M	>99	-	>99
acid						
concentration	4	0.33	6.5 M	>99	1	4

[a]The reactions were conducted in a flow reactor, using **1** (72.6 mmol), HCl 13 M (290.4 mmol), AcOH (24.0 mmol), base (290.4 mmol), and pressure 4 bar. [b]Determined by ^{1}H-NMR.

Moreover, the uncomplete solubility and the formation of a significant amount of solid precipitate was observed in both these cases, affecting the possibility to use them in the flow reaction. Also, the poor conversion achieved in absence of any catalyst is illustrated in Table 3.1 (Entry 6), confirming the requirement for the use of an acidic catalyst to perform the reaction.

      With the optimal conditions in hand, we decided to switch to the flow conditions, conducting the reaction in a commercial Uniqsis™ reactor. We began our flow investigation by using different amounts of acetic acid. Comparing the results with the one obtained in the previous batch screening, it's clear that improved heat and mass transfer phenomena are enabled by flow conditions, affording the target product **3a** in all cases (Table 3.2, Entries 1-3). Moreover, increasing the amount of catalyst over 0.33 equiv, appeared to be ineffective on the reaction progress. Different concentrations of HCl were also tested, clearly indicating the importance of this parameter on the process. Since the very low yield of **2a** (1%) and **3a** (4%) achieved in these conditions, further investigation on the products generated will be performed (Table 3.2, Entry 4).

Several experiments were performed, varying both temperature and residence time for the first reaction step, and collecting data in the contour map reported in Figure 3.2. The plot clearly illustrates a linear trend, mainly related to the temperature: 100°C appears to be a cut-off value required for the chemical transformation to take place. Accordingly, 100 °C and 2 h were chosen as optimal conditions to continue our investigation.

The subsequent step cyclization step was then investigated, starting from the screening of different bases (Table 3.3, Entries 1-5). The absence of base appeared to totally prevent the product formation, since no conversion occurred.

The effect of pK_b on the reaction progress was then evaluated, using $CaCO_3$ ($pK_b = 3$), KOH ($pK_b = 0.5$) and NaOH ($pK_b = 0.2$), as listed in Table 3.3 (Entries 2-4). Increasing the pK_b values, the positive effect on the selectivity for product **3a** was evident, as highlighted from the complete conversion of **1** in **3a** achieved using NaOH. Interestingly, the weakest base used (Table 3.3, Entry 2) pushed the selectivity for product **2a**, strongly restricting the formation of **3a**. Since NaOH was selected as best base, the role of the solution concentration was screened,
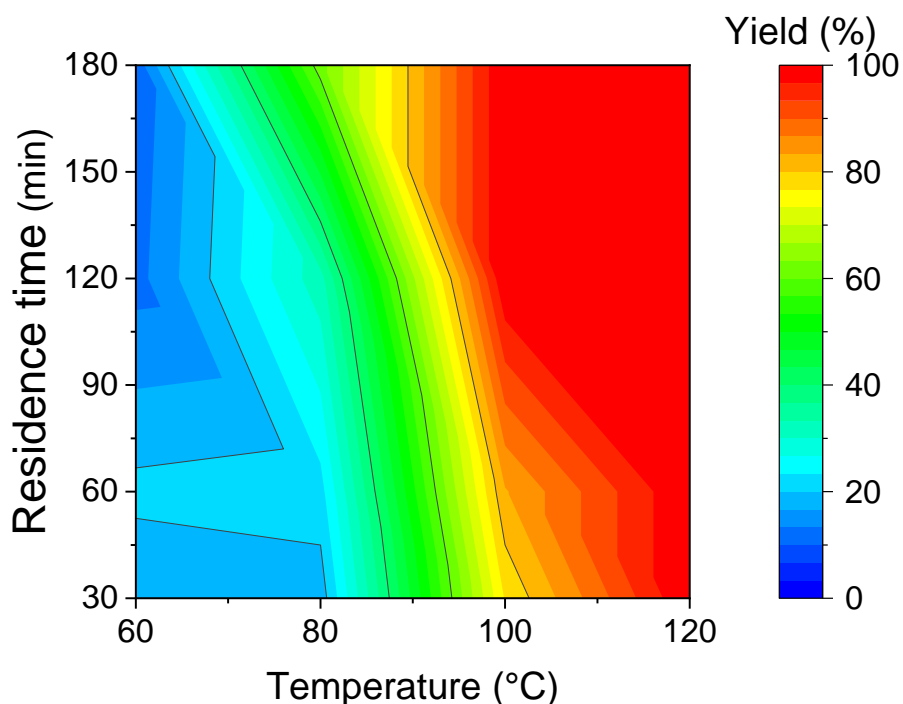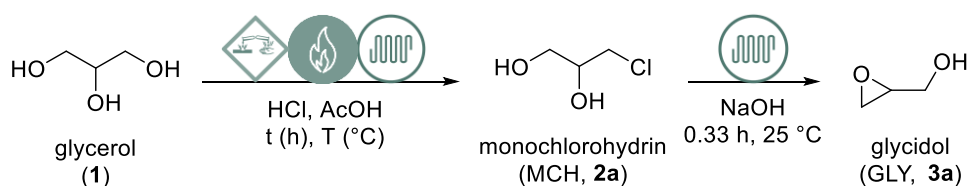
Figure 3.2. 3D contour map of temperature vs residence time. The reactions were conducted in a flow reactor, using 1 (72.6 mmol), HCl 13 M (290.4 mmol), AcOH (24.0 mmol), base (290.4 mmol), and pressure 4 bar.

comparing results obtained using solutions 9.6M, 5M, and 2.5M (Table 3.3, Entries 4, 5, and 6). A slight decrease in **3a** yield (72% and 64%, respectively) was noticed, confirming the necessity to use more concentrated basic solutions. Finally, a comparison between different residence times was conducted (Table 3.3, Entries 4, 7, and 8): increasing the time from 0.03 to 0.33 h no effect was detected. In contrast, a further increase up to 1.67 h appeared to be deterrent for the product formation, since the hydrolysis of **3a** takes places over this time.

Our investigation continued with the functionalization of glycidol **3a** using tosyl chloride **4**, obtaining glycidyl tosylate **5**, focusing on the optimization of the reaction protocol in both batch and flow conditions. The influence of solvent the

reaction progress was investigated, using mixtures of organic solvents and water (Table 3.4, Entries 1-4), and obtaining the target product **5** in low yields with a slight increase when only water was used (53%, Table 3.4, Entry 4). Also, the influence of pH on the process was confirmed by conducting the reaction at different pH values, namely 14, 7, and 0 (Table 3.4, Entries 4-6), confirming the need for a strong basic environment. Due to the suboptimal solubility of TsCl **4** in all the solvent mixture tested, except for the mixture H_2O/$CHCl_3$ (1:1), the latter was chosen as solvent for the following flow study.

Different residence times were screened, but no relevant differences between 0.5, 1, and 2 h were detected 0 (Table 3.5, Entries 1-3). In contrast, it's possible to appreciate a significant improvement, from 35% to 51% yield of **5**, between batch and flow conditions (Table 3.4 Entry 1, Table 3.5 Entry 2). Using 1 h as reaction time, we decided to investigate different reaction parameters, namely concentration of TsCl **4** and solvent. The first approach resulted to be successful, prompting the product yield

Table 3.3. Reaction optimization under flow conditions.

	Entry[a]	Base	Variation	Conversion[b] (%)	Yield[b] (%) 2a	3a
	1	none	None	-	-	-
	2	CaCO₃ [20 wt%]	0.33 h	>99	63	6
Influence of	3	KOH [9.6 M]	0.33 h	>99	5	85
base	4	NaOH [9.6 M]	0.33 h	>99	-	>99
	5	NaOH [5.0 M]	0.33 h	>99	4	72
	6	NaOH [2.5 M]	0.33 h	>99	7	64
Influence of	7	NaOH [9.6 M]	0.03 h	>99	-	>99
time (II step)	8	NaOH [9.6 M]	1.67 h	>99	5	73

[a]The reactions were conducted in a flow reactor, using **1** (72.6 mmol), HCl 13 M (290.4 mmol), AcOH (24.0 mmol), base (290.4 mmol), and pressure 4 bar. [b]Determined by ¹H-NMR.

Table 3.4. *Solvent and pH screening on glycidol tosylation in batch conditions.*

glycidol
(GLY, **3a**)   tosyl chloride
(TsCl, **4**)   Et₃N, solvent
1 h, 25 °C   glycidyl tosylate
(**5**)
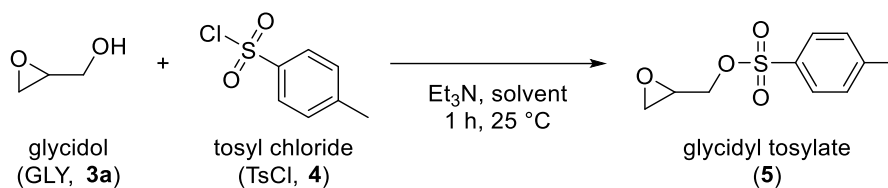
	Entry	Solvent	pH	Yield (%)
	1	H_2O/CHCl$_3$ (1:1)	14	35
Influence of	2	H_2O/DMF (1:1)	14	35
solvent	3	H_2O/Et$_2$O (1:1)	14	43
	4	H_2O	14	53
Influence of	5	H_2O	7	3
pH	6	H_2O	0	-

Table 3.5. *Reaction optimization under flow conditions.*

glycidol
(GLY, **3a**)   tosyl chloride
(TsCl, **4**)   Et₃N, solvent
t (h), 25 °C   glycidyl tosylate
(**5**)
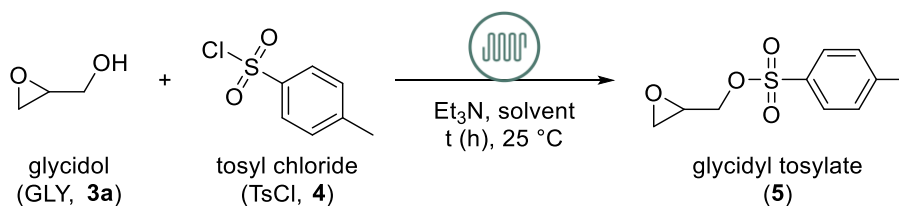
	Entry	Residence time (h)	Concentration TsCl [mmol mL^{-1}]	Solvent	Yield (%)
Influence of time	1	0.5	1.1	H_2O/CHCl$_3$ (1:1)	46
	2	1	1.1	H_2O/CHCl$_3$ (1:1)	51
	3	2	1.1	H_2O/CHCl$_3$ (1:1)	50
Influence of concentration	4	1	1.4	H_2O/CHCl$_3$ (1:1)	58
Influence of solvent	5	1	1.4	H_2O/CH$_2$Cl$_2$ (1:1)	50

up to 58% (Table 3.5, Entry 4); on the other hand, the use of dichloromethane instead of chloroform in these conditions led to a slight decrease of the reaction yield, due to the formation of a solid precipitate, insoluble in this solvent mixture, in the microreactor.

3.4. Conclusions

Sustainable development goal has raised increasing attentions in the production and management of waste, trying to convert it in a value-added element. In this study, we highlighted the benefits of microreactor technology in the development of circular processes, by promoting the valorization of byproducts generated during the biofuel production. Therefore, the telescoped synthesis of gycidol was presented, starting from the triglycerides hydrolysis under flow conditions. The optimized biphasic oil/water reaction, producing glycerol as intermediate, was in-depth investigated, affording promising outcomes. The subsequent intramolecular cyclization to produce glycidol was then performed, followed by the optimization of the reaction conditions to obtain the desired product in gram-scale and high-selectivity. The study was extended by producing further functionalized derivatives, with potential applications in the field of medicinal chemistry and polymer science. This work highlights once again the potentiality of continuous-flow chemistry to revolutionize the organic synthesis approach, finding his strength in crucial aspects for its industrial applications, such as safety and circularity.

Chapter 4

Nanostructured Carbon Nitride for Continuous-Flow Trifluoromethylation of (Hetero)arenes

4.1. Introduction

Trifluoromethyl groups are recognized as important substituents in drug candidates, owing to their ability to enhance lipophilicity.[184–186] Therefore, the implementation of efficient and sustainable methods for the late-stage incorporation of trifluoromethyl groups has garnered considerable attention in the field of organic and pharmaceutical synthesis.[187–189] Conventional protocols for the thermo-catalyzed trifluoromethylation of aromatics require harsh conditions.[190–194] In this regard, photocatalysis is an attractive technology to develop energy-saving processes that leverage light to stir chemical

transformations.[195–198] Such techniques offer numerous benefits, which include milder operational conditions (e.g., generally photochemical reactions are carried out at room temperature and atmospheric pressures),[199] replacement of transition metals and toxic reagents with greener photoactive analogues,[200–202] and shorter reaction times.[203] To date, the light-driven introduction of CF_3 to (hetero)aromatics has predominantly been achieved through metal-based homogeneous and heterogeneous photocatalysts.[204–206] Metal-free methodologies have been suggested in the scientific literature, but their industrial implementation has been limited. This limitation has been attributed to insufficient understanding of the catalytic mechanism and difficulties associated with scaling up the methods. Carbon nitride (CN_x) is one of the potential catalysts for metal-free trifluoromethylation.[207,208] This non-toxic material is prepared from cheap precursors (e.g., urea, thiourea, cyanamide, dicyanamide, or melamine) via simple synthetic routes including thermal or photochemical polymerization.[209] Properties of this class of materials include visible-light absorbing capabilities due to their semiconducting nature and corresponding band gap energy of ca. 2.7 eV, excellent thermo- and photostability, and tunable surface area achievable through different synthetic methods that lead to the formation of allotropes. These allotropes include graphitic carbon nitride (gCN_x), exfoliated nanosheets of graphitic carbon nitride (nCN_x), and mesoporous graphitic carbon nitride ($mpgCN_x$).[210,211]

In this work, we investigate the nanostructuring of carbon nitride for the trifluoromethylation reaction of heteroaromatics, elucidating the effect of structural properties, surface area, and band gap modulation on the reaction progression.[183] This enabled us to derive structure–property relationships that were exploited to design a continuous-flow process for the green and upscaled production of trifluoromethylated (hetero)aromatics. The flow protocol was then adopted for the synthesis of a variety of functionalized heteroaromatics.

4.2. Experimental

Catalyst Synthesis. To prepare graphitic carbon nitride, cyanamide (10 g; Sigma Aldrich, 99%) was heated for 3 h at 550 °C (heating ramp: 10 °C min^{-1}) in an alumina crucible. To prepare nanosheet carbon nitride, the as-obtained gCN_x

was exposed to further thermal exfoliation at 550 °C for 3 h (heating ramp: 2 °C min^{-1}). To prepare mesoporous graphitic carbon nitride, cyanamide (3 g; Sigma Aldrich, 99%) was added to SiO_2 Ludox HS40 with 12 nm particles (7.5 g; Sigma Aldrich, 40% aqueous dispersion) and heated under stirring at 70 °C for 16 h. The resulting white solid was heated for 8 h at 550 °C in an alumina crucible (heating ramp: 2.2 °C min^{-1}). The obtained material was then added to a 4.2 M solution of NH_4HF_2 (12 g in 50 mL of water; Sigma-Aldrich, 95%), kept under stirring for 24 h, and then centrifuged to obtain the product after three washes with water and ethanol.

Catalyst Characterization. The specific surface areas of the prepared materials were obtained via N_2 physisorption experiments, degassing the samples at 150 °C for 20 h and then measuring the isotherms on a Micromeritics 3Flex porosimeter at 77 K. Data were analyzed using a QuadraWin 5.05 software package applying the Brunauer–Emmett–Teller (BET) model to the adsorption isotherms for $0.05 < p/p_0 < 0.3$. The porosity and pore distribution were calculated by using the model of quenched solid density functional theory (QSDFT) for N_2 adsorbed on carbon (assuming cylindrical pore shape) at 77 K. A Philips model PW3040/60 X-ray diffractometer was used for powder X-ray diffraction (XRD), applying Cu Kα radiation ($\lambda = 0.15418$ nm). Elemental analysis (CHNS) was performed on a Vario Micro device by combustion.

Trifluoromethylation Reactions. The reactions were conducted on a commercial PhotoCube apparatus, consisting of an irradiated chamber versatile enough to account both reaction flasks and flow reactors. The apparatus is equipped with multicolor and UV LEDs (at eight different wavelengths) with an input power of up to 128 W. Magnetic stirrers inside the chamber enable proper mixing in batch conditions. For the batch experiments, the catalyst (100 mg) and the base (3 mmol) were added to a test tube, which was degassed for 15 min under a N_2 flow. Then, trifluoromethanesulfonyl chloride (herein indicated as TfCl, 1.3 mmol), the (hetero)aryl compound (1 mmol), and the solvent (8 mL) were added. The reaction mixture was closed, placed in the PhotoCube apparatus, kept under magnetic stirring, and irradiated with blue light ($\lambda = 457$ nm) for 60 min. At the

end of the reaction, the suspension was filtered to remove the catalyst.

For continuous-flow experiments, a physical mix of mpgCN$_x$ (50 mg), base (276 mg), and 50 μm of glass beads (2 g) was grinded in a mortar and blended in a vortex generator for 2 min. A transparent and flexible fluorinated ethylene-propylene (FEP) tube (500 mm long, 3.2 mm o.d., and 2.1 mm i.d.) was filled with the heterogeneous solid mixture and plugged with a quartz wool filter. The reactor was connected via 1/8″ o.d. 1/4″ 28 flat bottom flangeless fittings to the other 1/16″ o.d. tubing. The reactor volume was calculated as dead volume using the difference between the dry packed-reactor mass and the mass of the packed reactor filled with the reaction solvent. A solution of the (hetero)aryl reagent (0.25 M in acetonitrile, MeCN, flow rate: 0.03 mL min^{-1}) and a solution of TfCl (0.25 M in MeCN, flow rate: 0.03 mL min^{-1}) were introduced by syringe pumps (NE-1000, New Era Pump Systems, Inc.) operating at quasi-ambient pressure into the assembled packed-bed photoreactor. The reaction mixture was irradiated with blue light.

For both batch and flow experiments, an aliquot of the reaction mixture was withdrawn, and the product formation and starting material conversion were calculated using an Agilent 1200 high-performance liquid chromatography (HPLC) instrument, equipped with a UV detector G1315D working at $\lambda = 210$ nm, and a C18 HypersilGOLD 5 μm 175 Å column (Thermo-Fisher). Samples were analyzed using MeCN/H$_2$O 60:40 as a mobile phase with a total flow rate of 0.7 mL min^{-1} at 40 °C. ^{1}H and ^{19}F-NMR spectra were recorded with a Bruker 400 MHz Nuclear Magnetic Resonance spectrometer.

4.3.   Results and Discussion

Characterization of the Carbon Nitride Catalysts. Metal-free carbon nitride materials, namely, graphitic (gCN$_x$), nanosheet (nCN$_x$), and mesoporous graphitic (mpgCN$_x$) carbon nitrides, possessed different surface area and porosity features.[212] Porosity, pore distribution, and surface area data of the prepared materials were deduced via N$_2$ physisorption experiments. Brunauer–Emmett–Teller (BET) adsorption isotherms demonstrated the non-porous nature of gCN$_x$ and nCN$_x$ materials juxtaposed with that of mpgCN$_x$ (Figure A.4.1 a), which bore

a high surface area (157 m^2 g^{-1}). The material phase purity and crystallinity were evaluated through X-ray powder diffraction (XRD) studies. XRD diffractograms showed two characteristic diffraction peaks at 2θ = 13 and 28°, which, in accordance with the literature, correspond to the (100) and (002) planes, respectively. The former denotes the trigonal N-linkage of the triazine moiety, while the latter represents the stacking of aromatic rings. No other peaks were observed, confirming the absence of other crystalline impurities (Figure A.4.1 b). Elemental analysis of the prepared samples was carried out via CHNS analysis. The C/N values were found to lie in the range of 0.61–0.67 (Table A.4.1), close to the ideal value of 0.7 for the basic heptazine structure of CN$_x$. Discrepancies from the ideal value are typically ascribed to defects originating from the thermal polymerization process.[213] Nevertheless, the low H content values confirmed a high extent of polymerization of the cyanamide precursor, with only a low percentage of non-polymerized units carrying residual protons.[213]

Reaction Optimization in Batch and Role of the Surface Area. These materials were first evaluated under batch conditions using the PhotoCube setup as well as pyrrole **1** and trifluoromethanesulfonyl chloride (TfCl) **2** as starting materials, K$_2$HPO$_4$ as base, blue light, acetonitrile (MeCN) as solvent, and carrying out the reaction for 60 min. Preliminary investigation on the effect of catalyst surface area was conducted using the gCN$_x$ and nCN$_x$ samples, which afforded the desired product in yields below 10% due to the characteristic low surface area of this kind of nanostructuring. Indeed, compound **3a** was obtained with 80% yield when mpgCN$_x$ was used as catalyst, in accordance with the increased surface area features of mesoporous graphitic materials. The effect of the base and reactant stoichiometry are listed in Table 4.1. In particular, base screening experiments show that there is a direct correlation between the base strength and the selectivity for the product obtained: with a strong base such as K$_2$HPO$_4$ (Table 4.1, entry 4; pK$_b$ = 1.3), conversion and yield of 96 and 80% were obtained, respectively, along with a high selectivity for the monotrifluomethylated product **3a** of 84%. Conversely, employing weaker bases, namely, KH$_2$PO$_4$ (Table 4.1, entry 3; pK$_b$ = 7.2), and KF (Table 4.1, entry 2; pK$_b$ = 10.83), leads to only minor yields for the desired product **3**. Moreover, the reaction process appears to

Table 4.1. *Optimization studies for the photocatalytic trifluoromethylation of pyrrole using mesoporous carbon nitride catalyst. The optimal conditions are highlighted in orange.*
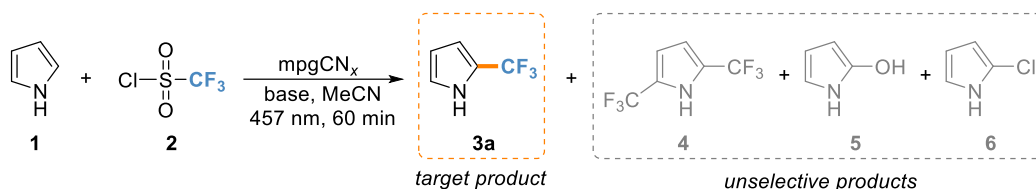
	Entry	Base	Variation	Conversion[b] (%)	Selectivity[b] (%)	
					3a	others (4+5+6)
Influence of base	1	none	None	91	42	44
	2	KF	None	99	71	23
	3	KH$_2$PO$_4$	None	95	75	17
	4	K$_2$HPO$_4$	None	96	84	13
Influence of TfCl content	5	K$_2$HPO$_4$	TfCl (1.2 mmol)	97	72	16
	6	K$_2$HPO$_4$	TfCl (1.5 mmol)	100	53	29
Influence of reaction conditions	7	K$_2$HPO$_4$	no N$_2$	73	22	75
	8	K$_2$HPO$_4$	no catalyst	82	7	75
	9	K$_2$HPO$_4$	no light	17	-	81
	10	K$_2$HPO$_4$	LED strip	64	6	75

[a]If not indicated otherwise, the reactions were conducted under inert conditions in a batch reactor, using 1 (1 mmol), 2 (1.3 mmol), base (3 mmol), mpgCN$_x$ as catalyst (100 mg), MeCN as solvent (8 mL), light wavelength λ = 457 nm (128 W), temperature 45 °C, pressure 1 atm, and reaction time 60 min; [b]Determined by HPLC.

be uninfluenced by the Lewis base feature of KF, whose driving force seems to be limited by the base strength. The higher yield achieved with the stronger base is probably related to the increased re-aromatization rate in presence of these if compared to weaker base condition or no base condition. A study concerning the amount of TfCl was also conducted, with the best result being given by 1.3 equivalents (Table 4.1, entries 4, 5, and 6). This improved selectivity for the double alkylation product **4** in the presence of an enhanced amount of the trifluoromethylating agent (Table 4.1, entry 6) can be rationalized on the basis of

the enhanced formation and availability of CF_3 radicals. Thus, this parameter appears to be fundamental in discriminating between the mono- and di-trifluoromethylation products, heavily influencing the selectivity of the process. Additional control experiments were conducted in the absence of (i) light, (ii) an inert atmosphere, and (iii) catalyst in order to determine the importance of each parameter on the model reaction (Table 4.1, entries 7–10). Despite the relatively high conversions obtained in the absence of an inert atmosphere and without catalyst (Table 4.1, entries 7 and 8), the selectivity for the desired product **3a** dropped dramatically to less than 22%. Under these two conditions, selectivity for the undesired side product **5** increased drastically ($> 65\%$). The decreased selectivity for the trifluoromethylation product **3a** in the absence of an inert atmosphere can be accounted for through consideration of a CF_3 radical quenching mechanism mediated by atmospheric water.[214] Indeed, the same effect, observed when the reaction was conducted in absence of catalyst, confirms the key role of CN_x to specifically catalyze the trifluoromethylation reaction. The importance of the irradiation conditions was confirmed by conducting the reaction in the dark (Table 4.1, entry 9), where it was found that a conversion of only 17% was recorded. Further studies highlighted the importance of the power of the irradiation source on the trifluoromethylation reaction: using a traditional batch setup comprised of a LED strip (18 W) wrapped around a reaction flask (see Appendix A for details), the conversion only reached 64%, while the selectivity for product **3a** was equal to 6% (Table 4.1, entry 10). The employment of the more powerful reactor (128 W) led to a beneficial outcome on the reaction performance (Table 4.1, entry 4), comparatively higher than the one obtained using the home-made LED setup.

A trifluoromethylation reaction mechanism has been proposed involving the generation of the radical intermediate **7** (Figure 4.1), in line with the literature.[215] When the carbon nitride photocatalyst is irradiated with a photon source that exceeds the bandgap energy, the generation via single-electron transfer (SET) of a trifluoromethyl radical takes place, which selectively combines with pyrrole **1**. The catalyst-promoted oxidation of the radical intermediate **7** affords a 2-trifluoromethyl-2,3-dihydro-1H-pyrrolylium species **8**, which easily undergoes
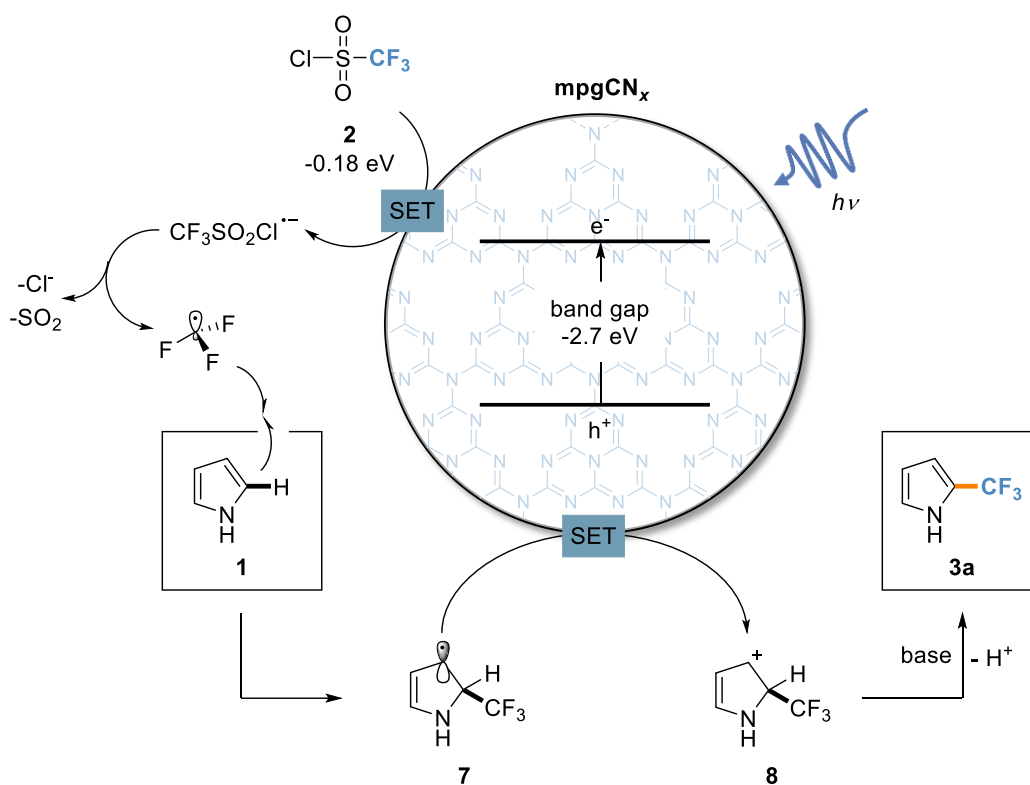
Figure 4.1. *Radical mechanism for the photocatalytic trifluoromethylation of pyrrole using mesoporous carbon nitride.*

deprotonation in presence of the base, affording the desired trifluoromethylated arene **3a**. This elucidates the central role of the base in the reaction. In order to obtain a more detailed understanding of the reaction mechanism, we conducted a kinetic study on the model compound (pyrrole).

The different carbon nitride analogues introduced in the previous section were thus tested, and the optimal reaction conditions in Table 4.1 were applied (vis-à-vis base, reactant equivalents, etc.). One of the key parameters differentiating the carbon nitrides from one another is their respective specific surface areas. Data collected from the kinetic study, conducted using the different carbon nitride catalysts with different surface areas, show a correlation between this intrinsic material property and the reaction progress (Figure 4.2 a,b). Particularly, gCN_x and nCN_x appear to have a similar behavior, providing low conversion and very low yield for the desired product **3** by promoting the formation of side product **5** (cf. Table 4.1). A different behavior is observed for the $mpgCN_x$ material, which provides the desired product in high yield. An overview of the species formation

trend during the kinetic study using the optimal catalyst is shown in Figure 4.2 c. The slight decrease in selectivity for the target product is due to the slow formation of the di-alkylated side product **4**, which becomes relevant only after the first hour. The improved conversion of pyrrole and the subsequent enhanced yield for the catalytic product provided by the mpgCN$_x$ catalyst could be easily justified with the increase of the surface area in this material, a key parameter in the light-catalyzed heterogeneous reaction, and considering that the optical properties in the three metal-free materials, *i.e.*, band gap and charge separation, are unaffected by the change of the tridimensional structure. Particularly, the mesopores present in the mpgCN$_x$ structures generates a tridimensional structure with enhanced surface area (>140 m^2 g^{-1}) if compared with the 2D graphitic (5 m^2 g^{-1}) and nanosheet (72 m^2 g^{-1}) samples; this structural effect leads to an increased contact between light, catalyst, and reactant, which is beneficial for the reaction outcome.[216] More detailed information regarding the formation of each side product in time is provided in the Appendix A.

Effect of the Catalyst Band Gap on the Trifluoromethylation Reaction. Given the excellent performance of mpgCN$_x$, we decided to use this photocatalyst to study the effect of band gap modulation on the catalytic activity, through the introduction of isolated metal centers.[217] In the literature, these metal-doped materials have shown enhanced catalytic properties for a number of energy-related reactions[218] and are starting to find applications in organic synthesis.[219] Metal insertion into the CN$_x$ framework leads to the creation of a joint electronic structure, which can in turn modify the band gap energy values, correlated also to the optical properties of the material.[220] By fine-tuning this property using metal atoms with different electronic properties, it is possible to precisely engineer the band gap value, which, for mpgCN$_x$, is around 2.7 eV (CB = -1.3 eV; VB = 1.4 eV). The presence of metal single atoms (specifically Zn, Cu, and Ag; metal-doped catalyst characterization is reported in Appendix A) appeared to have a detrimental effect on the yield of the desired product **3** (Figure 4.2 d). Specifically, a similar reaction progress was observed with the Zn- and Cu-based carbon nitrides, wherein a first predominant selectivity for the side product **5** was observed followed by a slow increase for the product **3** (steeper gradient with the Cu-based

material), which reached a value of 34% within 120 min. This led to overall yields of the desired product **3** that were far less superior to the undoped carbon nitride (42 and 34% for Zn- and Cu-based catalysts, respectively, versus 68% for mpgCN$_x$; Figure 4.2 d). On the other hand, the Ag-doped material displays a trend in both the conversion and yield that is quite similar to that of mpgCN$_x$. The following observations, when considered cumulatively, could explain the poorer performance of the Zn- and Cu- doped materials to yield the desired trifluoromethylated product **3** versus the bare mpgCN$_x$ support. First, the quenching of the photoluminescence (PL) spectra indicates the transfer of excited electrons to the single-atom sites (Figure 4.2 d and Figure A.4.3 c), in which the quenching follows the trend Zn@mpgCN$_x$ > Cu@mpgCN$_x$ > Ag@mpgCN$_x$ > mpgCN$_x$. Second, although the reaction vial is degassed prior to sample irradiation, a large quantity of the respective photocatalyst is employed (100 mg).
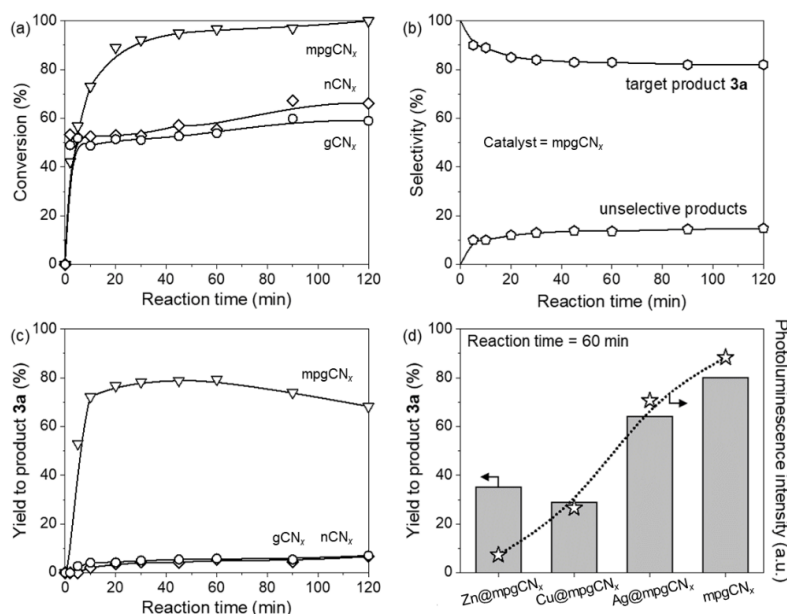
Figure 4.2. *Conversion (a), product selectivity (b), and yield of target product **3a** (c, d) over various CN$_x$ catalysts for the trifluoromethylation of pyrrole. Reaction conditions: 1 (1 mmol), 2 (1.3 mmol), catalyst (100 mg), K$_2$HPO$_4$ (3 mmol), MeCN as solvent (8 mL), light wavelength λ = 457 nm (128 W), temperature = 45 °C, and pressure = 1 atm. All data are determined by HPLC. The exact distribution of the (by)products is provided in the Appendix A.*

It has been discussed on several counts in the literature that the trapping of O_2 molecules within the mesoporous network of mpgCN$_x$, due to its incomplete elimination via simple N_2 degassing techniques, is indeed quite likely.[221] This residual presence of O_2 adsorbed by the mesoporous structure, coupled with the improved activation of molecular O_2 by metal single-atoms, could yield a higher concentration of reactive oxygen species (ROS) within the local environment.[222] Thus, the formation of this intermediate could in turn explain the increased selectivity for the hydroxylation of pyrrole (generating side product **5**) when Zn@mpgCN$_x$ and Cu@mpgCN$_x$ are employed in accordance with the enhanced electron transfer to the respective metal site in these materials.

Development and Optimization of a Scalable Continuous-Flow Process. Succeeding the batch investigations that provide novel detailed information about the structure–performance relationship, the design of a sustainable processes was performed, developing a continuous-flow route for the trifluoromethylation process (Figure 4.3) in which the photocatalyst was housed within a fixed-bed reactor. The photoreactor setup was assembled using a transparent FEP tube (length = 500 mm, i.d. = 2.1 mm), which was packed with mpgCN$_x$, K_2HPO_4, and glass beads (2.5 wt %). The use of the latter as a co-packing material in the bed reactor facilitated catalyst particle separation and dilution, which was necessary to reduce the competition for the absorption of visible-light photons. Evidence supporting this positive effect can be found by conducting the reaction in absence of glass beads and using sand to dilute the catalyst in the reactor. The unfavorable contact with light provided in these conditions led us to obtain product **3a** in only 58% yield. At first, we decided to optimize the reaction protocol starting from the evaluation of the light wavelength effect on the model reaction (Figure 4.3 a). The better performance of the catalyst in the presence of blue light (457 nm) is due to the proximity of the onset of absorption band of CN$_x$ with this wavelength. To investigate the reaction progress in continuous-flow mode, we evaluated the formation of trifluoromethylpyrrole **3a** screening different residence time conditions (Figure 4.3 b). From 10 to 20 min, a reasonable yield increase was observed (respectively 23, 45, and 77%), followed by a subsequent decrease of up to 30 min (67 and 64%) related to the enhanced formation of the di-

trifluoromethylated pyrrole **4** at longer reaction times. Choosing 20 min as the optimal residence time, comparative data between the batch and flow process with this reaction time show a similar yield between the two approaches (Table A.4.3); the real advantages related to the continuous-flow protocol are the easier recyclability of the catalyst and the productivity enhancement. The stability of the heterogeneous photocatalyst was evaluated by running the continuous-flow reaction over 5 h on stream (Figure 4.3 c). This has been carried out under kinetic conditions, prolonging the injection time of the solutions and evaluating the yield variation in time. The result demonstrates the excellent stability of $mpgCN_x$ with no activity loss, also confirmed by further characterization of the material after use (see the Appendix A). It must be remarked that, given that the residence time of the fluid flowing through the reactor is 20 min, the steady-state operation for 5 h is equivalent to 15 catalytic cycles in a batch reactor. With the optimized conditions in hand, a continuous-flow scaled-up experiment was performed for a
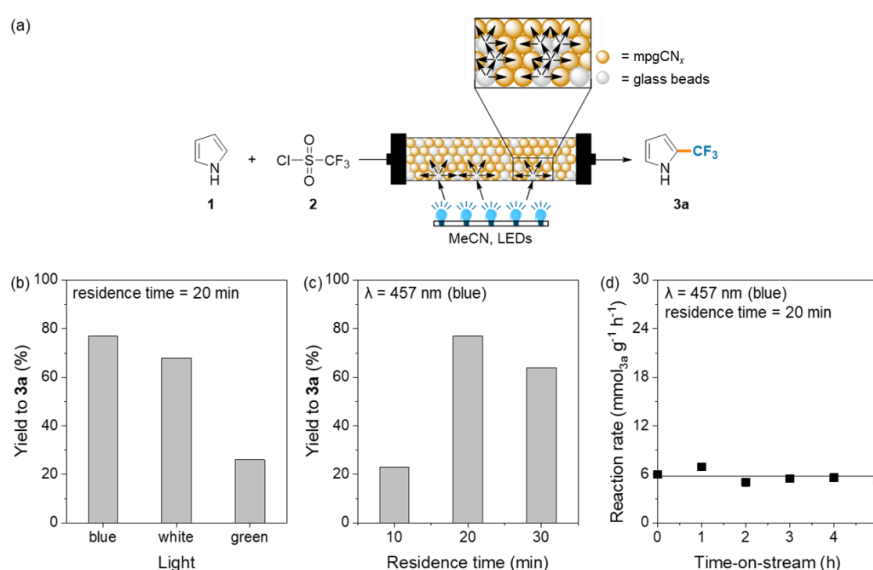
Figure 4.3. General scheme for the continuous-flow trifluoromethylation of pyrrole (a), effect of light source wavelength (b), effect of residence time (c), and catalyst stability study (d). Reaction conditions for the flow reaction: 1 (1 mmol, 0.25 M in MeCN), TfCl (1.3 mmol, 0.25 M in MeCN), various light wavelengths (blue λ = 457 nm, green λ = 550 nm, or white 400–700 nm), temperature = 45 °C, pressure = 1 atm. All data are determined by HPLC.

prolonged time (5 mmol), obtaining the target product **3a** in 62% yield and with a production rate of 0.62 mmol h^{-1}, doubling the batch performance (production rate in batch = 0.32 mmol h^{-1}). The enhancement in the productivity under flow conditions is justified by the high light intensity in the microreactors and irradiation condition uniformity provided by this configuration compared to the poorly designed batch conditions for conducting a heterogeneous photocatalytic reaction.[108,124]

Finally, the influence of heteroaromatic reactivity and the substitution pattern toward the trifluoromethylation reaction has been evaluated using different
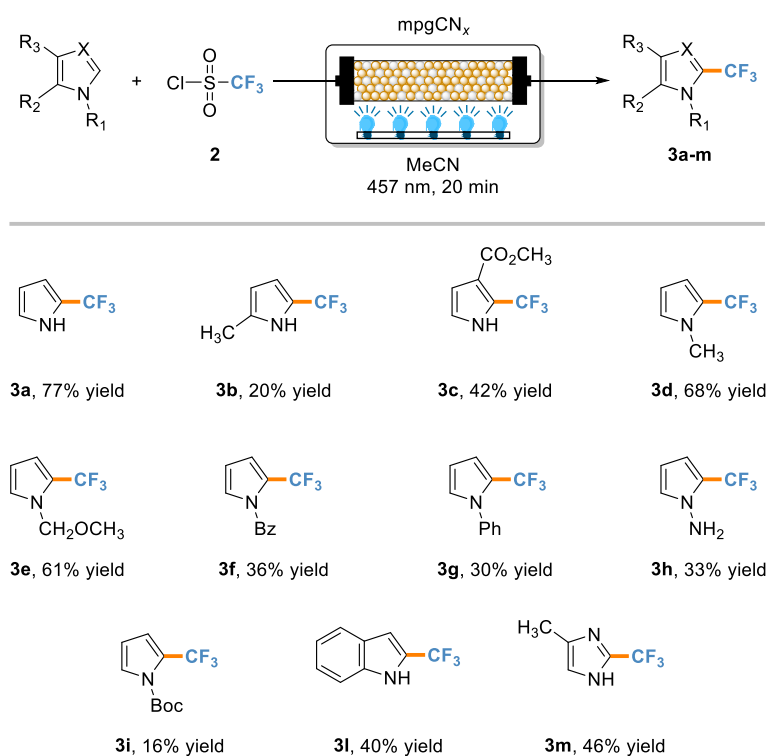
Scheme 4.1. *Substrate Scope for the Continuous-Flow Trifluoromethylation of (Hetero)arenes.[a]Reaction conditions: (hetero)arene (1 mmol, 0.25 M in MeCN), TfCl (1.3 mmol, 0.25 M in MeCN), temperature 45 °C, pressure 1 atm, residence time τ = 20 min. The packed-bed reactor was filled with a mix of mpgCN$_x$ (50 mg), K$_2$HPO$_4$ (3 mmol), and glass beads (2 g) to better spread the light irradiation through the catalyst bed. The yields are calculated via NMR using dibromomethane as an internal standard.*

substrates (Scheme 4.1). All pyrrole-based substrates performed with moderate to good yield. 2-Methyl **3b** (20% yield) and methyl-3-carboxylate **3c** (42% yield) exhibited lower reactivity, slightly offset by the electron-withdrawing effect of the ester group in the latter. The fluoroalkylation of nitrogen-substituted pyrroles occurred with good yield (compounds **3d**–**3h**, 30–68% yield) with a particular preference for substrates bearing weak electron-donating groups due to the mesomeric stabilization of the heteroaryl radical. This is further supported by compound **3i**, in which the withdrawing effect of the protecting group led to a decrease of the reaction performance (16% yield), related to the negative impact on the heteroaryl radical stability. The protocol has been also tested on different N-bearing heterocycles, namely, indole **3l** (40% yield) and indazole **3m** (46%). However, in the latter cases, the reaction suffered from the possibility of multiple alkylation positions with the formation of regioisomers, with 12% yield for the alkylation in C3 of the indole, and 23% yield for the C4 alkylation of the indazole.

4.4. Conclusions

In conclusion, we have studied the effect of carbon nitride structuring on the visible light-photocatalyzed introduction of trifluoromethyl moieties. A direct correlation between the product yield and surface area has been demonstrated. The material with the highest surface area (*i.e.*, mpgCN$_x$) has been further fine-tuned, introducing several isolated metals within the carbon nitride lattice to modulate the catalyst bandgap. The photoluminescence characterization of the samples has shown that electron transfer from the metal site favors the generation of reactive oxygen species, resulting in competing side-reactions involving the hydroxylation of pyrrole. These insights were exploited for the development of a continuous-flow process that remains selective and stable over long reaction times. Overall, the work demonstrates the advantages of metal-free catalysis and flow reactor technology for the synthesis of pharmaceutical intermediates in an on-demand, high-throughput fashion.

Chapter 5

Ag single atoms on carbon nitride enabling ligand-free photocatalytic oxidations

5.1. Introduction

The development of selective catalytic methods for pharmaceutically relevant transformations is essential for advancing a green economy but represents a major challenge in the field of chemistry. This challenge is due to the requirements of high selectivity, minimal utilization of expensive and toxic reagents, and the need to reduce energy consumption and pollution.[223,224] The selective oxidation of benzyl alcohol to benzaldehyde is one of the important chemical processes widely used to produce intermediates for fragrances, perfumes, and dyes.[225,226] Unfortunately, traditional methods for achieving this transformation, including liquid-phase chlorination and hydrolysis of toluene, or direct oxidation of alcohols using toxic oxidants such as MnO_4^-, $Cr_2O_7^{2-}$, and Cl_2, require high temperatures and pressures, and produce toxic byproducts that are harmful to the environment.[227] The photocatalytic oxidation of benzyl alcohol to benzaldehyde using O_2 or air as oxidants at room temperature has attracted much attention

recently.[225,228–230] Various photocatalysts have been studied, showing nearly full selectivity to the formation of benzaldehyde.[231] However, surface recombination of photo-induced charge carriers may slow down the reaction kinetics. To address this, metal nanoparticles have been added to these oxides as co-catalysts, with Pt-group noble metals playing a prime role.[232] Recently, the attention has shifted to using atomically-dispersed metals, leading to the creation of single-atom catalysts.[233,234] These new catalysts, consisting of isolated metal atoms supported on various substrates, exhibit unique electronic properties and high surface area, resulting in enhanced catalytic performance.[123,132,219] They also offer tunable degrees of selectivity for specific reactions by adjustment of the type, concentration, and speciation of metal sites. Nevertheless, to maintain a stable catalytic performance, it is often essential to load over 1% weighted Pt-group single atoms on TiO_2.[235] Besides, the limited photoactivation of TiO_2-based photocatalysts outside the UV region restricts their versatility.[236] The development of photocatalysts that are sensitive to visible light is a necessity for the design of energy-efficient processes able to utilize solar energy. Many efforts have been devoted in this direction: Bi_2WO_6 with the octahedral structure layer and a narrow band gap of 2.8 eV has shown promising applications in the oxidation of alcohols to aldehydes, but the complex procedures and high costs involved in preparing (modified or bare) Bi_2WO_6 make it inappropriate for large-scale applications.[237] Conjugated polymers are another class of visible-light-driven organic semiconductor photocatalyst that shows promise due to their photoactive π-conjugation structure and high specific surface area nanopores.[238,239] Their semiconductors bandgap structure is determined by the intrinsic attributes of polymerized monomers, which allows for the design of polymer photocatalysts with visible-light response. Recent studies show that combining certain donor and acceptor units can result in polymers with high photocatalytic activity due to the reasonable design of the bandgap structure and boosted separation of photogenerated electron-hole pairs.[238] Among those, carbon nitrides are a class of stable polymers where the immobilization of isolated metals can enhance the photocatalytic activity under visible light illumination.[216,219] However, such

catalyst was never used for the photocatalytic oxidation of benzyl alcohol to benzaldehyde.

In this work, we report an Ag-based single-atom catalyst for the oxidation of benzyl alcohol to benzaldehyde. Kinetic tests and density functional theory (DFT) calculations were employed to rationalize the catalyst structure and confirm the proposed reaction mechanism. Continuous-flow conditions were finally used to assess the scalability potential of the method.

5.2.   Experimental

Catalyst Synthesis. All chemicals in this study were purchased from Sigma-Aldrich and used as such, without any further purification. The Ag-based single-atom catalyst was prepared via copolymerization. An aqueous solution of $AgNO_3$ (1.70 g, 10 mmol; in 10 mL of deionized water) and an aqueous solution of sodium tricyanomethanide (1.13 g, 10 mmol; in 10 mL of deionized water) were mixed and stirred for 3 h at room temperature. The mixture was then filtered to recover the solid silver(I) tricyanomethanide salt, washed with water (3 × 10 mL), and subsequently dried in vacuum (7 mbar, 50 °C). The obtained salt (37 mg, 0.015 mmol) was mixed with a 40% aqueous dispersion of 12 nm SiO_2 particles (7.5 g, Ludox HS40) and cyanamide (3.0 g, 70 mmol). The mixture was stirred at 70 °C for 16 h until complete water evaporation. The obtained solids were calcined to 550 °C for 4 h, using a heating ramp of 2.2 °C min^{-1}. Silica template etching was performed washing the solid with an aqueous NH_4HF_2 solution (12 g in 50 mL of deionized water) at room temperature for 24 h. The resulting suspension was filtered, and the powder was washed three times with water and ethanol. Finally, the product was dried under vacuum at 60 °C overnight.

Catalyst Characterization. Powder X-ray diffraction (XRD) was performed on a Philips model PW3040/60 X-ray diffractometer using Cu Kα radiation (λ = 0.15418 nm). Nitrogen physisorption measurements were performed after degassing the samples at 150 °C for 20 h using a Micromeritics 3Flex porosimeter at 77 K. The specific surface areas were calculated by applying the Brunauer–Emmett–Teller (BET) model to adsorption isotherms for $0.05 < p/p_0 < 0.3$ using

the QuadraWin 5.05 software package. The pore size distribution was obtained by applying the quenched solid density functional theory model for N_2 adsorbed on carbon with a cylindrical pore shape at 77 K. Elemental analysis (CHNS) was accomplished by combustion analysis using a Vario Micro device. An inductively coupled plasma optical emission spectroscopy (ICP-OES) study was performed using a HORIBA Ultra 2 setup equipped with photomultiplier tube detection. X-ray photoelectron spectroscopy (XPS) was conducted using a Physical Electronics Instruments Quantum 2000 spectrometer with monochromatic Al Kα radiation generated from an electron beam operated at 15 kV and 32.3 W. All spectra were referenced to the C 1*s* peak of adventitious carbon at 284.8 eV. High-resolution transmission electron microscopy (HRTEM) analysis was performed over a Titan G2 60-300 microscope (FEI), using an X-FEG-type emission gun at 300 kV.

Catalytic Tests. The photocatalytic oxidation of benzyl alcohols was performed using the Illumin8 parallel photoreactor purchased from Asynt (UK), equipped with DrySyn OCTO MINI 8-position reaction station, standard hotplate magnetic stirring, and a cooling system to control reaction temperature. In a typical procedure, benzyl alcohol (19.5 mg, 0.18 mmol) was mixed with 5 ml of solvent and 5 mg of catalyst. The reaction flask was irradiated with blue light ($\lambda = 450$ nm, with 10 W LED COB chips) under continuous stirring (400 rpm) for the whole reaction time. All reactions were performed at 30 °C, varying the reaction time between 5- and 240-min. Control experiments with and without catalyst were performed in dark under similar experimental conditions. Reaction products were analyzed via gas chromatography (GC) equipped with a flame ionization-mass spectroscopy detector and ^{1}H NMR. The detection was done using two columns, HP- INNOWAX (5 m × 0.250 mm × 0.15 μm) and DB-5MS (20 m × 0.180 mm × 0.18 μm), connected in series. Quantification was performed after the calibration of the GC with the commercial standards. Products characterization is included in Appendix A.

Computational Details. Spin-polarized DFT calculations were performed with the VASP[240] code using the generalized gradient approximation, as implemented in the Perdew–Burke–Ernzerhof (PBE) functional.[241] Dispersion forces have been

included according to the Grimme's D3 parametrization.[242] The valence electrons have been expanded on a set of plane waves with a kinetic energy cutoff of 400 eV, whereas the core electrons were treated with the projector augmented wave approach (PAW).[243] The threshold criteria for electronic and ionic loops were set to 10^{-5} eV and 10^{-2} eV Å^{-1}, respectively. The sampling of the reciprocal space was reduced to the gamma point because of the cell size. We considered a corrugated CN_x layer characterized by heptazine pores and we optimized the lattice parameters (a = 13.846 Å, b = 13.846 Å, γ = 120°).[244] We also modelled another possible coordination of the silver atom, a nitrogen-doped graphene model, obtained by creating a carbon divacancy of a 4x4 graphene supercell (a = 9.872 Å, b = 9.872 Å, γ = 120°), and replacing 4 carbon atoms with nitrogen ones.[245] The binding energies (ΔE) of each intermediate were calculated with respect to the free molecular species and catalyst. The Gibbs energies (ΔG) were evaluated by adopting the thermochemistry approach of Nørskov and co-workers including zero-point energy correction and entropy terms.[246,247] The first were calculated within the harmonic approximation. Entropies of gases were taken from the international tables, and the entropy of solid-state species were considered equal to zero.[247]

$$\Delta G = \Delta E + \Delta E_{ZPE} - T\Delta S \qquad\qquad\qquad\qquad (Eq.\ 1)$$

5.3. Results and Discussion

The Ag-doped carbon nitride (Ag@mpgCN$_x$) was characterized to determine its structural properties. Crystallinity and purity of the prepared catalyst were evaluated through XRD analysis (Figure 5.1 a).[248] Two typical diffraction peaks at 2θ = 13° and 28° were found, corresponding to the *N*-linkage of the tri-*s*-triazine motif and to the π–π stacking of aromatic structures in the support, respectively. Porosity, pore volume, and surface area of the material were determined by N_2 physisorption experiments (Figure 5.1 b, Table 5.1). In particular, the analysis evidenced the relatively high Brunauer−Emmett−Teller (BET) surface area of Ag@mpgCN$_x$ (174 m^2 g^{-1}), consistently with previous reports,[212] and the

mesoporous nature of the fabricated material. The elemental composition of the catalyst was elucidated by CHNS and ICP-OES experiments (Table 5.1). The C/N ratio, resulting from the CHNS elemental analysis, was close to 0.65, which is the reference value for tri-s-triazine-derived mpgCN$_x$ carriers.[213] The ICP-OES analysis, instead, proved the effective incorporation of the metal on the support, with a total metal loading of 0.3 wt.%. High-resolution transmission electron microscopy (HRTEM) micrograph of Ag@mpgCN$_x$, at a magnification of 5 nm further demonstrated the absence of any large metal aggregation and the high dispersion of the metal phase (Figure A.5.1 a and b). Moreover, the bright-field
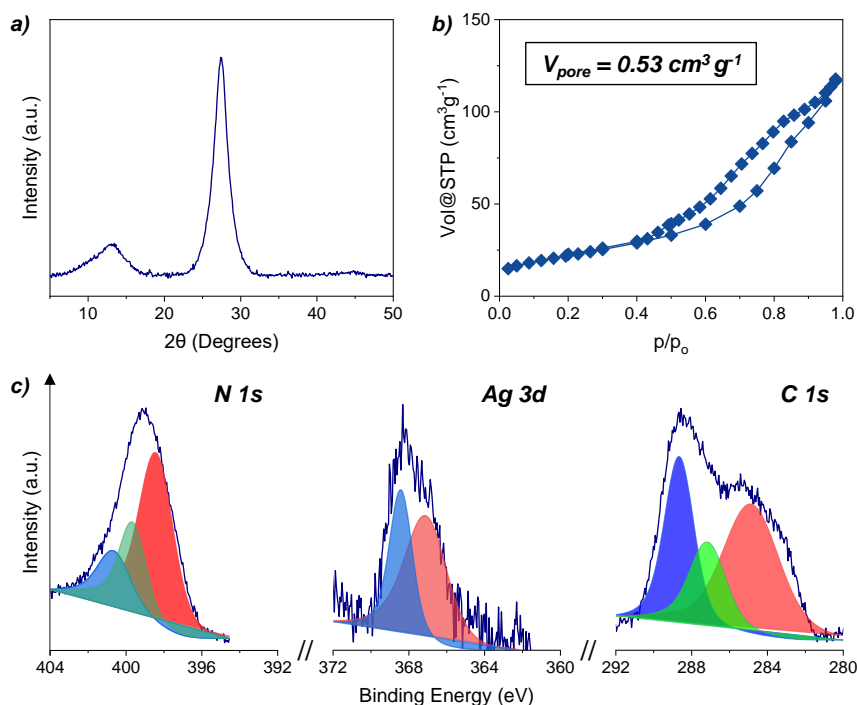
Figure 5.1. *Characterization of Ag@mpgCN$_x$: X-ray diffraction pattern (a), N$_2$ physisorption isotherm with the corresponding pore size distribution as an inset (b), C 1s, N 1s, and Ag 3d X-ray photoelectron spectroscopy (c).*

Table 5.1. *Elemental composition and textural properties of Ag@mpgCN$_x$.*

Catalyst	C^a (wt %)	N^a (wt %)	H^a (wt %)	C/N (-)	Metal^b (wt.%)	S_{BET}^c (m^2 g^{-1})	V_{pore}^d (cm^3 g^{-1})
Ag@mpgCN$_x$	31.01	47.43	2.40	0.65	0.30	174	0.53

^{a}CHNS. ^{b}ICP-OES ^{c}N$_2$ isotherm collected at 77 K. ^{d}Quenched solid density functional theory model assuming cylindrical-shaped pores.

HRTEM analysis corroborated the effective presence of mesopores in the sample. X-ray photoelectron spectroscopy (XPS) was employed to evaluate the oxidation state of the elements (C, N, and Ag) constituting our catalyst (Figure 5.1 c). In the N $1s$ spectra, three peaks are derived from the deconvolution of the experimental signal. The peak at 398.4 eV is related to the C=N–C nitrogen in the pyridinic structure of mpgCN$_x$; the one at 399.4 eV is assigned to the presence of tertiary C=N–C$_3$ nitrogen. The peak at 401.4 eV corresponds instead to primary amine groups coming from polymerization defects in the carrier. The XPS Ag $3d$ spectra shows two main peaks at 368.4 (Ag$^+$) and 367.2 eV (Ag^0), confirming the coexistence of these two oxidation states for the metal. The XPS C $1s$ spectra presents three peaks: the first (284.8 eV) is assigned to both adventitious carbons and energy calibration sp^2 carbon; the second (285.9 eV) is related to sp^3 C−C bonds; the last one (288.4 eV) corresponds to N–C=N carbons in the aromatic structure of the carbon nitride.[216]

The Ag@mpgCN$_x$ catalyst was exploited in the photocatalytic conversion of benzyl alcohol into benzaldehyde. We started our investigation by conducting control experiments in the absence of any light and catalyst, as shown by the

Table 5.2. *Reaction scheme: standard conditions and control experiments.*

Entry[a]	Control experiment	Yield[d] (%)
1	No light[b]	-
2	No photocatalyst[c]	-
3	No air (inert atmosphere)[b,c]	29
4	As shown[b,c]	67

[a]Conditions: benzyl alcohol concentration = 37 mM. [b]Ag@mpgCN$_x$ used as photocatalyst. [c]Photoreactor set to blue light irradiation. [d]Conversion and yield were computed via GC, with a calibration curve.

results in Table 5.2 (Entries 1 and 2). In both cases, no reaction was observed. Then, the role of air in driving the benzyl alcohol oxidation, providing reactive oxygen species, was confirmed by performing the reaction in the absence of the
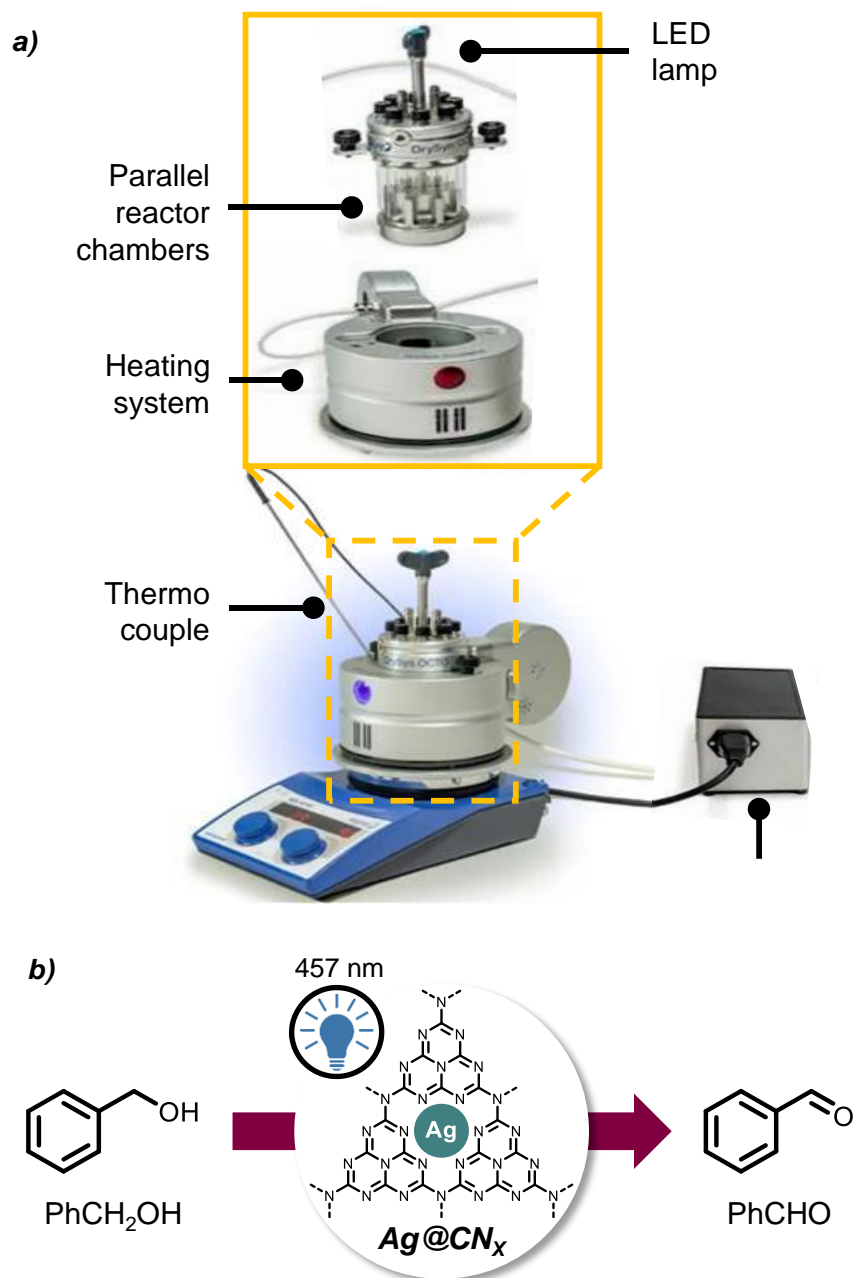
Figure 5.2. DrySyn OCTO MINI 8-position reaction station (a) and conditions (b) used in this study. General conditions: benzyl alcohol (0.19 mmol), catalyst (5 mg), solvent (5 mL), light wavelength λ = 457 nm, temperature 30 °C, reaction time 30 min (unless expressly specified). All data are determined by GC.

same, under N_2 atmosphere (Entry 3). The yield dropped to 29%, and the minimal formation of product was likely due to the presence of residual oxygen in the solvent. Only when blue light, the Ag@mpgCN$_x$, and air were added to the reaction vessel, the reaction gave benzaldehyde with 67% yield.

To probe the effect of the solvent properties on the reaction progress, several solvents were then examined using visible-light irradiation (450 nm) for 30 min. Notably, acetonitrile, cyrene, and water were selected as benchmarks for this investigation, being greener alternatives to commonly used organic solvents (Figure 5.3 a).[249] The experiment produced comparable yields using acetonitrile and cyrene, which were 53% and 49%, respectively. This result can be attributed to the comparable polarity of the solvents (relative polarity accounting to 0.46 and 0.33 for acetonitrile and cyrene respectively).[250] However, the water showed a slightly lower yield of 40%, which can be well explained by the moderate solubility of the product in water.[251] In addition to these steady-state catalytic tests, we performed a transient analysis to monitor the product formation over time. For this purpose, we employed the same batch reactor that allowed us to track the evolution of the products without altering the irradiation of the reaction vessel. This approach provided us with valuable insights into the reaction kinetics and allowed us to identify the optimal reaction conditions for maximizing the product yield. Upon increasing the reaction time from 5 min to 60 min, the benzyl alcohol conversion increased from 18% to 100% and the benzaldehyde yield reached 85% (Figure 5.3 b). After this time, the competitive formation of benzoic acid takes place, leading to a decrease of selectivity for the benzaldehyde. Such transient analysis complemented the steady-state experiments and provided a more comprehensive understanding of the catalytic system. Finally, the optimal stability of the Ag-based material was assessed by means of a recyclability test, composed by three reaction cycle. After each oxidative experiment (30 min), the catalyst was filtrated, washed, dried, and reused. As depicted in Figure 5.3 c, no significant decrease of the benzyl alcohol conversion and benzaldehyde yield were observed during several reaction cycles, suggesting that the chemical and structural properties of the material were retained during the photooxidation of benzyl
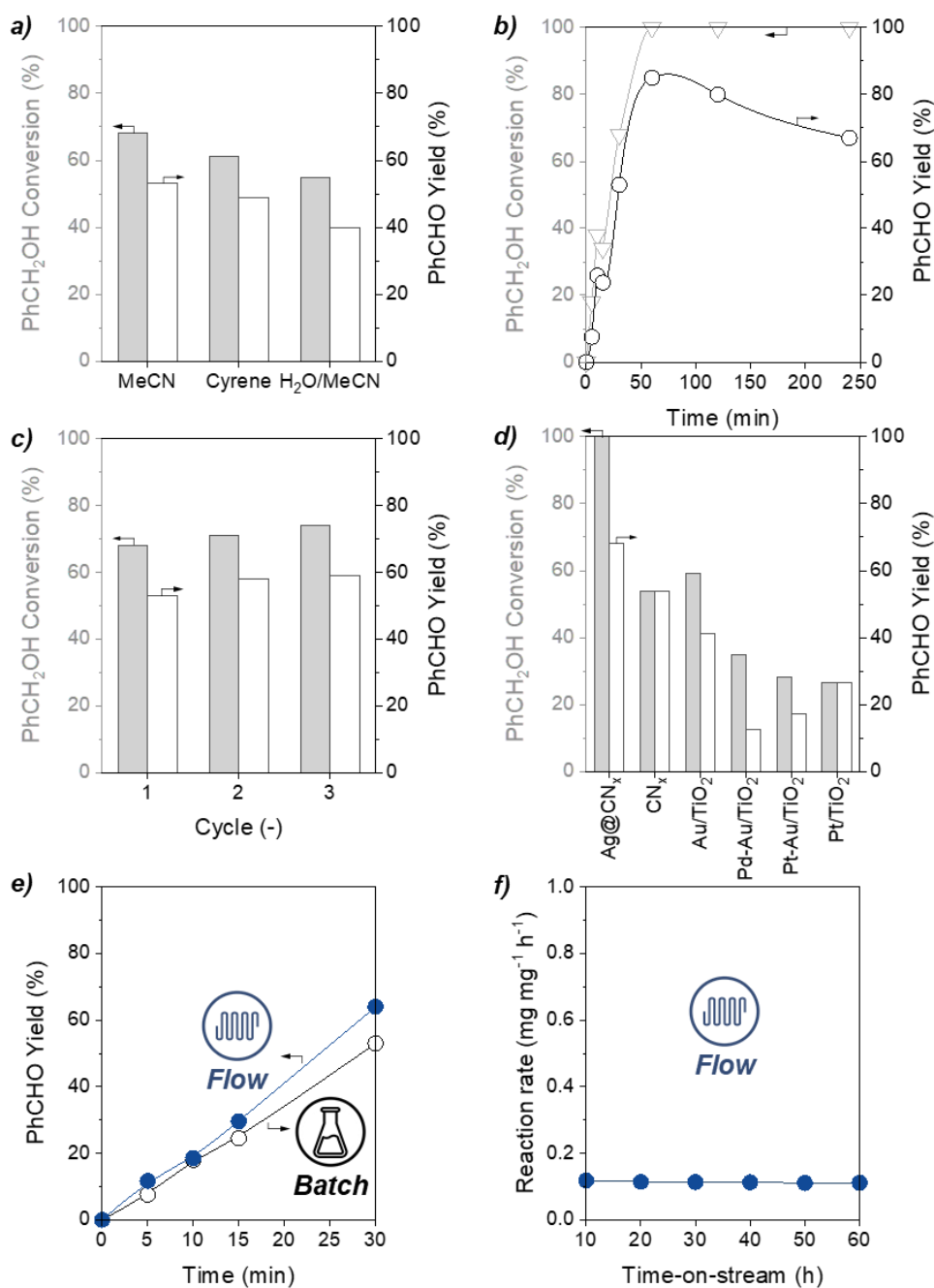
Figure 5.2. *Solvent screening for the reaction in the presence of blue light irradiation (a); time-dependent rate for the oxidation reaction (b); recycling experiment performed under standard conditions for 3 catalytic cycles (c); comparison of different catalytic systems (d). Comparison between batch and flow oxidation of benzyl alcohol (e) and continuous-flow time-on-stream experiments (f).*

alcohol. This was further confirmed by the full characterization of the used catalyst

provided in the Appendix A. We also investigated other catalytic systems to remark the optimal performance of our photocatalyst, and demonstrate the advantages from the use of a fully integrated Ag-doped single-atom system (Figure 5.3 d). First of all, the metal-free carbon nitride was tested on the reaction at the optimal reaction conditions identified above, to understand the effect of the metal doping of the material. The decreased photocatalytic performances of the mpgCN$_x$ highlights the role of silver in the catalysis, promoting and enhancing the oxidation reactions.[252,253] The superior photocatalytic performances showcased by the single Ag atom-doped material, when compared with the bare mpgCN$_x$ support, are related to ligand-to-metal charge transfer (LMCT) phenomena, that lead to enhanced electron transfer from the support to the metal surface, thus increasing the electron flux from the catalyst to the substrate.[212] The CN-based support was then substituted with TiO$_2$, a benchmark photoactive support, and doped with several metals, namely Au, Pd/Au, Pt/Au, and Pt. In all cases, benzaldehyde was obtained in lower yields, even in the presence of Au-doped material, where it is accepted that plasmonic effect are present, resulting in light absorption and hole carrier quenching from the nanoparticles, with potential higher energy transfer from the catalyst to the substrate.[254]

These outstanding results of Ag@mpgCN$_x$ were explained via DFT calculations. In particular, given the presence of possible defects in carbon nitride-based materials, the metal atom was studied in different sites of CN$_x$, in particular coordinated with the N atoms of a triazine pore (Figure 5.4 a), and in a N-doped defect cavity (Figure 5.4 b). In both configurations the metal atom assumes a formal Ag$^+$ state, as can be evinced from the analysis of the density of states and spin density, and in agreement with our XPS characterizations. From these structures, it is possible to appreciate that the electronic metal configuration is compatible with a $4d^{10}5s^0$, and the latter indicates that the charge donated by the metal is delocalized over the conduction band of the support. The calculated adhesion energies are -1.66 eV and -2.40 eV for CN$_x$ and 4N-Gr respectively, showing that Ag is more strongly bounded to the support in the second case.[244] In CN$_x$, another possible minimum is represented by the metal atom on top of a nitrogen atom. In this case, the metal is weaklier bounded to the support (E_{ad} = -

0.67 eV). In terms of local structures, Ag in the pore is coordinated by 5 N atoms, with Ag-N distances in the range 2.40-2.60 Å. Ag in 4N-Gr is coordinated by 4 N atoms, with $d_{Ag-N} = 2.00$ Å. On these two structures representing the coordination of the single metal atom within the mpgCN$_x$ carrier, we modelled the oxidation of benzyl alcohol to benzaldehyde. The reaction is formally an oxidation involving two monoelectronic reaction steps, each releasing a proton and an electron. We considered the following reaction path, taken from previous DFT studies of the oxidation of alcohols to aldehydes on metal-based catalysts.[255]

$$PhCH_2OH + * \rightarrow PhCH_2OH^* \tag{Eq. 2}$$

$$PhCH_2OH^* \rightarrow PhCH_2O^* + H^+ + e^- \tag{Eq. 3}$$

$$PhCH_2O^* \rightarrow PhCHO^* + H^+ + e^- \tag{Eq. 4}$$

$$\Delta PhCHO^* \rightarrow PhCHO + * \tag{Eq. 5}$$

The first step is the adsorption of the reactant on the single metal site, PhCH$_2$OH*. Then, the first proton and electrons are released, giving PhCH$_2$O*. Next, a second proton and electron release take place, yielding PhCHO*. Finally, the product is desorbed from the single-atom catalyst. Figure 5.4 c shows the Gibbs free energy profile calculated at $T = 298$ K. The reaction is nearly isoergonic since the process PhCH$_2$OH $\rightarrow$ PhCHO + 2H$^+$ + 2e$^-$ gives ΔG = -0.02 eV. Starting from the case of Ag coordinated to CN$_x$, the benzyl alcohol is weakly physisorbed (ΔG = -0.07 eV), and the first hydrogen release requires a barrier of 0.75 eV. The subsequent step is favourable, leading to an adsorbed benzaldehyde nearly as stable as the separated product and single-atom catalyst. The profile is similar when considering Ag@4N-Gr but with an higher reaction barrier (1.07 eV) due to the stronger coordination of the single-atom catalyst to the support and consequently lower reactivity.[219] Interestingly, the reaction is expected to be extremely unfavourable without the catalytic action. Indeed, the barrier to form the same reaction intermediate increases to 1.75 eV, suggesting the important role played by the light and Ag@mpgCN$_x$ catalyst.
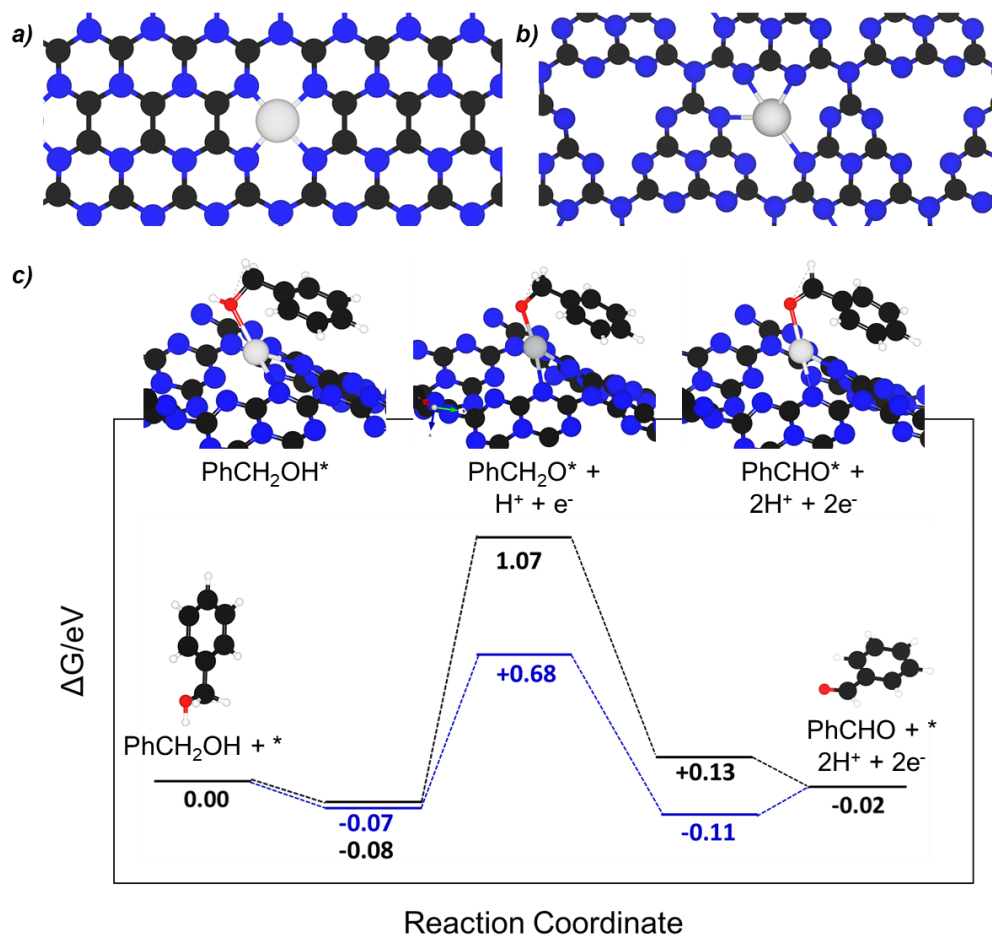
Figure 5.4. Atomistic structure of the Ag-based catalysts (a and b). Calculated Gibbs free energy profile of the oxidation of $PhCH_2OH$ to $PhCHO$ (c).

With the optimal conditions in hand, and after the in-depth investigation on reaction mechanism, we decided to prove the flexibility of the protocol for the oxidation of several primary and secondary alcohols, reported in the Appendix A.

Finally, we focused on the scale-up of the process. In particular, the continuous-flow technology was adopted in order to provide a uniform radiation distribution inside the reactor, and satisfy the constraints imposed by the Beer-Lambert Law for photoinduced chemical transformations. The packed-bed reactor design and the porous framework of the mesoporous graphitic photocatalyst offered a unique environment to meet these requirements and scale-up the process, minimizing the mass transfer limitation of the multicomponent reaction. Also, the use of glass beads as a co-packing material in the bed reactor facilitated catalyst particle separation and dilution, which was necessary to reduce the competition for the

absorption of visible-light photons. Kinetic studies conducted under such flow conditions showed an increase in the production rate of the desired model compound, compared to the batch method (Figure 5.3 e). This improvement, coupled with both the stability of the catalyst (as verified by time-on-stream analysis, Figure 5.3 f) and the facile recyclability of the photocatalytic system highlighted the importance of continuous-flow reactor design for the scale-up of the SACs-based photocatalyzed process.

5.4.   Conclusions

This study has explored the use of single-atom silver catalysts for photocatalytic oxidation of benzoic acids without ligands or organic additives, and using visible blue light. The high surface area of mesoporous graphitic carbon nitride allowed for the stabilization of a high density of single-atom reaction sites, leading to a 2-fold enhancement in catalytic activity compared to metal-based commercial TiO_2 photocatalysts. The mechanism of the reaction was rationalized by density functional theory calculations and operando nuclear magnetic resonance spectroscopy supported the theoretical predictions. The study was also extended to continuous-flow conditions, showing potential for industrial implementation in the synthesis of other aldehyde intermediates.

Chapter 6

A Bijel-Based Microreactor Confining Carbon Nitride for Continuous Photocatalytic Applications

Sivo, A.; Allasia, N.; Nevskyi, O.; Marelli, M.; Vanoli, V.; Fusi, N. C.; Jody Albertazzi, J.; Busini, V.; Castiglione, F.; Savateev, O.; Rossi, F.; Vilé, G. *Nat. Chem. Eng.* **2023**, *Submitted.*

6.1. Introduction

Heterogeneous photocatalysis has emerged as a powerful tool in contemporary chemistry, offering transformative prospects for sustainable chemical processes and environmental remediation.[256–258] The versatility of this approach stems from its capability to exploit light to induce chemical reactions using solid-state catalysts. These materials not only manifest superior photostability but also demonstrate reduced usage of transition metals when compared to their homogeneous (organometallic) counterparts.[221,259,260] Within the domain of

traditional chemical engineering, packed beds are the preferred choice for implementing solid-state catalysts within industrial reactors.[261] The rationale behind this preference lies in the ability to accommodate catalysts in granular form, overcoming the challenges posed by finely dispersed powdered catalysts commonly utilized in slurry reactors.[262–264] Granular catalysts within packed beds circumvent issues related to catalyst separation and recovery, while simultaneously reducing pressure drops within the reactor. These attributes collectively contribute to a higher reactor performance and better operational stability. Nevertheless, when considering heterogeneous photocatalysis, the adoption of packed-bed reactors introduces a distinctive challenge centred on energy transfer limitations. The confined energy transfer inherent within packed beds can hinder the propagation of photogenerated energy to the catalyst, and this can compromise the overall efficiency and effectiveness of the photocatalytic process.[265,266] Several strategies have emerged to overcome this challenge. For instance, depositing catalysts within micromixer frameworks, nanofibers, or membranes enhances mass transfer and facilitates effective light interaction.[133,267] However, this approach may result in the catalyst layer detaching during extended reaction times. Another method involves reducing the diameter of the packed bed to create a microthin reactor, thereby improving light transfer efficiency.[268,269] As an alternative, dispersing glass beads among catalyst particles can help diffuse light within the internal sections of the packed bed, mitigating irradiation limitations.[121] Nevertheless, controlling the precise placement of these glass beads is often challenging and can lead to less predictable processes. Despite their inherent limitations, these solutions have collectively paved the way for enhanced photocatalytic performance in the realm of heterogeneous catalysis. However, the incorporation of heterogeneous photocatalysis within a structural (foam-based) configuration remains unexplored, and the utilization of polymer conjugation and catalyst integration through in situ copolymerization presents a promising approach to address these challenges, leading to the creation of novel types of packed bed photoreactors and allowing precise tuning of the absorption properties of the photocatalytic material.

In particular, bicontinuous interfacially jammed emulsion gels, referred to as bijels, are emerging as a transformative material with extensive implications across diverse domains including separation membranes, drug delivery, and energy-storage technologies.[270–272] These materials boast a distinctive 3D architecture, comprising interpenetrating domains enriched with nanosized particles that harmonize at the interface. The resultant stabilization mechanism effectively reduces interfacial tension at the liquid-liquid junction.[273,274] The porous morphology, resulting from the immiscible phase interpenetration, can be finely tailored by manipulating nanoparticle size and concentration during synthesis. Although these materials have never been applied in photocatalysis, we envisioned that by incorporating an array of photoactive particles, including graphitic and mesoporous carbon nitride and the respective single-atom photocatalysts, customized matrices could be attainable, underlining their promise for multifunctional roles in catalysis.[89]

In this study, we thus unveil an innovative paradigm by introducing a bijel-based reactor prepared in situ using carbon nitride. This novel hybridization seamlessly integrates polymer science advancements with the classical virtues of heterogeneous catalysts. The catalytic composite was synthesized by employing polypentadecalactone (PPDL) and nanostructured carbon nitride as immiscible phases. We have elucidated the intricate material structure and its physico-chemical properties. Remarkably, our reactor construct exhibits remarkable capabilities, as exemplified by its application for methylene blue photodegradation under flow conditions. Furthermore, the system potential was vividly demonstrated across diverse photocatalytic reactions.

6.2. Experimental

Catalyst Synthesis. The metal-based catalysts were prepared via copolymerization. An aqueous solution of corresponding chlorinated salt (10 mmol; Sigma-Aldrich, 99%) in water (10 mL) and of sodium tricyanomethanide (10 mmol; Sigma-Aldrich, 99%), in water (10 mL), were stirred at room temperature (3 h). The resulting mixture was filtered to recover the solid metal tricyanomethanide, washed with water (30 mL), and dried in vacuum. The salt (37

mg, 0.015 mmol) was added to a 40% aqueous dispersion of 12 nm SiO_2 particles (7.5 g, Ludox HS40; Sigma-Aldrich) and solid cyanamide (70 mmol; Sigma Aldrich, 99%), and stirred at 70 °C (16 h). The obtained white solid was then heated at 550 °C (4 h, heating ramp: 2.2 °C min^{-1}). The resulting yellow solid was washed with a NH_4HF_2 solution (12 g in 50 mL of water; Sigma-Aldrich, 95%), at room temperature (24 h) and filtered, affording the product after drying under vacuum.

Bijel Preparation. To a mixture of pentadecalactone (PDL) (7 mmol, 1 equiv.; Sigma-Aldrich, 99%) and ethanol (1.4 mmol, 0.2 equiv.; Sigma-Aldrich, 99%), triazabicyclodecene (TBD) (0.28 mmol, 0.04 equiv.; Sigma-Aldrich, 99%) was added. The solution was mixed at 80 °C for 1.5 h to reach the desired degree of polymerization. Then, 60 mg of photocatalyst were dispersed in 3 mL of deionized water (20 mg mL^{-1}) at room temperature. The mixture was sonicated using an ultrasonic probe (Fisherbrand™ 120) at 30 W for 15 min, to obtain a homogeneous dispersion, added to the polymeric mixture, and stirred at 90 °C until completion of the biphasic porous structure formation. Finally, the obtained polymer was dried under vacuum at 60 °C for 5 h to obtain the photocatalytic material.

Photocatalytic Experiments. All substrates were purchased by Sigma-Aldrich and used without any further purification. Product characterization was performed using several techniques, depending on the reaction. Absorption spectroscopy was performed using a Thermo Scientific GENESYS™ Vis/UV-Vis spectrophotometer at 664 nm. High-performance liquid chromatography (HPLC) was conducted with the Agilent™ 1260 Infinity II system, equipped with a variable wavelength detector G7114A working at λ = 210 nm, and a C18 HypersilGOLD 5 μm 175 Å column (Thermo-Fisher). Samples were analyzed using $MeCN/H_2O$ 60:40 as a mobile phase with a total flow rate of 0.7 mL min^{-1} at 40 °C. ^1H NMR spectra were recorded on a Bruker 400 MHz spectrometer. Chemical shifts are reported in parts per million downfield from tetramethylsilane.

Preparation of photocatalytic reactor. 500 mg of photocatalytic material, containing 20 mg of photocatalytic material, were prepared following the previously reported procedure and melted at 90 °C. The obtained liquid mixture

was loaded into a transparent fluorinated ethylene-propylene (FEP) tube (25 mm long, 3.2 mm o.d., and 2.1 mm i.d.), plugged with a quartz wool filter and connected via 1/8" o.d. 1/4"-28 flat bottom flangeless fittings to a 1/16 o.d. PTFE tube. The reactor volume was calculated using the difference in mass between the dry photoreactor and the mass of the filled reactor washed the reaction solvent, dividing the difference by the solvent density. The reagent solution was pumped into the prepared reactor using a syringe pump (Harvard PHD ULTRA™), equipped with a 25 mL gastight syringe (Hamilton™), and irradiated at different light wavelengths using a commercial PhotoCube™ (ThalesNano) apparatus (128 W).

General Procedure A: Photodegradation of methylene blue (MB)

MB was dissolved in deionized water to reach the desired final concentration. 20 mL of solution were pumped into the photocatalytic reactor under 457 nm LED irradiation at 43 °C, using different flow rates. 2 mL of solution were collected and analyzed by absorption spectroscopy.

General Procedure B: Photooxidation of benzyl alcohol (BnOH)

BnOH (0.19 mmols) was dissolved in deionized water (5 mL) and pumped in the photocatalytic reactor under 457 nm LED irradiation at 38 °C, using a flow rate of 0.006 mL min^{-1}. A volume of 0.3 mL of solution was withdrawn, diluted with 1.5 mL of pure acetonitrile, and analyzed by HPLC. ^{1}H NMR was performed to characterize the final product.

General Procedure C: Photocatalytic amination

4-Bromobenzonitrile (0.16 mmols, 1 equiv.) was added to a solution containing sodium azide (0.8 mmols, 5 equiv.) and triethylamine (0.32 mmols, 2 equiv.), dispersed in a mixture EtOH/H$_2$O 1:1 (2 mL). The reaction solution was purged with N$_2$ for 10 min and pumped into the tubular system under white-LED irradiation at 35 °C, using a flow rate of 0.003 mL min^{-1}. The collected solution was diluted with water (3 mL) and extracted with ethyl acetate (5 mL x 2). The combined organic layers were dried over sodium sulfate, filtrated, and concentrated under vacuum. ^{1}H NMR was performed to characterize the final product.

General Procedure D: Photocatalyzed C-N homocoupling

Benzylamine (0.08 mmols) was dissolved in a mixture MeCN/H_2O 1:1 (2 mL). The reaction solution was pumped into the photocatalytic reactor under 457 nm LED irradiation at 38 °C, using a flow rate of 0.003 mL min^{-1}. The collected solution was diluted with water (3 mL) and extracted with ethyl acetate (5 mL x 2). The combined organic layers were dried over sodium sulfate, filtrated, and concentrated under vacuum. ^1H NMR was performed to characterize the final product.

Characterization techniques. Porosity, pore distribution, and surface area were deduced via nitrogen physisorption measurements, degassing the sample (150 °C, 20 h) using a Micromeritics 3Flex porosimeter. The size distribution of pores was evaluated using the quenched solid density functional theory model for nitrogen adsorbed on carbon, assuming pores with a cylindrical shape. The Brunauer–Emmett–Teller (BET) model to adsorption isotherms for $0.05 < p/p_0 < 0.3$ was used to calculate specific surface area with QuadraWin 5.05. The material crystallinity was evaluated through X-ray powder diffraction (XRD) studies, using Philips model PW3040/60 as X-ray diffractometer and Cu Kα radiation with $\lambda = 0.15418$ nm. The oxidation state of both the metal atoms and the support in the fabricated catalyst was determined by X-ray photoelectron spectroscopy (XPS) with a Physical Electronics Instruments Quantum 2000 spectrometer, using an electron beam (at 15 kV and 32.3 W) to generate a monochromatic Al Kα radiation. CHNS elemental analysis was performed using a Vario Micro device, after combustion. The inductively coupled plasma optical emission spectroscopy (ICP-OES) analysis was conducted in a HORIBA Ultra 2, using a photomultiplier tube detector. Dynamic light scattering (DLS) measurements were conducted using a Malvern Zetasizer Nano ZS (scattering angle=173°) at 25 °C, after an equilibration time of 60 seconds. Solid state cross polarization/magic angle spinning nuclear magnetic resonance (CP-MAS NMR) was used to acquire ^{13}C and ^{15}N NMR spectra on a Bruker NEO 500 MHz spectrometer equipped with a commercial 4 mm MAS iProbe to provide a more complete characterization of the polymeric material. Samples were packed into 4 mm ZrO_2 rotor and spun at the magic angle. Infrared spectra were collected with a Nicolet^{TM} iS20 spectrometer

using the corresponding Smart iTX setup for ATR measurements; 128 scans recorded with a 2 cm^{-1} resolution were typically averaged for each of the acquired spectra. Scanning electron microscopy (SEM) and SEM-EDS analysis were performed by a Philips XL30 instrument in low vacuum mode -0.8 torr. SEM is equipped with a EDAX Element probe for elemental mapping and analysis. Samples were fixed onto a standard SEM pin with carbon tape and analyzed without further treatment. Confocal laser scanning microscopy measurements were performed on a custom-built confocal setup. For the excitation 405/488 nm 40 MHz pulsed diode lasers (PDL 800-B driver with LDH-D-C-405/LDH-P-C-485B diodes, PicoQuant) were utilised. A quarter-wave-plate was used in the excitation path to convert linear to circular polarisation. The laser beam was coupled into a single-mode fiber (PMC-460Si-3.0-NA012-3APC-150-P, Schäfter + Kirchhoff) with a fiber-coupler (60SMS-1-4-RGBV-11-47, Schäfter + Kirchhoff). After the fiber, the output beam was collimated by an air objective (UPlanSApo 10× /0.40 NA, Olympus). After passing thought a corresponding clean-up filter (MaxDiode 405/10, Semrock or ZET 488/10, Chroma), an ultra-flat quad-band dichroic mirror (ZT405/488/561/640rpc, Chroma) was used to direct the excitation light into the microscope. The excitation beam was directed into a laser scanning system (FLIMbee, PicoQuant) and then into a custom side port of the microscope (IX73, Olympus). The three galvo mirrors in the scanning system are deflecting the beam while preserving the beam position in the backfocal plane of the objective (UPIanSApo 60× /1.2 NA water, Olympus). The sample position can be adjusted a using manual XY stage (Olympus) and a z-piezo stage (Nano-ZL100, MadCityLabs). Emission fluorescence light was collected by the same objective and de-scanned in the scanning system. Afterwards, the achromatic lens (TTL180-A, Thorlabs) was used to focus the beam onto the pinhole (100 µm P100S, Thorlabs). The excitation laser light was blocked in the emission path by a band-pass filter (BrightLine HC 460/60, Semrock) or by a long-pass filter (561 LP Edge Basic, Semrock). Then, the emission light was collimated by a 100 mm lens. Finally, the emission light was focused onto a SPAD-detector (SPCM-AQRH, Excelitas) with an achromatic lens (AC254-030-A-ML, Thorlabs). The output signal of the photon detector was recorded by a TCSPC system (HydraHarp

400, PicoQuant) which was synchronized with the triggering signal from the excitation laser. Measurements were acquired with the software (SymPhoTime 64, PicoQuant), which controlled both the TCSPC system and the scanner system. Typically, sample scan with a virtual pixel size of 100 nm, a dwell time of 2.5 µs/pixel and a TCSPC time resolution of 16 ps were chosen. The polymer sample was labeled with Nile Red dye according to the following procedure. First, a small piece of the material was cut with a sharp scalpel and immersed in a 1 µM solution of Nile Red (in distilled water) for 30 minutes. Then, the corresponding piece of the material was transferred to the microscope and placed between two coverslips in the water medium. During the measurements, the beam was focused approximately 10 µm inside the material. Nano computed tomography scanning was performed by using an industrial micro CT system (BIR Actis 130/150, upgraded). Scanning plane is horizontal and perpendicular to the axis of the cylindrical sample. Based on geometry and dimensions of the specimen, a cubic voxel of 0.012 mm was obtained. Segmentation and binarization of 2D slices obtained from microCT technique was carried out by means of Avizo (Mercury)® software in order to detect pores. The thermal stability of the synthesized bijels was evaluated by thermogravimetic analysis (TGA) using a simultaneous thermal analyzer (STA) 6000 (PerkinElmer). Absorbance was measured by Thermo Scientific GENESYS™ Vis/UV-Vis spectrophotometer. The ^{1}H HR-MAS spectra were recorded using a Bruker NEO spectrometer operating at 500 MHz proton frequency, equipped with a dual ^{1}H/^{13}C high-resolution magic angle spinning (HR-MAS) probehead. The samples were transferred in a 4 mm ZrO_2 rotor containing a volume of about 12 µL. All data were acquired at 305 K with a spinning rate of 4 kHz. The diffusion measurements were performed using diffusion ordered spectroscopy (DOSY) methods with a bipolar pulse longitudinal eddy current delay (BPPLED) pulse sequence.[275] The duration of the magnetic-field pulse gradients (δ) and the diffusion times (t_d) were optimized for each sample to obtain complete dephasing of the signals with the maximum gradient strength. For the investigated samples, t=20 ms and δ=3 ms. The pulse gradients were increased linearly from 2 to 95% of the maximum gradient strength. In each

experiment, a series of 32 spectra with 32K points was collected with a relaxation delay of 10 s. The DOSY experiment was repeated in triplicate.

6.3.   Results and Discussion

The powdered graphitic and mesoporous carbon nitride (gCN_x and $mpgCN_x$, respectively) samples, and the materials featuring atomically-dispersed transition metals on mesoporous carbon nitride ($Mn@mpgCN_x$, $Zn@mpgCN_x$, and $Ni@mpgCN_x$) were synthesized as detailed in Appendix A, and the obtained material chemical and structural characteristics (Table A.6.1) were in accordance with previous results.[183,276] The powdered photocatalysts were used to prepare *in situ* a polymeric microphotoreactors with functionalized (photo)catalysts. Here, ω-pentadecalactone (PDL) underwent thermal-induced ring-opening polymerization, generating the hydrophobic phase of the Pickering emulsion. The aqueous phase was obtained by suspending the carbon nitride powders in water, with a 1:1 volume ratio compared to the polymer. The phases combination, resulting from the entrapment of water in the polymeric network, in the absence of coalescence phenomena, generated a bicontinuous nanoarchitecture (Figure 6.1 a). In the experimental campaign, we prepared, characterized, and evaluated a series of polymeric functionalized microphotoreactors with the powders indicated above, but for the sake of conciseness only the microphotoreactor containing $mpgCN_x$ is discussed below in terms of advanced materials characterization.

The microphotoreactor obtained following the aforementioned procedure was characterized by solid state cross polarization magic angle spinning nuclear magnetic resonance spectroscopy (ssCP-MAS NMR). The analysis was performed in comparison with the spectrum of the powdered $mpgCN_x$ and the pure polypentadecalactone (PPDL) used as skeleton for the microphotoreactor, confirming the nature of the obtained bicontinuous phase (Figure 6.1 b). In particular, the ^{13}C ssCP-MAS spectrum of $mpgCN_x$ showed two sharp signals localized at 156.7 and 164.5 ppm, in agreement with data reported in the literature.[277] Instead, the spectrum of PPDL featured a plethora of signals localized in three main regions, corresponding to methylene groups (20 and 40 ppm), α-methoxy carbons (60 and 70 ppm), and carbonyl moiety (169 and 177 ppm).[278]

Finally, the solid-state ^{13}C NMR spectrum of the prepared microphotoreactor showed characteristic signals of both the polymer and the photocatalyst, thus confirming the presence of both the components in the obtained structure. The zoomed region (180-140 ppm) has been included in Appendix A (Figure A.6.2 a) to highlight the two signals related to the presence of carbon nitride within the composite. Obviously, the low intensity of the carbon nitride signal was justified by the substantial presence of a transparent polymeric phase within the microphotoreactors, wherein the catalyst found its confinement. Fourier-transform infrared (FTIR) spectroscopy of mpgCN$_x$, PPDL, and the functionalized microphotoreactor biphasic porous structure are shown in Figure 6.1 c. The mpgCN$_x$ spectrum (in blue) showed a broad absorption band between 1700 and 1150 cm^{-1}, corresponding to the stretching modes of the heteroaromatic rings, and a sharp characteristic peak at 810 cm^{-1}, attributed to the breathing mode of triazine units.[279] PPDL (in red) and the functionalized microphotoreactor (in black) featured an absorption band at 1730 cm^{-1}, which corresponded to the characteristic -C=O stretching vibrations of the carbonyl group. Several strong bands in the 1250-1100 cm^{-1} region were assigned to the symmetric and asymmetric C–O–C stretching vibrations. The majority of such peaks in the microphotoreactor absorption profile highlighted the confinement of the carbon nitride photocatalyst within the bicontinuous polymeric architecture. Thermogravimetric analysis (TGA) was also performed to verify the thermal stability of the prepared materials. Figure 6.1 d depicts the TGA of the microphotoreactor composite, recorded from 100 °C to 900 °C at 10 °C min^{-1}. Here, the polymer underwent irreversible pyrolysis between 350 and 550 °C, resulting from the single-step thermal degradation of C-O-C groups characterizing the polyester skeleton of the microphotoreactor. Nevertheless, the relatively high thermal stability of the microphotoreactor, up to 200-250 °C, could ensure long-term stability of the composite matrix for most fine chemical synthetic processes, and even during low-temperature light irradiation. The UVvis absorption spectra of mpgCN$_x$, PPDL, and the microphotoreactor are then shown in Figure 6.1 e.
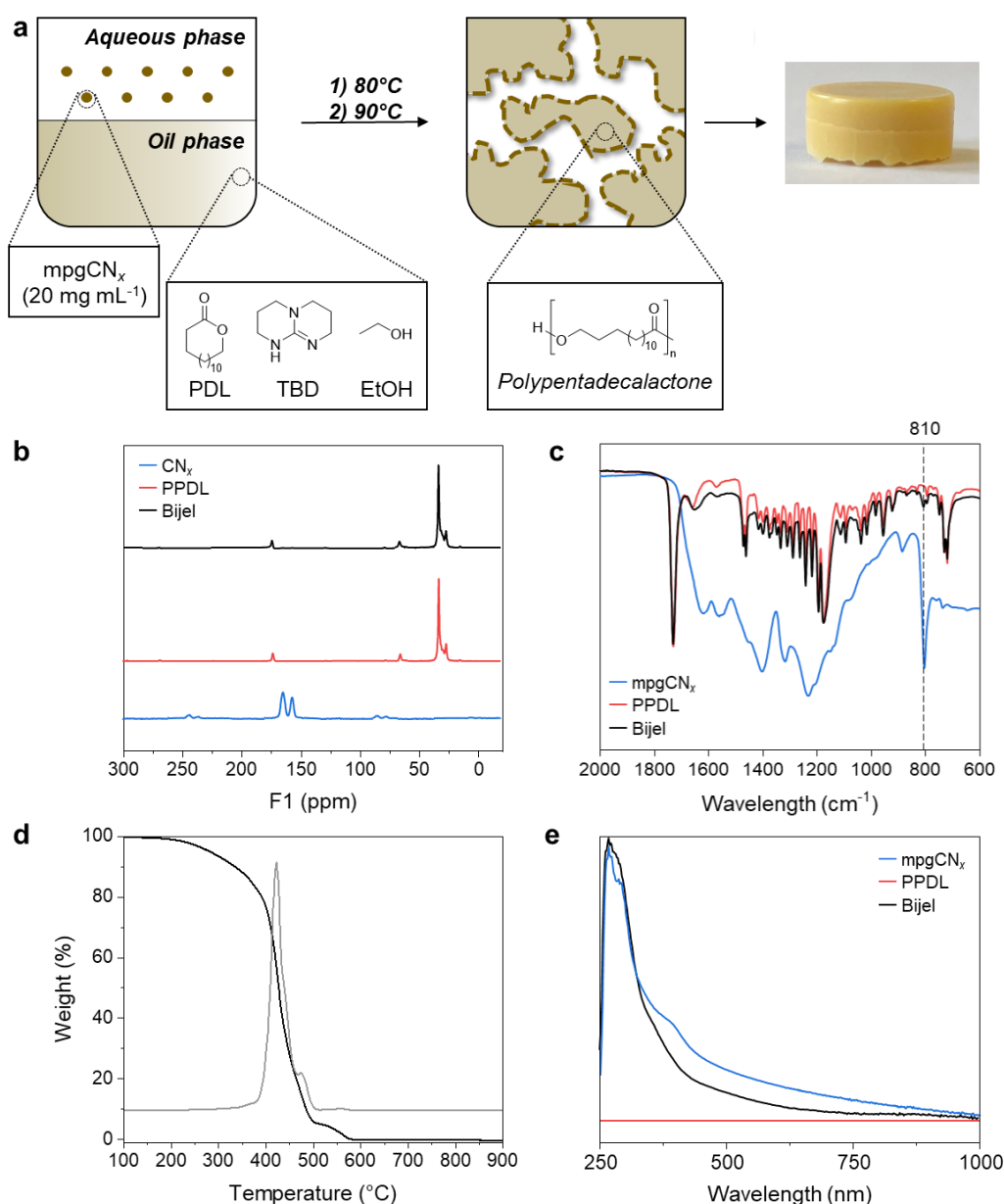
Figure 6.1. *Integrated materials analysis of a microphotoreactor confining mpgCN$_x$ and of reference powdered samples. Schematic representation of the microphotoreactor preparation process (a), along with ^{13}C solid-state cross-polarization magic-angle-spinning nuclear magnetic resonance spectroscopy (b), Fourier-transform infrared spectroscopy (c), thermogravimetric analysis (solid line) and corresponding weight derivative (dotted line) (d), and UV-Vis absorption spectra (e) of selected materials. Specifically, the figure showcases properties of mpgCN$_x$ (in blue), PPDL (in red), and of the microphotoreactor confining mpgCN$_x$ (in black).*

The similar absorption profile of both the powdered catalyst and the microphotoreactor demonstrated the efficient $mpgCN_x$ incorporation in the biphasic porous structure, with retention of its photon absorption capacity, while the transparency of PPDL, unable to absorb photons above 200 nm, demonstrated its potential inactive behavior in any photocatalytic process.

Scanning electron microscopy (SEM) of the biphasic porous microphotoreactor and the respective elemental maps obtained through energy dispersive X-ray spectroscopy (EDS) are shown in Figure 6.2 b and c. The presence of spherical structured aggregates with a diameter of 10 μm (inset Figure 6.2 b) was attributed to the $mpgCN_x$ phase, in line with the confocal laser scanning microscopy (CLSM) observations (*vide infra*). EDS confirmed the incorporation of carbon nitride in the polymeric matrix and its uniform distribution. The microreactor systems showed a strong fiber-like, porous morphology diffused homogenously through the material (Figure 6.2 d). For the investigation of the internal structure of the material, the polymer was labelled with Nile Red dye (for the detailed labelling procedure, refer to Appendix A) and submitted for CLSM analysis. Nile Red is widely used for visualizing various polymer structures due to its photophysical and spectroscopic properties.[270] Specifically, it is nearly nonfluorescent in water or other polar environments but undergoes fluorescence enhancement when non-covalently attached to the polymer structure of interest. In our case, we observed and confirmed the fiber-like polymeric porous structure of the microphotoreactor, and the aggregates of $mpgCN_x$ nanoparticles because their emission band was significantly blue shifted compared to Nile Red. Thus, by utilizing a 405 nm excitation wavelength, we selectively imaged the morphology of the incorporated $mpgCN_x$ nanoparticles while the polymer matrix remained unobserved. Here, the presence of spherical structured aggregates with a diameter of 10 μm (inset Figure 6.2 b and Figure 6.2 d) was attributed to $mpgCN_x$ nanoparticles. To confirm our observations, we finally performed control CLSM experiments, imaging non-labeled $mpgCN_x$ -doped material and pure PPDL polymer.
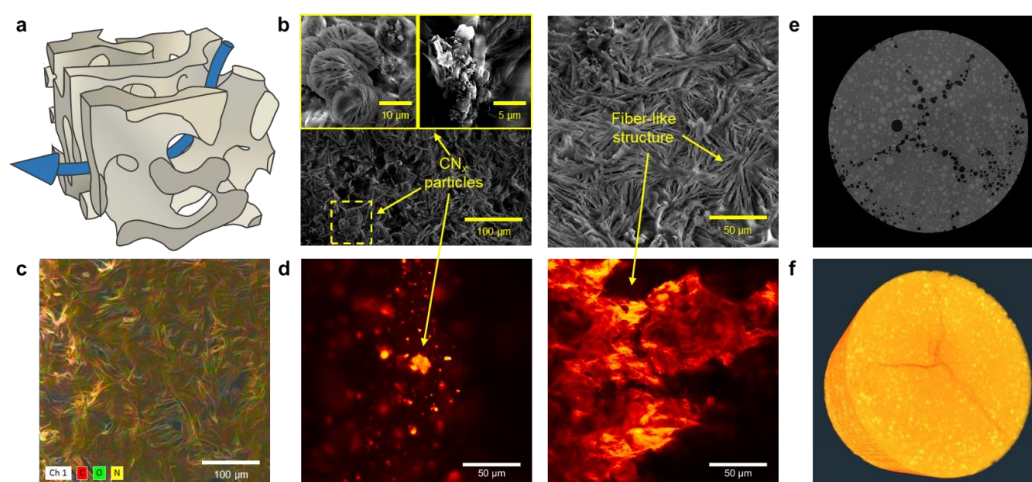
Figure 6.2. *Advanced visual inspection of the microphotoreactor confining mpgCN$_x$. 3D representation showcasing the porous structure of the composite (a); scanning electron microscopy capturing the cross-sectional view of the sample (b), along with the corresponding energy-dispersive X-ray spectroscopy image (c). Confocal laser scanning microscopy (d) revealing mpgCN$_x$ confined within the microreactor porous structure. Front view of the bijel-based microphotoreactor by tomography (e), where the dark areas represent the free volume available for the catalysis, and a 3D reconstruction of the whole microphotoreactor predicted via tomographic technique (f).*

The internal morphology of the material was investigated through microcomputed tomography (microCT, Figure 6.2 e). The spherical shape and the homogeneous distribution of the pores, with a modal diameter of 0.20 mm, featured the whole volume of the prepared material, with an average pore diameter of 527.0 Å detected by porosimetry test (Appendix A, Figure A.6.3). The pores were mainly concentrated along a central vertical axis originating from a larger pore at the base of the sample and presenting three branches pointing to the outer edge of the specimen with an angle of 120° (Figure 6.2 f). Rounded vesicles of the same dimensions of the pores and filled by a denser material (light grey, Figure 6.2 be) were widespread throughout the sample. Also, the presence of some isolated pores at the border of the sample was detected during the microCT analysis. The 3D reconstruction enabled by this technique, provided a complete microstructural representation of the main features of the bijel, including tight

distributions of domain sizes, high connectivity between channels, controlled tortuosity, and structural self-similarity (Figure 6.2 f). Given the high porosity of the sample, we attempted to measure the diffusivity of potential reactive molecules passing through the microphotoreactor. In particular, in order to measure the molecular diffusion motion over a known observation time t_d, ^{1}H high resolution magic angle spinning (HR-MAS NMR) of the microreactor samples were recorded using diffusion ordered spectroscopy (DOSY) NMR technique with pulse field gradients (PFG) of increasing intensity along a defined axis (usually, z-axis). A conventional analysis of the 2D experiment yielded a 2D map encoding for each observed species, with the chemical shift in the horizontal axis versus their diffusion coefficient, D, in the vertical dimension.[280] Figure 6.3 a shows the ^{1}H DOSY map. The data confirm the bicontinuous structure of the material with two separate domains (water-PCL highlighted in the map). Following a different processing of the experimental data, the molecular mean square displacement $\langle z^2(t_d) \rangle$ could be calculated by fitting the gradient dependent signal intensities $I(q, t_d)$ according to the following equation:

$$I(q, t_d) = I_0 \exp\left(-\frac{1}{2} q^2 \langle z^2(t_d) \rangle\right) \tag{Eq. 1}$$

where $q = \frac{\gamma g \delta}{2\pi}$, and in particular γ is the gyromagnetic ratio of the observed nucleus, δ is the gradient pulse duration, and g is the intensity. For isotropic solutions, the mean square displacement scales linearly with the observation time t_d according to the equation:

$$\langle z^2(t_d) \rangle = 2D t_d \tag{Eq. 2}$$

where D is the diffusion coefficient. The normalized experimental signal decays, $I(q, t_d)/I(0, t_d)$, versus q^2 is reported in Figure 6.3 b and c. The diffusion coefficient within the bijel structure was $D = 4.4 \times 10^{-10}$ m^2 s^{-1}, a lower value than the bulk water solution $D_0 = 2.7 \times 10^{-9}$ m^2 s^{-1}, indicating the presence of tortuous interconnected domains.[281] The ratio of D over D_0 ($\tau = 0.16$) reflected the tortuosity of the diffusion motion through a microphotoreactor structure.
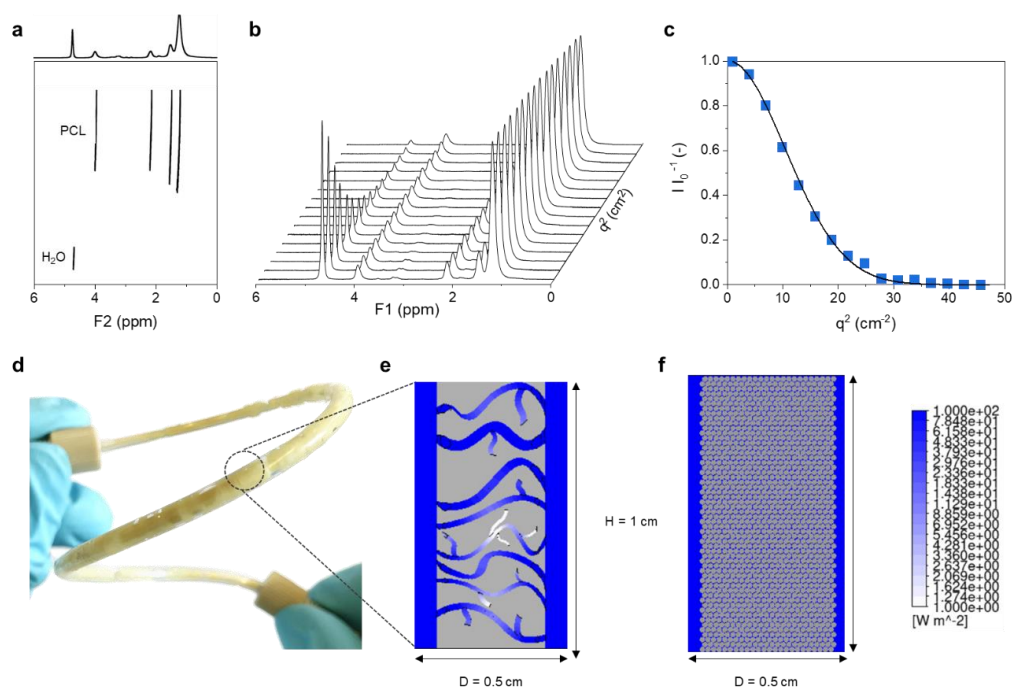
Figure 6.3. *Diffusivity and proof of light penetration within the microphotoreactor structure. Mapping through high-resolution ^{1}H magic angle spinning diffusion-ordered spectroscopy of the microphotoreactor composite (a), with the decay of the NMR signal intensity illustrated in (b) and (c). Additionally, a visual of the microphotoreactor packed in a polymer tube and used for catalytic applications (d). Light distribution within the photocatalytic microphotoreactor via computational fluid dynamics (e), and analogous distribution within a packed-bed reactor (f).*

The catalytic properties of the microphotoreactor were investigated on several light-driven reactions under flow conditions. The fabricated materials, loaded with several types of gCN$_x$ and mpgCN$_x$, were packed in a transparent fluorinated ethylene propylene copolymer tube (Figure 6.3 d, for more details see the Appendix A), and firstly tested on the visible-light driven degradation of methylene blue (MB). The selected model reaction was performed using a 44 μM aqueous solution of the dye, based on the preliminary concentration screening (Table A.6.2, Entry 1). Also, we examined our reaction in the absence of catalyst, as shown in Table A.6.2, Entry 2, and no reaction was observed. Only when the reaction was performed in the presence of mpgCN$_x$ irradiated under blue light
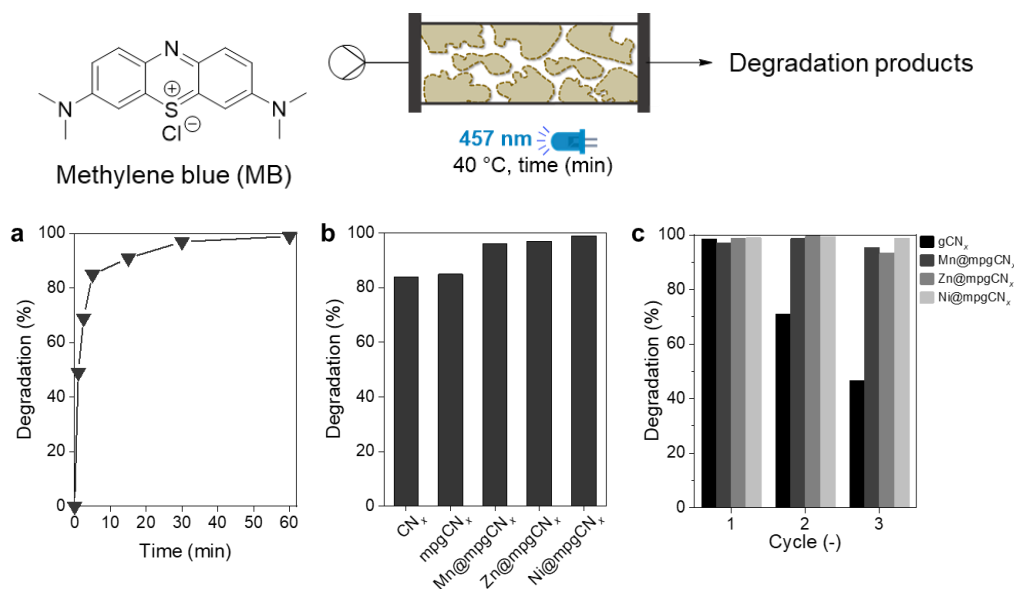
Figure 6.4. Photocatalytic degradation of MB. Effect of residence time on the MB degradation rate using a microphotoreactor confining mpgC$_3$N$_4$ (a), evaluation of the photocatalytic activity of several microphotoreactor confining several metal-free and metal-based materials (b), and investigation of the microphotoreactor stability over three reaction cycles (c). Reaction conditions: MB concentration = 44 μM, τ = 5 min, λ = 457 nm, T = 40 °C, and water as solvent.

conditions, the degradation was completed within 5 min (Table A.6.2, Entry 3). To optimize the reaction conditions in a continuous-flow mode, we investigated the degradation of MB at different residence times (Figure 6.4 a). Between 5 and 15 min, a quasi-linear increase of the process efficiency was observed (from 49% to 85%), followed by a plateau, with a final degradation of MB of 99% with 60 min residence time. Comparative data between metal-free and metal-based mpgCN$_x$ are shown in Figure 6.4 b, with a 5 min residence time to better appreciate the differences between the screened photocatalytic systems. The two metal-free photocatalysts, namely gCN$_x$ and mpgCN$_x$, bearing a different surface area (Table A.6.1 in Appendix A), showed similar photocatalytic degradations at fixed conditions. In contrast, the use of metal-based mpgCN$_x$ lead to better degradation rates, with no relevant differences based on the metal type (*i.e.*, Mn, Zn, and Ni). The stability of the prepared photocatalytic materials was also evaluated performing the continuous-flow reaction over three reaction cycles, with an

excellent photostability and recyclability of the produced biphasic porous structure and no activity losses when mpgCN$_x$-based materials were used (Figure 6.4 c). In contrast, the use of the gCN$_x$ led to a decrease in the MB degradation rate due to the partial deactivation of the used photocatalyst.

Computational fluid dynamics (CFD) simulations were performed to study the radiation field inside the reactor. The simulation results are shown in in Figure 6.4 e and f (and also in Figure A.6.4 in Appendix A), with the light distribution shown in blue as the light was assumed to be in the blue visible spectrum, to replicate the conditions of experiments. In these conditions, we considered as negligible the optical thickness (defined as $(k + \sigma_s) \cdot L_s$, where k and σ_s are the absorption and scattering coefficient of the species, respectively, and L_S is the optical path of the reactor.[282] The results corroborate that the open and porous structure of the microphotoreactor, bearing the assembly of a sponge, allows the light to enter the channels; this ensures higher irradiation in the reactor than conventional systems such as packed bed reactors, in which the layers of catalyst spheres can considerably hinder light penetration.[282]

The scope of this work was finally expanded to include industrially-relevant synthetic processes, and proving the different potential applications of our photocatalytic system. The reaction, in particular, were conducted without any optimization of the reaction conditions (Scheme 6.1). Notably, the porous microphotoreactor structure, loaded with photoactive single-atom catalysts based on mpgCN$_x$, provided the desired products in good yields. The photooxidation of benzyl alcohol gave in one pass the desired benzaldehyde with a 27% yield after 1 h, using air as oxidizing agent and water as solvent (Scheme 6.1 a). The photocatalytic amination of aryl bromides was performed in presence of sodium azide and triethylamine, with the corresponding p-aminobenzonitrile (24%) in presence of white light irradiation (Scheme 6.1 b). A 30% yield of product was obtained when the microphotoreactor was used in the C-N homocoupling of benzylamine (Scheme 6.1 c).
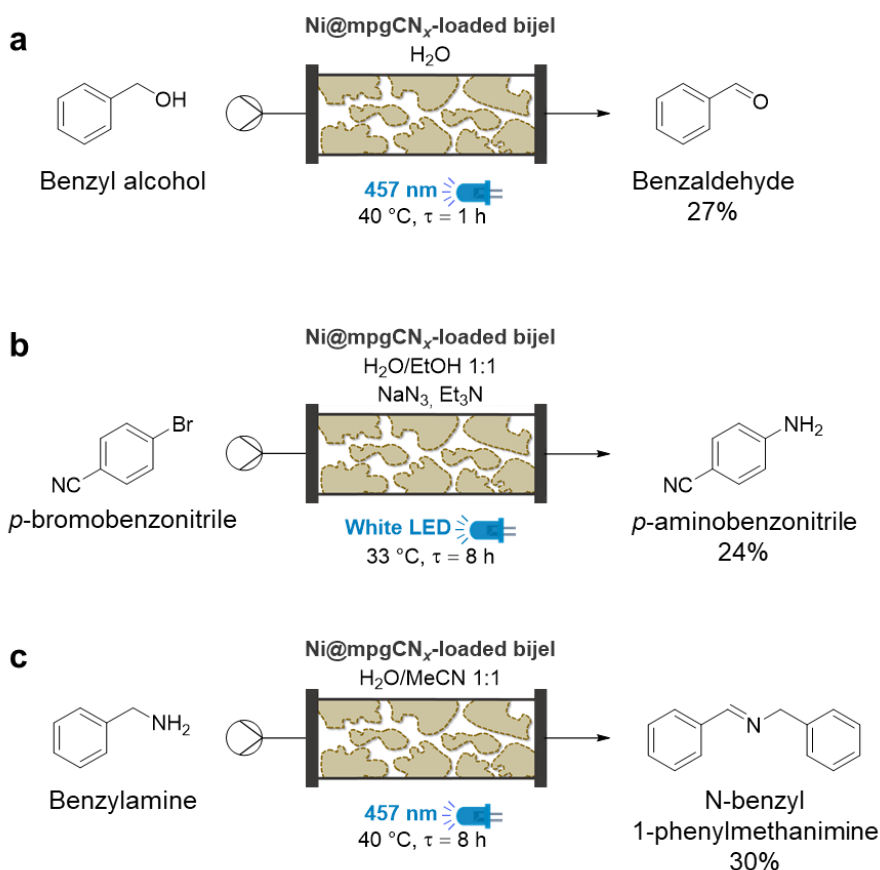
Scheme 6.1. *Photocatalytic scope. Photooxidation of benzyl alcohol (a), photocatalytic amination of p-bromobenzonitrile (b), and photocatalyzed C-N homocoupling (c) over a microphotoreactor confining metal-based materials.*

6.4. Conclusions

In this study, we successfully developed a novel paradigm for heterogeneous photocatalysis by confining powdered photocatalysis into a gel-based microreactor. This innovative approach combines polymer science with classical heterogeneous catalysis. The resulting catalytic composite, synthesized in situ with polypentadecalactone and nanostructured carbon nitride, displayed a distinctive bicontinuous porous nanoarchitecture. Our microphotoreactor exhibited remarkable capabilities, exemplified by its effective performance in methylene blue photodegradation under flow conditions. Furthermore, the system demonstrated potential across diverse reactions. This research opens new avenues

for multifunctional catalysis, leveraging the benefits of both polymer matrices and solid-state catalysis for sustainable chemical transformations.

Chapter 7

Enhanced flow synthesis by in-line integration of catalysis and continuous chromatography

Sivo, A.; Kim, T. K.; Ruta, V.; Luisi, R.; O.-Tejada, J.; E.-Gelonch, M.; Hessel, V.; Sponchioni, M.; Vilé, G. *React. Chem. Eng.* **2022**, *7* (12), 2650–2658.

7.1. Introduction

Automatized and smart pharmaceutical processes are necessary to realize iterative design–synthesis–testing platforms that can provide chemical probes and leads for druggable targets.[283,284] Over the past decades, microreactor technology has offered a way to perform chemical reactions with milder, faster, and safer protocols.[285,286] This has been ascribed to the high surface-to-volume ratio of those small-scale reactors, that lead to improved mass and heat transfer.[261] The integration of microreactors with in-line process analytical systems and artificial intelligence algorithms has further developed the field, enabling quicker optimization protocols, with several advantages for pharmaceutical and chemical

manufacturing.[155,287,288] As these benchtop reactors become even more indispensable as a result of their modularity, it is of paramount importance to be able to connect upstream and downstream methods to realize an integrated process. One of the most challenging (and less developed) aspects of microsystem engineering remains the design and in-line integration of benchtop purification processes, which are always needed after a synthetic step. Most chemical processes involve multistep reactions, and almost each step needs a downstream purification, that can go from the easy workup to a demanding crystallization and chromatography.[94,159] These downstream steps consume energy, reactants, solvents, and time, with a considerable impact on the environmental footprint and overall efficiency of the process. Despite the high number of downstream unit operations, there are only a few devices which have been suitably designed for integration with microreactors.[20,23] These examples mainly relate to liquid–liquid and liquid–gas extractions used for solvent switch, which are based on Zaiput membranes.[289,290] Technologies such as continuous benchtop crystallizations have not yet provided a method for easy and in-line integration with continuous-flow reactors.[291,292]

Significant efforts to integrate in-line purification by column chromatography with continuous-flow synthesis have been undertaken in recent years. The first method has been developed by Seeberger and co-workers, by coupling simulated moving-bed (SMB) chromatography with flow synthesis.[293] Here, a highly complex system has been used, consisting of a six-column configuration and 48-port valves. The use of multiple dual-mode centrifugal partition chromatography (MDM-CPC) has been also reported.[294] This kind of chromatography relies on the use of two non-miscible phases, instead of using a solid stationary phase. Selecting the two phases, or biphasic liquid system (BLS), is elaborate and time-consuming for benchtop application, as it needs to consider various operating parameters, such as the partition coefficients of product in the BLS and the settling time of the phases, which can determine the resolution of the separation. Two studies have been reported based on the use of multiple columns in parallel as a substitute of the countercurrent chromatography for the in-line purification. A supercritical fluid chromatography (SCFC) coupled with a multistep flow synthetic process has

been reported by Ley and co-workers.[295] Despite the high overall yield of the process, this four-column system of 21 independent items of equipment with additional programming for automatic sampling require many specialists to operate. Vilela and co-workers investigated the use of in-line flash chromatography purification through a two-column configuration with a 10-port valve.[296] All in-line purification technologies mentioned before provided significant advancements to this field, but their system complexity and low injection volumes per cycle (maximum 10 mL) clearly require further improvements.

In this work, we propose the capture-SMB technology as a new in-line purification approach, that offers high resolution, yield, and productivity, as well as low solvent consumption.[297] This is achieved by utilizing only two twin columns and a new loading method, in which the product breaking through the outlet of a fully loaded first column is loaded onto the second column, thereby avoiding wasting precious material as well as increasing the process productivity.
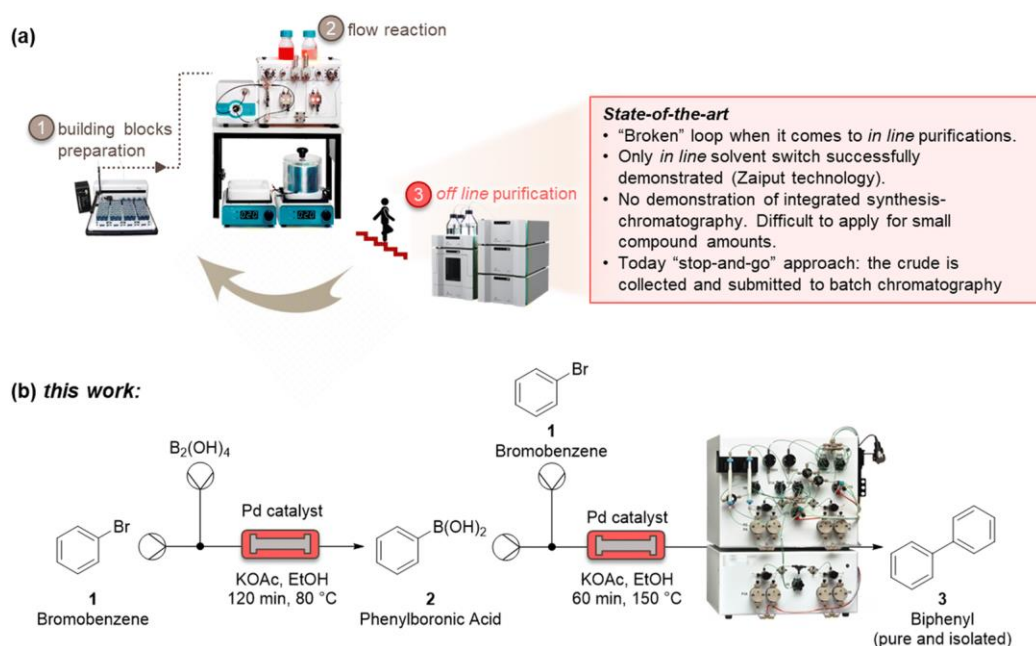

Figure 7.1. *State-of-the-art showing challenges in terms of in-line integration of continuous purification systems with flow platforms (a). Sketch for the integrated and continuous synthesis–purification process reported in this work, for the example of a Suzuki–Miyaura cross coupling reaction (b).*

To integrate synthesis and purification, and build the end-to-end continuous process, a surge tank can be introduced to compensate the different flowrates of the synthesis and purification steps.[298,299] As the mass transfer is improved between the liquid and the resin by the realization of a countercurrent movement between the stationary phase and the mobile phase, a higher resolution, or higher purity, is expected by the application of this technology. Moreover, a built-in software of the capture-SMB technology allows for fully automated operation and the minimum number of multi-port valves minimize the hold-up volume.

7.2. Experimental

General information. All reactants were purchased from Sigma-Aldrich and used as such. Product characterization after reaction was done collecting an aliquot of the reaction product and analyzing it by high-performance liquid chromatography (HPLC). This was carried out on an Agilent 1100 series chromatograph equipped with a Thermo Scientific C18 Hypersil GOLD™ column (4.2 mL) and diode array detector (DAD) set at $\lambda = 210$ nm. In addition, ^{1}H and ^{13}C nuclear magnetic resonance (NMR) spectra of the products were recorded on a Bruker 400 mHz spectrometer. Batch reactions were performed using 20 mL round-bottom flasks. Flow reactions were conducted on a commercial Uniqsis™ flow microreactor, consisting of an HPLC pump, a T-shaped micromixer, a packed-bed reactor (diameter 1 cm, length 12 cm), a heating module, and a back-pressure regulator of 10 bar.

Synthesis of phenylboronic acid (2). The synthesis of phenylboronic acid was performed either in a batch reactor or under continuous-flow conditions. For the batch experiments, to a stirred solution of bromobenzene **1** (1 mmol, 1 equiv.) in ethanol (5 mL, 0.2 M), dibenzylideneacetone palladium(0) phosphaadamantane ethyl silica (1% mol) and KOAc (3 mmol, 3 equiv.) were added at room temperature. After stirring the mixture for 5 minutes, the heating was set to 80 °C, and the $B_2(OH)_4$ (1 mmol, 1 equiv.) was added. The mixture was kept under stirring for another 2 h. After this step, the mixture was cooled down to room temperature, and an aliquot of the reaction mixture was withdrawn for HPLC

analysis. For the flow experiments, a solution of bromobenzene **1** (1 mmol, 1 equiv.), $B_2(OH)_4$ (1 mmol, 1 equiv.), and KOAc (3 mmol, 3 equiv.) in ethanol (5 mL) was pumped on the commercial Uniqsis™ flow microreactor. The solution passed through a column reactor, packed with dibenzylideneacetone palladium(0) phosphaadamantane ethyl silica (1% mol), kept at fixed temperature. The product outlet was cooled down to room temperature, and an aliquot of the product mixture was withdrawn for HPLC analysis.

Synthesis of biphenyl (3). The synthesis of biphenyl was performed either in a batch reactor or under continuous-flow conditions. For the batch experiments, dibenzylideneacetone palladium(0) phosphaadamantane ethyl silica (1% mol) and KOAc (3 mmol, 3 equiv.) were added at room temperature to a solution of bromobenzene **1** (1 mmol, 1 equiv.) in ethanol (5 mL, 0.2 M). After stirring the mixture for 5 minutes, the heating was set to 150 °C, and phenylboronic acid **2** (1 mmol, 1 equiv.) was added to the reaction flask, and stirred for 1 h. After this step, the mixture was cooled down to room temperature, and an aliquot of the reaction mixture was withdrawn for HPLC analysis. For the flow experiments, a solution of bromobenzene **1** (1 mmol, 1 equiv.), phenylboronic acid **2** (1 mmol, 1 equiv.), and KOAc (3 mmol, 3 equiv.) in ethanol (5 mL) were pumped through a commercial Uniqsis™ flow microreactor. The solution passed through a column reactor, packed with dibenzylideneacetone palladium(0) phosphaadamantane ethyl silica (1% mol), kept at fixed temperature. The product outlet was cooled down to room temperature, and an aliquot of the product mixture was withdrawn for HPLC analysis.

Synthesis of 1,3-bis[methyl(phenyl)amino]propan-2-ol (4). A 2.8 M solution of epichlorohydrin (28 mmol, 1 equiv.) in EtOH and a 2.8 M solution of N-methylaniline (28 mmol, 1 equiv.) in EtOH were mixed and pumped through a stainless-steel coil reactor (internal volume = 60 mL) at 80 °C and 60 min. The product outlet was cooled down to room temperature, and an aliquot of the product mixture was withdrawn for HPLC analysis.

Synthesis of diphenyl ether (5). Bromobenzene **1** (0.75 mmol, 1.5 equiv.), $CuCl_2$ (1% mol), and K_2CO_3 (1 mmol, 2 equiv.) were solubilized in a round-

bottom flask using DMF (2 mL) as a solvent. The mixture was heated to 150 °C. At this temperature, phenol (0.5 mmol, 1 equiv.) was added. The mixture was kept under stirring for 24 h. After this step, the mixture was cooled down to room temperature, and an aliquot of the reaction mixture was withdrawn for HPLC analysis.

Purifications and capture-SMB technology. The purifications were conducted on a system comprising two long lifetime LED UV detectors (280 and 300 nm recorded simultaneously), and four high-precision double-piston pumps with active seal wash and one fraction collector. The system was equipped with two twin HPLC columns YMC-Triart Prep C18-S20 μm, each with a volume of 1.66 mL. The system was also supported by MControl, a dynamic software which keeps the process at the optimum. Breakthrough curves were collected using a solution composed by 25 mol% of phenylboronic acid and 75 mol% of biphenyl with a concentration of 3.5 mg mL^{-1}. Both batch chromatography and flow multi-column chromatography were performed using the same solution and a linear velocity of 300 cm h^{-1}.

The operating conditions of the capture-SMB technology were optimized using the results obtained from the breakthrough (BT) curves. As this twin-column technology uses an interconnected mode, in which the outlet of the upstream column is connected to the inlet of the downstream one, and a batch mode, in which the two columns are disconnected and operate in parallel, timings to switch from the batch to the interconnected mode and vice versa are essential in optimizing the operation of the technology. This process optimization can be easily achieved by inserting the BT points of the product (ranging from 1% to 10% of the product BT), and the desired loading volume (ranging from 65% to 85% of the product BT) obtained from the BT curves. These two experimental points determine the start and the end of the interconnected mode, respectively. After the first step of the process, in which the upstream column undergoes loading and the downstream column undergoes elution, cleaning and equilibration, the two columns are interconnected at the BT point defined for the process, which in this case is equal to 1%. Then, the two columns are disconnected when the desired BT of the upstream column is reached, in this case equal to 70%. The upstream column

undergoes the same phases of the downstream column in the first step (i.e., elution, cleaning, and equilibration) while the downstream column continues the loading. In this way, using the twin-column technology efficiently loads the columns to maximize their resin utilization and thus allows for improving its productivity and solvent consumption.

Life cycle assessment. Given that the main reagent utilized (bromobenzene) is derived from fossil resources, the reduction of halobenzene usage would significantly improve the environmental performance of the product life cycle. In this sense, to evaluate the environmental profiles of the analyzed processes, we applied a life cycle assessment (LCA) methodology.[300] The LCA focused on the impacts associated with the production of the quantity of bromobenzene utilized per mg of final product. A cradle-to-gate scope and a cut-off system model based on mass allocation was defined. The environmental impact categories of global warming, fine particulate matter formation, and fossil resource scarcity were selected because, among the different 18 categories assessed in the ReCiPe midpoints impacts assessment method,[301–304] the impacts of bromobenzene production on these three categories contribute to over 90% of the aggregated environmental impacts on human health, ecosystems, and resources scarcity. Life cycle inventory for the production of bromobenzene was based on experimental data,[304] and the datasets for energy and materials flows based on European market from the life cycle inventory database (Ecoinvent 3.8).[303] The heating energy required in the bromobenzene preparation was thermodynamically estimated and adjusted by assuming an efficiency of 60% of the electric heating device.[305] The stirring energy was calculated based on a required power of 3.2 W at 700 rpm for stirring a 10 g of mixture and extrapolated to the specific quantity in the bromobenzene experiment. Regarding facilities and transport, a chemicals plant of 50 000 ton yearly production with a 50 year lifespan and transport by lorry and train for distances of 100 km and 600 km were considered.[306–308] Emissions to air during the process were assumed to be 0.2% of volatile input materials.[306] A 90% organic matter removal efficiency was assumed in the wastewater treatment, whose carbon is subsequently released into the air in the form of CO_2.[308] Finally, the impacts assessment results were obtained using the SimaPro 9.2 software.[307]

Circularity assessment. Different from the above LCA study, the circularity study investigated the formation of biphenyl, starting from three different halobenzene (chloro, bromo, and iodobenzene). The circularity methodology proposed by the Ellen MacArthur (EMA) foundation was applied, taking the material circular indicator (MCI) with values between 0 (linear) and 1 (circular).[309] A production of 100 mg of pure biphenyl was assumed as functional unit. The processes considered were batch and continuous-flow synthesis and included the corresponding batch and continuous purification. To determine the impact of mass recycling, two scenarios were considered: (1) not considering reactant recycling and (2) considering reactant recycling. To this aim, the following hypotheses were taken: (i) all mass flows of the process were calculated according to the functional unit, so the material loads are different between process layouts, but the same between scenarios; (ii) the same reaction yields were taken for the different halogen-based derivatives; (iii) when a reactant was not recycled, it was considered as wasted; (iv) secondary wastes were not considered and, thus, the extraction efficiency (EF) of a recycled reactant was assumed as 100% in all cases; (v) the utility factor $F(X)$, which includes the product intensity and lifetime, was considered invariant in this study. All parameters used were defined according to the definitions and equations given by the Ellen MacArthur (EMA) foundation.[309]

7.3. Results and Discussion

We initiated the work by optimizing the Suzuki–Miyaura reaction, a classical reaction applied in drug discovery and development, to prepare a biphenyl compound. The reaction is made of two steps: a Miyaura borylation where bromobenzene reacts with tetrahydroxydiboron to obtain phenylboronic acid, and a Suzuki C–C cross-coupling where the boronic acid obtained from the previous step reacts with bromobenzene to form biphenyl. The reactions were optimized on the commercial continuous-flow unit described before, equipped with a packed bed filled with Pd-based silica-supported heterogeneous catalyst (dibenzylideneacetone palladium(0) phosphaadamantane ethyl silica). Using a 'design of experiments' (DoE) approach, the borylation step was conducted in a systematic manner varying the temperature between 60 and 100 °C, and the

residence time between 30 and 120 min. The two reactants were injected together, and the product yield was calculated by HPLC. At the optimized 80 °C and 120 min conditions, the compound **2** was obtained with 86% yield. To highlight the advantage of the continuous-flow synthesis, we performed at comparative experimental conditions (*i.e.*, 80 °C and 120 min) the same reaction in a standard round-bottom flask, obtaining compound **2** with only a 67% total yield under batch mode. As discussed elsewhere, the higher yield in flow conditions can be ascribed to the improved contact of the liquid phase with the catalytic sites in flow.[310–312] The second step was performed by using the same continuous set-up described above. The formation of biphenyl was performed by injecting an ethanolic solution of bromobenzene and phenylboronic acid in the packed-bed reactor. Following the DoE approach, the reaction was conducted at different temperatures (from 100 to 150 °C) and residence times (from 30 to 120 min). The maximum yield of compound **3** (58%) was achieved at 150 °C and 60 min. Under batch conditions, compound **3** was achieved with only 45% yield, thus testifying the improvement brought by flow conditions. Having optimized the synthesis, we integrated the two continuous steps together to prepare biphenyl in one pot. We then moved to the development of a suitable purification process. We started from the traditional batch chromatography, in which the crude mixture is discontinuously loaded into a column, packed with a C18 resin, until its capacity is approached. The biphenyl compound obtained from the Suzuki–Miyaura reaction served as model species to demonstrate the effectiveness of this multidisciplinary approach. A breakthrough test was preliminarily carried out on the reaction product in order to determine the dynamic binding capacity of the resin, which is pivotal for establishing the conditions for its optimal utilization (Figure 7.2 a). The crude, at 2.37 mg mL^{-1} of product **3**, was loaded onto 1.66 mL of C18 resin and the product concentration in the eluate of the column was measured through a calibrated in-line UV-vis detector. The 1% breakthrough (BT), i.e., 1% of the product concentration in the feed, was measured in the eluate after having loaded 34 mL of crude. Considering
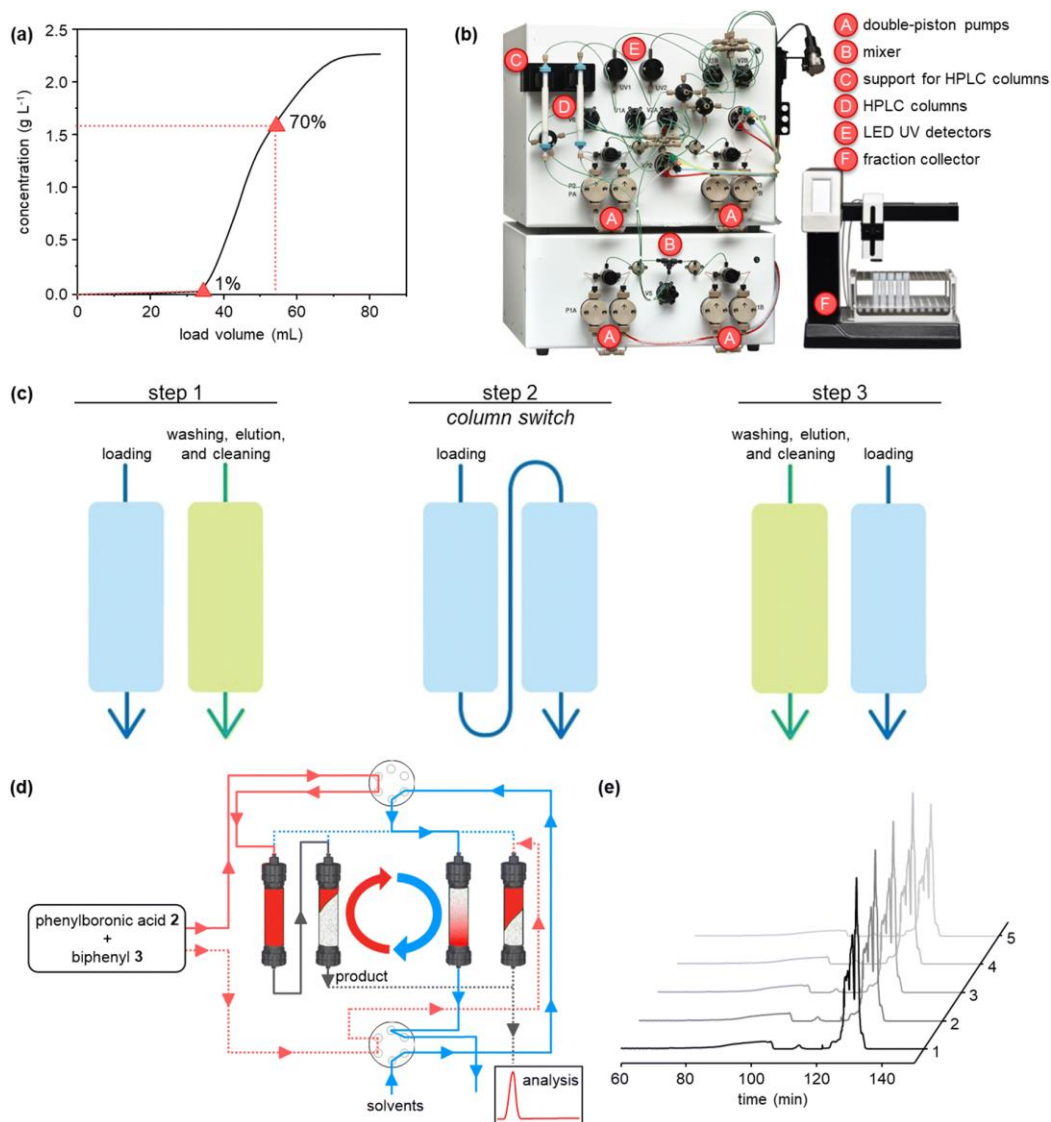
Figure 7.2. *Breakthrough curve for biphenyl product during batch and continuous chromatographic purification (a), showing improved performance over a multi-column continuous setup; photograph of the modified continuous moving bed chromatography setup (b); schematic representation of a half-cycle of the continuous operation, for the loading, washing, elution, and cleaning steps (c); schematic flow diagram of the continuous chromatography setup (d); UV traces of the five performed cycles during continuous synthesis and product purification (e).*

the operating linear velocity of 300 cm h^{-1}, the saturation time corresponding to the 1% BT was 61.5 min.[313–315] This means that, reached this loading volume, the product starts being lost in the eluate, with no more adsorption on the resin,

compromising the yield of the process. This was then considered as the reference loading for a batch single-column chromatography in order to avoid sacrificing the yield of the product. In this condition, a resin loading of 48.5 mg mL_{resin}^{-1} was achieved. Using this parameter, the initial separations were performed in batch. The crude, with an overall concentration of 3.5 mg mL^{-1}, was loaded up to the 1% BT estimated previously. After the loading, a washing step with 14 mM Na_2CO_3 was performed to desorb the impurities. Finally, the elution was operated with a step gradient to 100% acetonitrile and 1 mL fractions were collected during this phase to characterize the process. In particular, the yield and the biphenyl concentration in each fraction were determined by at-line HPLC analysis. The overall purity of the biphenyl collected from the batch process was about 86%. The yield, defined as the ratio between collected and injected product, was 51% for the batch process, while the productivity is 17 g h^{-1} L_{resin}^{-1} (Table 7.1). This poor yield was ascribed to the breakthrough of some product in the loading phase as well as in the washing step, required to desorb the impurities and reach acceptable standards of purity. In order to improve the downstream processing performances, we moved to a continuous countercurrent chromatography process based on two twin columns, directly applying it to our small molecules[301–304] In this approach, the crude is partialized into multiple columns, which undergo consecutive interconnected (series) and disconnected (parallel) operations ensuring the periodic continuity of the feeding and the necessary steps of cleaning-

Table 7.1. Comparison between batch and continuous-flow purification processes in the purification of biphenyl.

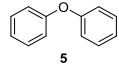|	Solvent consumption (L g^{-1})	Isolated yield (%)	Productivity (g h^{-1} L^{-1})	Purity (%)
Batch[a]	1.4	51.3	17.2	86.3
Continuous[a]	0.3	81.3	22.7	>99
Process gain[b] (batch *vs* continuous)	79.6%	58.5%	31.6%	15.9%

[a]Synthesis and purification conditions in Figure 7.2 b and in the Appendix A. [b]Process improvement between continuous-flow and batch experiments.

in-place and regeneration. This leads to higher resin utilization and process efficiency, due to the maximized driving force for mass transfer, ensured by the simulated countercurrent movement between the solid and liquid phases, and therefore an easier scalability for industrial processes. The set-up was composed by two supports for columns, two long lifetime LED UV detectors (280 and 300 nm recorded simultaneously), four high precision double-piston-pumps with active seal wash and one pump for feed supply. The chromatograph was equipped with two HPLC columns YMC-Triart Prep C18-S20 μm, each with a volume of 1.66 mL (Figure 7.2 b).

The purification cycle involved two phases (Figure 7.2 c and d): in the first one, the columns are interconnected and are employed in series to ensure that the product breaking through the upstream column during the loading is re-adsorbed in the downstream one. This allowed to push the loading phase to higher values of breakthrough. In this work, 70% BT, corresponding to a loaded volume of 54 mL, was applied. This enabled a higher loading of the resin, up to 77 mg mL$_{resin}^{-1}$, which in turns grants a better column utilization compared to the single-column configuration. In the second stage, the columns are employed in parallel, performing the washing, elution and regeneration of the upstream column while completing the loading of the downstream one. These two phases constitute a switch, after which the two columns reach the same initial conditions but with exchanged positions (*i.e.*, the upstream column becomes the downstream one and vice versa). Then, a full cycle comprises two symmetrical switches.

In our work, with only five cycles, we were able to purify the compounds. The UV traces recorded at the outlet of one of the two columns for these five cycles are shown in Figure 7.2 e, confirming the periodicity of the process, with good reproducibility of the chromatogram cycle after cycle. The peak corresponding to biphenyl can be appreciated at 130 min. From in-line HPLC analysis, we demonstrated that this product could be collected with high purity (>99%) in each cycle. The overall process performances of this continuous operation were evaluated by averaging the parameters obtained for the cycles that have reached the steady state (cycles 2, 3, and 4) and are reported in Table 7.1. In particular, biphenyl can be recovered, through this continuous chromatographic approach,

Table 7.2. Continuous synthesis of other small molecules.[a]
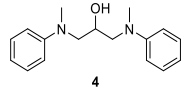
	Solvent consumption (L g^{-1})	Isolated yield (%)	Productivity (g h^{-1} L^{-1})	Purity (%)
4	2.4	68	7.5	93
5	2.4	71	7.1	92

[a]Synthesis and purification conditions in the Appendix A.

with 81% yield and productivity of 22.7 g h^{-1} L$_{resin}^{-1}$ at a purity of >99%. Thus, the continuous purification process provides increased yield and productivity, respectively by 59% and 32%, compared to the batch process. As shown in Table 1, the batch produced 80.5 mg of the product per run using 57.8 mL of the solvent while the continuous purification was able to produce 127.8 mg of the product per switch using 31.2 mL. This clear advantage could be summarized as the solvent utilized per purified product, or solvent consumption, which was 1.4 L g^{-1} for the batch and 0.3 L g^{-1} for the continuous purification. This remarkable reduction in the solvent consumption makes the continuous purification more attractive from an industrial and environmental viewpoint.

The broad applicability of our flow synthesis–purification method was demonstrated testing the protocol on different reaction mixtures. Among this, the symmetric aminoalcohol **4** and the diphenylether **5** were isolated using the same protocols validated above. As reported in Table 7.2, the separation provided products **4** and **5** in high purity (>90%), and with an overall yield of 68% and 71% respectively. Further information and comparative data with batch methods are reported in the Appendix A. The environmental impact as given by the LCA is assumed to be largely dependent on the reactant mass used to achieve the same quantity of product. This paper reported advances in the reduction of reactant mass by flow chemistry, over batch synthesis, and continuous-flow purification, over batch purification.
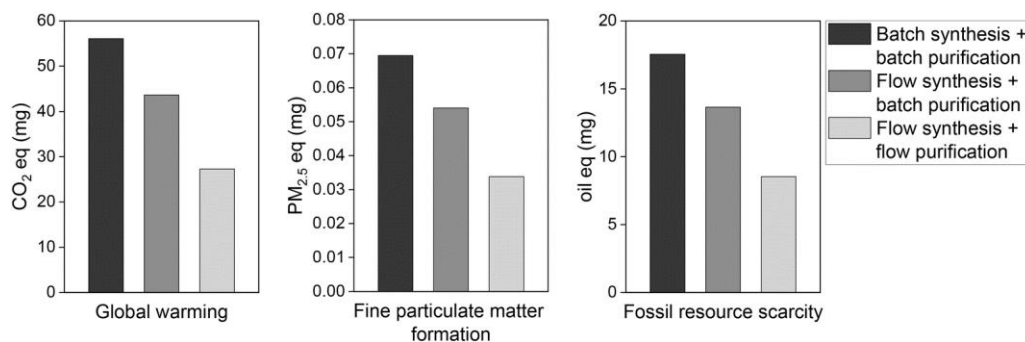
Figure 7.3. *Environmental impacts of bromobenzene used to obtain 1 mg of biphenyl by batch and flow processes.*

Table 7.3. *Circularity analysis per 100 mg of purified biphenyl obtained from bromobenzene reagent. The process is studied for the three cases, which include both synthesis and purification in batch and/or flow. For each design, two scenarios are proposed, namely without (A) and with (B) reactant recycling.*

	Using bromide derivatives					
Layout →	Batch + Batch		Conti + Batch		Conti + Conti	
Indicator	A	B	A	B	A	B
M (mg)[a]	3326	3326	1661	1661	1447	1447
F_R[b]	0.00	0.18	0.46	0.68	0.62	0.75
V (mg)[c]	3326	2733	895	526	550	355
C_U[d]	0.00	0.18	0.46	0.68	0.62	0.75
E_F[e]	1.00	1.00	1.00	1.00	1.00	1.00
W (mg)[f]	3226	2633	795	425	450	255
LFI[g]	0.98	0.81	0.51	0.29	0.35	0.21
F(X)[h]	0.9	0.9	0.9	0.9	0.9	0.9
MCI[i]	**0.114**	**0.274**	**0.542**	**0.742**	**0.689**	**0.810**

[a]Mass load entering the process (M); [b]recycled fraction (FR); [c]use of virgin materials (V); [d]reuse fraction (CU); [e]extraction efficiency (EF); [f]unrecoverable waste (W); [g]linear flow indicator (LFI); [h]utility factor F(X); [i]material circular indicator (MCI).

The LCA results show that, indeed, this process intensification is translated into environmental benefits (Figure 7.3). As expected, the reduction of the quantity of reagent used per mg of product generates proportionally reductions in the pollutant emissions and fossil resources scarcity. Hence, the total 56.1 mg CO_2 eq. emitted due to bromobenzene consumption in the batch synthesis to produce 1 mg of biphenyl are reduced by 51% in the flow synthesis process, *i.e.*, emitting only 27.3 mg CO_2 eq. per mg of product. Similarly, air pollutant emissions and the impacts on fossil resources scarcity are halved by switching the production process from batch to flow systems. A similar positive outcome was determined for the environmental impact categories fine particulate matter formation and fossil resource scarcity.

Together with the global warming, this provides a forecast both for most urgent global issues (warming, resources) and human health (particulate matter). The circularity assessment goes one step further in scope than the LCA, by considering the route to generate biphenyl. As the focus is on recycling, the lost and recovered mass loads determine the degree of circularity. The mass loads are reduced when switching from batch to continuous-flow, both for the synthesis and purification (Table 7.3).[316] In this sequence, the demand of virgin materials (V) decreases when the process is carried out continuously. Additionally, the recycled fraction (FR) is increased to a maximum value of 0.81, for a continuous synthesis and purification with reactants recycled and assuming synthesis using chlorobenzenes (Appendix A). Waste generation is also positively impacted, reaching a 95% reduction when using chloro-benzenes. The MCI metrics scores largest (0.859) for the best scenario. To summarize, the two-fold continuous process, continuous in synthesis and purification, is considerably better in the environmental performance, as evidenced by the LCA study. The circularity study confirmed this outcome, and outlined that the results would be significantly better when considering recycling of reactant waste and replacing the bromohalogens of the study with chlorohalogens.

7.4.   Conclusions

In conclusion, we have presented an improved protocol for the end-to-end

synthesis and multi-column preparative purification of small molecules, in an integrated manner and under continuous conditions. The approach was demonstrated for the synthesis of structurally-different organic compounds. In all cases, the flow method demonstrated higher product yields, quick product isolation, and reduced solvent consumption compared to traditional batch-type chromatography. Circularity and life cycle analyses further highlighted the environmental benefits for the integrated flow process. The approach may find applications in the design of new synthesis–purification–analysis platforms applied in drug discovery.

Chapter **8**

Conclusions and Outlook

Sustainable development goals have garnered increasing attentions with regard to the circularity of manufacturing processes. In the last decade, the role of continuous-flow chemistry as green enabling technology has emerged as a focal point for circularity, finding widespread applications in organic, pharmaceutical, and fine chemical synthesis. This technology has demonstrated notable advantages in terms of safety, efficiency, and sustainability. My PhD thesis has aimed to make a substantial contribution to the advancement of flow chemistry by providing a comprehensive understanding of the underlying principles and offering practical guidelines for designing highly effective and efficient synthetic procedures.

8.1.   Better Control of Hazardous and Multistep Reactions

The work presented in this PhD thesis has highlighted the role of flow chemistry in various processes, as this technology improves the efficiency of the reaction, enabling a better control of the temperature in hazardous conditions, and facilitating the reactions scale-up. This has been demonstrated in the exothermic production of azetidinium salts, in which the flow technology allowed safer and faster reaction conditions, due to the high surface-to-volume ratio of the microreactors. The advantages of flow chemistry were also demonstrated in the

highly hazardous synthesis of glycidol and glycidyl derivatives, by employing biphasic mixtures and integrating work-up steps under optimized conditions. The telescoped protocol allowed for the sequential execution of multiple steps without the need for intermediate isolation and purification, reducing the overall time and effort required for the synthesis.

8.2. Novel Photocatalytic Methods

Emphasis has been also placed in the development of novel, light-driven methods for the synthesis of pharmaceuticals. In particular, for the fabrication of carbon nitride-based materials with applications in visible light-driven processes, the ability to customize catalyst features was crucial for achieving improved catalytic performance. The possibility to finely tune the catalyst's surface area played a significant role in optimizing the trifluoromethylation process, which is a key transformation in pharmaceutical synthesis. Furthermore, the modulation of the bandgap by introducing different types of metals into the carbon nitride-based materials was investigated. This exploration provided valuable insights into the theorized reaction mechanism, shedding light on the factors influencing the catalytic performance. In addition, the utilization of single atom catalysts, a novel class of materials with properties intermediate between homogeneous and heterogeneous catalysts, was employed to improve catalytic performance in the benzyl alcohol oxidation process. This approach also offered valuable information regarding the role of the photoactive support in the oxidation reaction.

These strategies allowed to establish structure-performance relationships for each process by conducting comprehensive characterization of the prepared nanocatalysts. This provided in-depth insights into the catalyst's properties and their influence on catalytic performance. Moving forward, the integration of photocatalytic heterogeneous catalysis and flow chemistry presented a significant challenge, primarily related to suboptimal light penetration throughout the reactor volume, limiting the interaction between light and the catalyst. To address this challenge, the development of nanostructured reactors for flow applications has emerged as a promising solution in this PhD thesis. In particular, the fabrication of a new polymer-based material was investigated, focusing on its enhanced light

penetration capabilities due to the presence of carbon nitride as a photoactive component supported by a polymeric matrix. Extensive characterization of this highly photo-stable and recyclable material demonstrated the critical role of the material's structure and porosity in several photocatalytic processes.

Overall, the thesis further proves that photocatalysis remains a transformative cornerstone for harnessing solar irradiation to develop sustainable and environmentally friendly processes. This paradigm-shifting approach holds immense promise for revolutionizing the landscape of sustainable technologies and ushering in a brighter future for chemistry.

8.3. Technologies Integration

The final purpose of this PhD project was the development of flexible protocols for the preparation of pharmaceutical intermediates under continuous conditions, from the synthesis to the almost always required purification step. Particularly, we have investigated one application of the continuous chromatography approach particularly useful to separate binary mixtures, called simulating moving bed (SMB), in which a countercurrent flow between particles and fluids is simulated with a particular arrangement of columns. This step was integrated after the sequential catalysis step. The higher columns capacity and process efficiency was due to the maximized driving force for heat and mass transfer, and provided easier scalability and greener conditions.

8.4. Outlook

Continuous-flow chemistry, as showcased in this thesis, is poised to become an indispensable tool for organic synthesis and industrial manufacturing, offering a multitude of advantages in terms of sustainability, safety, and efficiency. The challenges and opportunities presented by flow chemistry are driving researchers to explore and advance the field. One key area of focus is the integration of flow chemistry with automation, which has the potential to revolutionize chemical manufacturing processes. Through this combination, it becomes possible to create fully continuous, digital, and environmentally friendly plants that eliminate waste generation and improve process efficiency. The automation of flow chemistry

systems enables precise control over reaction parameters, real-time monitoring, and rapid optimization, leading to enhanced productivity and reduced resource consumption. Additionally, the application of flow chemistry in novel research areas, such as circular processing and nanomaterial synthesis, holds great promise. Flow chemistry can contribute to improving the conversion of waste materials into value-added products through efficient and controlled reactions. This approach aligns with the principles of sustainable chemistry and circular economy, offering opportunities for the development of more environmentally friendly processes, also for what concerns greener pharmaceutical synthesis. Moreover, integrating downstream purification methods with upstream reaction systems remains a challenge. The availability of miniaturized work-up and purification setups that can seamlessly integrate with flow reactors is limited. Developing standardized and compatible systems for integrated purification and reaction setups is crucial to overcome this challenge and enable the seamless flow of reactions and purification steps.

Overall, the relevance and impact of flow chemistry will continue to expand in the coming years. Its advantages, such as improved efficiency, enhanced control, and reduced waste generation, will extend to various fields of research and industry. The examples highlighted in this PhD thesis confirm that some of the technical features necessary to address these challenges are already available and can be applied to existing and new processes.

Bibliography

(1)   Sivo, A.; Galaverna, R. de S.; Gomes, G. R.; Pastre, J. C.; Vilé, G. From Circular Synthesis to Material Manufacturing: Advances, Challenges, and Future Steps for Using Flow Chemistry in Novel Application Area. *React. Chem. Eng.* **2021**, *6* (5), 756–786.

(2)   Peng, Z.; Jimenez, J. L. Radical Chemistry in Oxidation Flow Reactors for Atmospheric Chemistry Research. *Chem. Soc. Rev.* **2020**, *49* (9), 2570–2616.

(3)   Sharma, M. K.; Raval, J.; Ahn, G.-N.; Kim, D.-P.; Kulkarni, A. A. Assessing the Impact of Deviations in Optimized Multistep Flow Synthesis on the Scale-Up. *React. Chem. Eng.* **2020**, *5* (5), 838–848.

(4)   Elsherbini, M.; Wirth, T. Electroorganic Synthesis under Flow Conditions. *Acc. Chem. Res.* **2019**, *52* (12), 3287–3296.

(5)   Plutschack, M. B.; Pieber, B.; Gilmore, K.; Seeberger, P. H. The Hitchhiker's Guide to Flow Chemistry. *Chem. Rev.* **2017**, *117* (18), 11796–11893.

(6)   Gutmann, B.; Cantillo, D.; Kappe, C. O. Continuous-Flow Technology-A Tool for the Safe Manufacturing of Active Pharmaceutical Ingredients. *Angew. Chem. Int. Ed.* **2015**, *54* (23), 6688–6728.

(7)   Newby, J. A.; Blaylock, D. W.; Witt, P. M.; Pastre, J. C.; Zacharova, M. K.; Ley, S. V.; Browne, D. L. Design and Application of a Low-

Temperature Continuous Flow Chemistry Platform. *Org. Process Res. Dev.* **2014**, *18* (10), 1211–1220.

(8)   Hessel, V.; Kralisch, D.; Kockmann, N.; Noël, T.; Wang, Q. Novel Process Windows for Enabling, Accelerating, and Uplifting Flow Chemistry. *ChemSusChem* **2013**, *6* (5), 746–789.

(9)   Baumann, M. Integrating Continuous Flow Synthesis with In-Line Analysis and Data Generation. *Org. Biomol. Chem.* **2018**, **16** (33), 5946–5954.

(10)   Fanelli, F.; Parisi, G.; Degennaro, L.; Luisi, R. Contribution of Microreactor Technology and Flow Chemistry to the Development of Green and Sustainable Synthesis. *Beilstein J. Org. Chem.* **2017**, *13*, 520–542.

(11)   Musci, P.; Colella, M.; Sivo, A.; Romanazzi, G.; Luisi, R.; Degennaro, L. Flow Microreactor Technology for Taming Highly Reactive Chloroiodomethyllithium Carbenoid: Direct and Chemoselective Synthesis of α-Chloroaldehydes. *Org. Lett.* **2020**, *22* (9), 3623–3627.

(12)   Colella, M.; Nagaki, A.; Luisi, R. Flow Technology for the Genesis and Use of (Highly) Reactive Organometallic Reagents. *Chem. Eur. J.* **2020**, *26* (1), 19–32.

(13)   Wegner, J.; Ceylan, S.; Kirschning, A. Flow Chemistry – A Key Enabling Technology for (Multistep) Organic Synthesis. *Adv. Synth. Catal.* **2012**, *354* (1), 17–57.

(14)   Damião, M. C. F. C. B.; Galaverna, R.; Kozikowski, A. P.; Eubanks, J.; Pastre, J. C. Telescoped Continuous Flow Generation of a Library of Highly Substituted 3-Thio-1,2,4-Triazoles. *React. Chem. Eng.* **2017**, *2* (6), 896–907.

(15)   Damião, M. C. F. C. B.; Marçon, H. M.; Pastre, J. C. Continuous Flow Synthesis of the URAT1 Inhibitor Lesinurad. *React. Chem. Eng.* **2020**, *5* (5), 865–872.

(16)   Pastre, J. C.; Browne, D. L.; Ley, S. V. Flow Chemistry Syntheses of Natural Products. *Chem. Soc. Rev.* **2013**, *42* (23), 8849.

(17)   Ley, S. V. On Being Green: Can Flow Chemistry Help? *Chem. Rec.* **2012**, *12* (4), 378–390.

(18) Gioiello, A.; Mancino, V.; Filipponi, P.; Mostarda, S.; Cerra, B. Concepts and Optimization Strategies of Experimental Design in Continuous-Flow Processing. *J. Flow Chem.* **2016**, *6* (3), 167–180.

(19) Cerra, B.; Mangiavacchi, F.; Santi, C.; Lozza, A. M.; Gioiello, A. Selective Continuous Flow Synthesis of Hydroxy Lactones from Alkenoic Acids. *React. Chem. Eng.* **2017**, *2* (4), 467–471.

(20) Gioiello, A.; Piccinno, A.; Lozza, A. M.; Cerra, B. The Medicinal Chemistry in the Era of Machines and Automation: Recent Advances in Continuous Flow Technology. *J. Med. Chem.* **2020**, *63* (13), 6624–6647.

(21) Baxendale, I. R.; Deeley, J.; Griffiths-Jones, C. M.; Ley, S. V.; Saaby, S.; Tranmer, G. K. A Flow Process for the Multi-Step Synthesis of the Alkaloid Natural Product Oxomaritidine: A New Paradigm for Molecular Assembly. *Chem. Commun.* **2006**, *24*, 2566.

(22) Dalla-Vechia, L.; Reichart, B.; Glasnov, T.; Miranda, L. S. M.; Kappe, C. O.; de Souza, R. O. M. A. A Three Step Continuous Flow Synthesis of the Biaryl Unit of the HIV Protease Inhibitor Atazanavir. *Org. Biomol. Chem.* **2013**, *11* (39), 6806–6813.

(23) Adamo, A.; Beingessner, R. L.; Behnam, M.; Chen, J.; Jamison, T. F.; Jensen, K. F.; Monbaliu, J.-C. M.; Myerson, A. S.; Revalor, E. M.; Snead, D. R.; Stelzer, T.; Weeranoppanant, N.; Wong, S. Y.; Zhang, P. On-Demand Continuous-Flow Production of Pharmaceuticals in a Compact, Reconfigurable System. *Science* **2016**, *352*, 61–67.

(24) Chanda, A.; Daly, A. M.; Foley, D. A.; LaPack, M. A.; Mukherjee, S.; Orr, J. D.; Reid, G. L.; Thompson, D. R.; Ward, H. W. Industry Perspectives on Process Analytical Technology: Tools and Applications in API Development. *Org. Process Res. Dev.* **2015**, *19* (1), 63–83.

(25) U.S. Department of Health and Human Services - Food and Drug Administration, Quality Considerations for Continuous Manufacturing.

(26) Palmer, E. GSK Opens $95M Continuous Production Operation in Singapore, Available at: Https://Www.Fiercepharma.Com/Manufacturing/Gsk-Opens-130m-Continuous-Productionfacilities-Singapore (Accessed 29 June 2020).

(27) Palmer, E. Glaxo to Use New Technology in India Plant, Available at: Https://Www.Fiercepharma.Com/Partnering/Glaxo-to-Usenew-Technology-India-Plant (Accessed 20 November 2020).

(28)   Cole, K. P.; Groh, J. M.; Johnson, M. D.; Burcham, C. L.; Campbell, B. M.; Diseroad, W. D.; Heller, M. R.; Howell, J. R.; Kallman, N. J.; Koenig, T. M.; May, S. A.; Miller, R. D.; Mitchell, D.; Myers, D. P.; Myers, S. S.; Phillips, J. L.; Polster, C. S.; White, T. D.; Cashman, J.; Hurley, D.; Moylan, R.; Sheehan, P.; Spencer, R. D.; Desmond, K.; Desmond, P.; Gowran, O. Kilogram-Scale Prexasertib Monolactate Monohydrate Synthesis under Continuous-Flow CGMP Conditions. *Science* **2017**, *356*, 1144–1150.

(29)   Eli Lilly, Meet Eli Lilly and Company - 2019 Facility of the Year Process Innovation Category Winner, Available at: Https://Ispe.Org/Pharmaceutical-Engineering/Ispeak/Meet-Elililly-Andcompany-2019-Facility-Year-Process-Innovation (Accessed 04 July 2020).

(30)   Brennan, Z. FDA Calls on Manufacturers to Begin Switch from Batch to Continuous Production, Available at: Https://Www. Outsourcing-Pharma.Com/Article/2015/05/01/FDA-Calls-Onmanufacturers-to-Begin-Switch-from-Batch-to-Continuousproduction (Accessed 05 July 2020).

(31)   Harsanyi, A.; Conte, A.; Pichon, L.; Rabion, A.; Grenier, S.; Sandford, G. One-Step Continuous Flow Synthesis of Antifungal WHO Essential Medicine Flucytosine Using Fluorine. *Org. Process Res. Dev.* **2017**, *21* (2), 273–276.

(32)   Desai, B.; Dixon, K.; Farrant, E.; Feng, Q.; Gibson, K. R.; van Hoorn, W. P.; Mills, J.; Morgan, T.; Parry, D. M.; Ramjee, M. K.; Selway, C. N.; Tarver, G. J.; Whitlock, G.; Wright, A. G. Rapid Discovery of a Novel Series of Abl Kinase Inhibitors by Application of an Integrated Microfluidic Synthesis and Screening Platform. *J. Med. Chem.* **2013**, *56* (7), 3033–3047.

(33)   Keenan, J. Cambrex Caps Latest Addition of Continuous-Flow Manufacturing at North Carolina Plant, Available at: Https://www.Fiercepharma.Com/Manufacturing/Cambrex-Caps-Latestaddition-Continuous-Flow-Manufacturing-at-North-Carolinaplant (Accessed 04 July 2020).

(34)   Lynch, M. Flexibility, Agility and Quality Assurance: Advantages of Continuous Manufacturing, Available at: Https://www.Outsourcing-Pharma.Com/Article/2019/04/10/Janssenon-the-Benefits-of-Continuous-Manufacture (Accessed 05 July 2020).

(35) Makgwane, P. R.; Ray, S. S. Synthesis of Nanomaterials by Continuous-Flow Microfluidics: A Review. *J. Nanosci. Nanotechnol.* **2014**, *14* (2), 1338–1363.

(36) Loizou, K.; Mourdikoudis, S.; Sergides, A.; Besenhard, M. O.; Sarafidis, C.; Higashimine, K.; Kalogirou, O.; Maenosono, S.; Thanh, N. T. K.; Gavriilidis, A. Rapid Millifluidic Synthesis of Stable High Magnetic Moment Fe x C y Nanoparticles for Hyperthermia. *ACS Appl. Mater. Interfaces* **2020**, *12* (25), 28520–28531.

(37) Romashov, L. V.; Ananikov, V. P. Alkynylation of Bio-Based 5-Hydroxymethylfurfural to Connect Biomass Processing with Conjugated Polymers and Furanic Pharmaceuticals. *Chem. Asian J.* **2017**, *12* (20), 2652–2655.

(38) Castello, D.; Pedersen, T.; Rosendahl, L. Continuous Hydrothermal Liquefaction of Biomass: A Critical Review. *Energies* **2018**, *11* (11), 3165.

(39) Maschmeyer, T.; Humphreys, L. J. Methods for Biofuel Production. WO2011/123897 A1, **2011**.

(40) Maschmeyer, T. Processing of Organic Matter. WO2012/ 092644 A1, **2012**.

(41) Lane, J. The Silver in Silva: The Story of Steeper Energy and SGF's's $59M Advanced Biofuels Project in Norway, Available at: Https://Www.Biofuelsdigest.Com/Bdigest/2018/ 01/16/the-Silver-in-Silva-the-Story-of-Steeper-Energys-59madvanced- Biofuels-Project (Accessed 07 July 2020).

(42) Steeper Energy, Hydrofaction®, Available at: Https:// Steeperenergy.Com/Hydrofaction/ (Accessed 06 July 2020).

(43) Jensen, C. U.; Rodriguez Guerrero, J. K.; Karatzos, S.; Olofsson, G.; Iversen, S. B. Fundamentals of HydrofactionTM: Renewable Crude Oil from Woody Biomass. *Biomass Convers. Biorefin.* **2017**, *7* (4), 495–509.

(44) Bosetti, A.; Bianchi, D.; Franzosi, G.; Ricci, M. Processfor the Production of Bio-Oil from Solid Urban Waste. WO2011/030196 A1, **2011**.

(45) ENI S.p.A., Waste-Tofuel, Available at: Https://Www.Eni.Com/En-IT/Operations/ Waste-to-Fuel.Html (Accessed 08 July 2020).

(46) Beston (Henan) Machinery Co., Ltd., Continuous Waste Tyre Pyrolysis Plant, Available at: Https://Www.Bestongroup.Com/Continuous-Waste-Tyre-Pyrolysis-Plant/ (Accessed 08 July 2020).

(47) Henan Mingjie Environmental Equipment Co., Ltd., Fully Continuous Pyrolysis Plant, Https://Www.Mingjiegroup.Com/Products/Fully_continuous_pyrolysis_Plant.Html?Gclid=Cj0KCQjwl4v4BRDaARIsAFjATPkepBDLCIRloMJTdbMrEIYC8po0GLKQ5gqNeYWCFaHmVxdMa2bcLcQaAo9MEALw_wcB (Accessed 08 July 2020).

(48) Hommes, A.; Heeres, H. J.; Yue, J. Catalytic Transformation of Biomass Derivatives to Value-Added Chemicals and Fuels in Continuous Flow Microreactors. *ChemCatChem* **2019**, *11* (19), 4671–4708.

(49) Gérardy, R.; Morodo, R.; Estager, J.; Luis, P.; Debecker, D. P.; Monbaliu, J.-C. M. Sustaining the Transition from a Petrobased to a Biobased Chemical Industry with Flow Chemistry. *Top. Curr. Chem.* **2019**, *377*, 1.

(50) Keijer, T.; Bakker, V.; Slootweg, J. C. Circular Chemistry to Enable a Circular Economy. *Nat. Chem.* **2019**, *11* (3), 190–195.

(51) Slootweg, J. C. Using Waste as Resource to Realize a Circular Economy: Circular Use of C, N and P. *Curr. Opin. Green Sustain. Chem.* **2020**, *23*, 61–66.

(52) Wardenier, N.; Gorbanev, Y.; Van Moer, I.; Nikiforov, A.; Van Hulle, S. W. H.; Surmont, P.; Lynen, F.; Leys, C.; Bogaerts, A.; Vanraes, P. Removal of Alachlor in Water by Non-Thermal Plasma: Reactive Species and Pathways in Batch and Continuous Process. *Water Res.* **2019**, *161*, 549–559.

(53) Becker, D.; Rodriguez-Mozaz, S.; Insa, S.; Schoevaart, R.; Barceló, D.; de Cazes, M.; Belleville, M.-P.; Sanchez-Marcano, J.; Misovic, A.; Oehlmann, J.; Wagner, M. Removal of Endocrine Disrupting Chemicals in Wastewater by Enzymatic Treatment with Fungal Laccases. *Org. Process Res. Dev.* **2017**, *21* (4), 480–491.

(54) Braga, A. H.; Vidinha, P.; Rossi, L. M. Hydrogenation of Carbon Dioxide: From Waste to Value. *Curr. Opin. Green Sustain. Chem.* **2020**, *26*, 100386.

(55) Siudyga, T.; Kapkowski, M.; Bartczak, P.; Zubko, M.; Szade, J.; Balin, K.; Antoniotti, S.; Polanski, J. Ultra-Low Temperature Carbon (Di)Oxide Hydrogenation Catalyzed by Hybrid Ruthenium–Nickel Nanocatalysts: Towards Sustainable Methane Production. *Green Chem.* **2020**, *22* (15), 5143–5150.

(56)   Ren, S.; Joulié, D.; Salvatore, D.; Torbensen, K.; Wang, M.; Robert, M.; Berlinguette, C. P. Molecular Electrocatalysts Can Mediate Fast, Selective CO_2 Reduction in a Flow Cell. *Science* **2019**, *365*, 367–369.

(57)   Jeng, E.; Jiao, F. Investigation of CO_2 Single-Pass Conversion in a Flow Electrolyzer. *React. Chem. Eng.* **2020**, *5* (9), 1768–1775.

(58)   Bui, T. Q.; Konwar, L. J.; Samikannu, A.; Nikjoo, D.; Mikkola, J.-P. Mesoporous Melamine-Formaldehyde Resins as Efficient Heterogeneous Catalysts for Continuous Synthesis of Cyclic Carbonates from Epoxides and Gaseous CO_2. *ACS Sustain. Chem. Eng.* **2020**, *8* (34), 12852–12869.

(59)   Schotten, C.; Plaza, D.; Manzini, S.; Nolan, S. P.; Ley, S. V.; Browne, D. L.; Lapkin, A. Continuous Flow Metathesis for Direct Valorization of Food Waste: An Example of Cocoa Butter Triglyceride. *ACS Sustain. Chem. Eng.* **2015**, *3* (7), 1453–1459.

(60)   Pfab, E.; Filiciotto, L.; Romero, A. A.; Luque, R. Valorization of Humins-Extracted 5-Methoxymethylfurfural: Toward High Added Value Furanics via Continuous Flow Catalytic Hydrogenation. *Ind. Eng. Chem. Res.* **2019**, *58* (35), 16065–16070.

(61)   Questell-Santiago, Y. M.; Galkin, M. V.; Barta, K.; Luterbacher, J. S. Stabilization Strategies in Biomass Depolymerization Using Chemical Functionalization. *Nat. Rev. Chem.* **2020**, *4* (6), 311–330.

(62)   Tang, X.; Zuo, M.; Li, Z.; Liu, H.; Xiong, C.; Zeng, X.; Sun, Y.; Hu, L.; Liu, S.; Lei, T.; Lin, L. Green Processing of Lignocellulosic Biomass and Its Derivatives in Deep Eutectic Solvents. *ChemSusChem* **2017**, *10* (13), 2696–2706.

(63)   Fang, R.; Dhakshinamoorthy, A.; Li, Y.; Garcia, H. Metal Organic Frameworks for Biomass Conversion. *Chem. Soc. Rev.* **2020**, *49* (11), 3638–3687.

(64)   Park, C.; Lee, J. Recent Achievements in CO_2-Assisted and CO_2-Catalyzed Biomass Conversion Reactions. *Green Chem.* **2020**, *22* (9), 2628–2642.

(65)   Dwi Prasetyo, W.; Putra, Z. A.; Bilad, M. R.; Mahlia, T. M. I.; Wibisono, Y.; Nordin, N. A. H.; Wirzal, M. D. H. Insight into the Sustainable Integration of Bio- and Petroleum Refineries for the Production of Fuels and Chemicals. *Polymer* **2020**, *12* (5), 1091.

(66)   Bertella, S.; Luterbacher, J. S. Lignin Functionalization for the Production of Novel Materials. *Trends Chem.* **2020**, *2* (5), 440–453.

(67) Liberato, V.; Benevenuti, C.; Coelho, F.; Botelho, A.; Amaral, P.; Pereira, N.; Ferreira, T. Clostridium Sp. as Bio-Catalyst for Fuels and Chemicals Production in a Biorefinery Context. *Catalysts* **2019**, *9* (11), 962.

(68) Cho, E. J.; Trinh, L. T. P.; Song, Y.; Lee, Y. G.; Bae, H.-J. Bioconversion of Biomass Waste into High Value Chemicals. *Bioresour. Technol.* **2020**, *298*, 122386.

(69) Hone, C. A.; Lopatka, P.; Munday, R.; O'Kearney-McMullan, A.; Kappe, C. O. Continuous-flow Synthesis of Aryl Aldehydes by Pd-catalyzed Formylation of Aryl Bromides Using Carbon Monoxide and Hydrogen. *ChemSusChem* **2019**, *12* (1), 326–337.

(70) Galaverna, R.; Fernandes, L. P.; Browne, D. L.; Pastre, J. C. Continuous Flow Processing as a Tool for the Generation of Terpene-Derived Monomer Libraries. *React. Chem. Eng.* **2019**, *4* (2), 362–367.

(71) Gérardy, R.; Debecker, D. P.; Estager, J.; Luis, P.; Monbaliu, J.-C. M. Continuous Flow Upgrading of Selected C2–C6 Platform Chemicals Derived from Biomass. *Chem. Rev.* **2020**, *120* (15), 7219–7347.

(72) Galaverna, R.; Breitkreitz, M. C.; Pastre, J. C. Conversion of d-Fructose to 5-(Hydroxymethyl)Furfural: Evaluating Batch and Continuous Flow Conditions by Design of Experiments and In-Line FTIR Monitoring. *ACS Sustain. Chem. Eng.* **2018**, *6* (3), 4220–4230.

(73) Tadele, K.; Verma, S.; Gonzalez, M. A.; Varma, R. S. A Sustainable Approach to Empower the Bio-Based Future: Upgrading of Biomass via Process Intensification. *Green Chem.* **2017**, *19* (7), 1624–1627.

(74) Luo, Z.; Qin, S.; Chen, S.; Hui, Y.; Zhao, C. Selective Conversion of Lignin to Ethylbenzene. *Green Chem.* **2020**, *22* (6), 1842–1850.

(75) De Clercq, R.; Dusselier, M.; Makshina, E.; Sels, B. F. Catalytic Gas-Phase Production of Lactide from Renewable Alkyl Lactates. *Angew. Chem. Int. Ed.* **2018**, *57* (12), 3074–3078.

(76) Jiménez-Gómez, C. P.; Cecilia, J. A.; García-Sancho, C.; Moreno-Tost, R.; Maireles-Torres, P. Selective Production of Furan from Gas-Phase Furfural Decarbonylation on Ni-MgO Catalysts. *ACS Sustain. Chem. Eng.* **2019**, *7* (8), 7676–7685.

(77) Peschke, T.; Bitterwolf, P.; Gallus, S.; Hu, Y.; Oelschlaeger, C.; Willenbacher, N.; Rabe, K. S.; Niemeyer, C. M. Self-Assembling All-Enzyme Hydrogels for Flow Biocatalysis. *Angew. Chem. Int. Ed.* **2018**, *130* (52), 17274–17278.

(78) Hartley, C. J.; Williams, C. C.; Scoble, J. A.; Churches, Q. I.; North, A.; French, N. G.; Nebl, T.; Coia, G.; Warden, A. C.; Simpson, G.; Frazer, A. R.; Jensen, C. N.; Turner, N. J.; Scott, C. Engineered Enzymes That Retain and Regenerate Their Cofactors Enable Continuous-Flow Biocatalysis. *Nat. Catal.* **2019**, *2* (11), 1006–1015.

(79) Planchestainer, M.; Contente, M. L.; Cassidy, J.; Molinari, F.; Tamborini, L.; Paradisi, F. Continuous Flow Biocatalysis: Production and in-Line Purification of Amines by Immobilised Transaminase from Halomonas Elongata. *Green Chem.* **2017**, *19* (2), 372–375.

(80) Roura Padrosa, D.; Benítez-Mateos, A. I.; Calvey, L.; Paradisi, F. Cell-Free Biocatalytic Syntheses of l-Pipecolic Acid: A Dual Strategy Approach and Process Intensification in Flow. *Green Chem.* **2020**, *22* (16), 5310–5316.

(81) De Martino, M. T.; Tonin, F.; Yewdall, N. A.; Abdelghani, M.; Williams, D. S.; Hanefeld, U.; Rutjes, F. P. J. T.; Abdelmohsen, L. K. E. A.; van Hest, J. C. M. Compartmentalized Cross-Linked Enzymatic Nano -Aggregates (c-CLE*n*A) for Efficient in-Flow Biocatalysis. *Chem. Sci.* **2020**, *11* (10), 2765–2769.

(82) Weiser, D.; Nagy, F.; Bánóczi, G.; Oláh, M.; Farkas, A.; Szilágyi, A.; László, K.; Gellért, Á.; Marosi, G.; Kemény, S.; Poppe, L. Immobilization Engineering – How to Design Advanced Sol–Gel Systems for Biocatalysis? *Green Chem.* **2017**, *19* (16), 3927–3937.

(83) Britton, J.; Dyer, R. P.; Majumdar, S.; Raston, C. L.; Weiss, G. A. Ten-Minute Protein Purification and Surface Tethering for Continuous-Flow Biocatalysis. *Angew. Chem. Int. Ed.* **2017**, *129* (9), 2336–2341.

(84) Velasco-Lozano, S.; Benítez-Mateos, A. I.; López-Gallego, F. Co-immobilized Phosphorylated Cofactors and Enzymes as Self-Sufficient Heterogeneous Biocatalysts for Chemical Processes. *Angew. Chem Int. Ed.* **2017**, *56* (3), 771–775.

(85) Vilé, G.; Schmidt, G.; Richard-Bildstein, S.; Abele, S. Enantiospecific Cyclization of Methyl N-(Tert-Butoxycarbonyl)-N-(3-Chloropropyl)-D-Alaninate to 2-Methylproline Derivative via 'Memory of Chirality' in Flow. *J. Flow Chem.* **2019**, *9* (1), 19–25.

(86) Colella, M.; Tota, A.; Takahashi, Y.; Higuma, R.; Ishikawa, S.; Degennaro, L.; Luisi, R.; Nagaki, A. Fluoro-Substituted Methyllithium Chemistry: External Quenching Method Using Flow Microreactors. *Angew. Chem. Int. Ed.* **2020**, *132* (27), 11016–11020.

(87)   Usutani, H.; Nihei, T.; Papageorgiou, C. D.; Cork, D. G. Development and Scale-up of a Flow Chemistry Lithiation–Borylation Route to a Key Boronic Acid Starting Material. *Org. Process Res. Dev.* **2017**, *21* (4), 669–673.

(88)   Yasukouchi, H.; Nishiyama, A.; Mitsuda, M. Safe and Efficient Phosgenation Reactions in a Continuous Flow Reactor. *Org. Process Res. Dev.* **2018**, *22* (2), 247–251.

(89)   Vilé, G.; Albani, D.; Nachtegaal, M.; Chen, Z.; Dontsova, D.; Antonietti, M.; López, N.; Pérez-Ramírez, J. A Stable Single-Site Palladium Catalyst for Hydrogenations. *Angew. Chem. Int. Ed.* **2015**, *54* (38), 11265–11269.

(90)   Vilé, G.; Albani, D.; Almora-Barrios, N.; López, N.; Pérez-Ramírez, J. Advances in the Design of Nanostructured Catalysts for Selective Hydrogenation. *ChemCatChem* **2016**, *8* (1), 21–33.

(91)   Vilé, G.; Almora-Barrios, N.; Mitchell, S.; López, N.; Pérez-Ramírez, J. From the Lindlar Catalyst to Supported Ligand-Modified Palladium Nanoparticles: Selectivity Patterns and Accessibility Constraints in the Continuous-Flow Three-Phase Hydrogenation of Acetylenic Compounds. *Chem. Eur. J.* **2014**, *20* (20), 5926–5937.

(92)   Cantillo, D.; de Frutos, O.; Rincón, J. A.; Mateos, C.; Kappe, C. O. A Continuous-Flow Protocol for Light-Induced Benzylic Fluorinations. *J. Org. Chem.* **2014**, *79* (17), 8486–8490.

(93)   Chen, Y.; Hone, C. A.; Gutmann, B.; Kappe, C. O. Continuous Flow Synthesis of Carbonylated Heterocycles via Pd-Catalyzed Oxidative Carbonylation Using CO and O_2 at Elevated Temperatures and Pressures. *Org. Process Res. Dev.* **2017**, *21* (7), 1080–1087.

(94)   Tortoioli, S.; Friedli, A.; Prud'homme, A.; Richard-Bildstein, S.; Kohler, P.; Abele, S.; Vilé, G. Development of an Efficient and Sustainable Synthesis of 2-(3-Methyl-1 H -1,2,4-Triazol-1-Yl) Acetic Acid under Continuous-Flow Conditions. *Green Chem.* **2020**, *22* (12), 3748–3758.

(95)   Bogdan, A. R.; Sach, N. W. The Use of Copper Flow Reactor Technology for the Continuous Synthesis of 1,4-Disubstituted 1,2,3-Triazoles. *Adv. Synth. Catal.* **2009**, *351* (6), 849–854.

(96)   Monteiro, J.; Pieber, B.; Corrêa, A.; Kappe, C. Continuous Synthesis of Hydantoins: Intensifying the Bucherer–Bergs Reaction. *Synlett* **2015**, *27* (01), 83–87.

(97) O'Brien, M.; Baxendale, I. R.; Ley, S. V. Flow Ozonolysis Using a Semipermeable Teflon AF-2400 Membrane To Effect Gas−Liquid Contact. *Org. Lett.* **2010**, *12* (7), 1596–1598.

(98) Yang, L.; Jensen, K. F. Mass Transport and Reactions in the Tube-in-Tube Reactor. *Org. Process Res. Dev.* **2013**, *17* (6), 927–933.

(99) Pastre, J. C.; Browne, D. L.; O'Brien, M.; Ley, S. V. Scaling Up of Continuous Flow Processes with Gases Using a Tube-in-Tube Reactor: Inline Titrations and Fanetizole Synthesis with Ammonia. *Org. Process Res. Dev.* **2013**, *17* (9), 1183–1191.

(100) Mastronardi, F.; Gutmann, B.; Kappe, C. O. Continuous Flow Generation and Reactions of Anhydrous Diazomethane Using a Teflon AF-2400 Tube-in-Tube Reactor. *Org. Lett.* **2013**, *15* (21), 5590–5593.

(101) Brzozowski, M.; O'Brien, M.; Ley, S. V.; Polyzos, A. Flow Chemistry: Intelligent Processing of Gas–Liquid Transformations Using a Tube-in-Tube Reactor. *Acc. Chem. Res.* **2015**, *48* (2), 349–362.

(102) Jolley, K. E.; Chapman, M. R.; Blacker, A. J. A General and Atom-Efficient Continuous-Flow Approach to Prepare Amines, Amides and Imines via Reactive N -Chloramines. *Beilstein J. Org. Chem.* **2018**, *14*, 2220–2228.

(103) Murray, P. R. D.; Browne, D. L.; Pastre, J. C.; Butters, C.; Guthrie, D.; Ley, S. V. Continuous Flow-Processing of Organometallic Reagents Using an Advanced Peristaltic Pumping System and the Telescoped Flow Synthesis of (E/Z)-Tamoxifen. *Org. Process Res. Dev.* **2013**, *17* (9), 1192–1208.

(104) Cao, Y.; Adriaenssens, B.; de A. Bartolomeu, A.; Laudadio, G.; de Oliveira, K. T.; Noël, T. Accelerating Sulfonyl Fluoride Synthesis through Electrochemical Oxidative Coupling of Thiols and Potassium Fluoride in Flow. *J. Flow Chem.* **2020**, *10* (1), 191–197.

(105) Laudadio, G.; Deng, Y.; van der Wal, K.; Ravelli, D.; Nuño, M.; Fagnoni, M.; Guthrie, D.; Sun, Y.; Noël, T. C(Sp3)–H Functionalizations of Light Hydrocarbons Using Decatungstate Photocatalysis in Flow. *Science* **2020**, *369*, 92–96.

(106) Wen, Z.; Maheshwari, A.; Sambiagio, C.; Deng, Y.; Laudadio, G.; Van Aken, K.; Sun, Y.; Gemoets, H. P. L.; Noël, T. Optimization of a Decatungstate-Catalyzed C(Sp3)–H Alkylation Using a Continuous

Oscillatory Millistructured Photoreactor. *Org. Process Res. Dev.* **2020**, *24* (10), 2356–2361.

(107) Noël, T.; Cao, Y.; Laudadio, G. The Fundamentals Behind the Use of Flow Reactors in Electrochemistry. *Acc. Chem. Res.* **2019**, *52* (10), 2858–2869.

(108) Cambié, D.; Bottecchia, C.; Straathof, N. J. W.; Hessel, V.; Noël, T. Applications of Continuous-Flow Photochemistry in Organic Synthesis, Material Science, and Water Treatment. *Chem. Rev.* **2016**, *116* (17), 10276–10341.

(109) Su, Y.; Straathof, N. J. W.; Hessel, V.; Noël, T. Photochemical Transformations Accelerated in Continuous-Flow Reactors: Basic Concepts and Applications. *Chem. Eur. J.* **2014**, *20* (34), 10562–10589.

(110) He, Z.; Bae, M.; Wu, J.; Jamison, T. F. Synthesis of Highly Functionalized Polycyclic Quinoxaline Derivatives Using Visible-Light Photoredox Catalysis. *Angew. Chem. Int. Ed.* **2014**, *126* (52), 14679–14683.

(111) Chen, Z.; Vorobyeva, E.; Mitchell, S.; Fako, E.; Ortuño, M. A.; López, N.; Collins, S. M.; Midgley, P. A.; Richard, S.; Vilé, G.; Pérez-Ramírez, J. A Heterogeneous Single-Atom Palladium Catalyst Surpassing Homogeneous Systems for Suzuki Coupling. *Nat. Nanotechnol.* **2018**, *13* (8), 702–707.

(112) Vilé, G.; Richard-Bildstein, S.; Lhuillery, A.; Rueedi, G. Electrophile, Substrate Functionality, and Catalyst Effects in the Synthesis of α-Mono and Di-Substituted Benzylamines via Visible-Light Photoredox Catalysis in Flow. *ChemCatChem* **2018**, *10* (17), 3786–3794.

(113) Hauschild, M. Z., Rosenbaum, R. K., Olsen, S. *Life Cycle Assessment*. Springer International Publishing: Cham, **2018**.

(114) Tsang, M.; Philippot, G.; Aymonier, C.; Sonnemann, G. Anticipatory Life-Cycle Assessment of Supercritical Fluid Synthesis of Barium Strontium Titanate Nanoparticles. *Green Chem.* **2016**, *18* (18), 4924–4933.

(115) Bédard, A.-C.; Longstreet, A. R.; Britton, J.; Wang, Y.; Moriguchi, H.; Hicklin, R. W.; Green, W. H.; Jamison, T. F. Minimizing E-Factor in the Continuous-Flow Synthesis of Diazepam and Atropine. *Bioorg. Med. Chem.* **2017**, *25* (23), 6233–6241.

(116) Yaseneva, P.; Hodgson, P.; Zakrzewski, J.; Falß, S.; Meadows, R. E.; Lapkin, A. A. Continuous Flow Buchwald–Hartwig Amination of a Pharmaceutical Intermediate. *React. Chem. Eng.* **2016**, *1* (2), 229–238.

(117) Amara, Z.; Poliakoff, M.; Duque, R.; Geier, D.; Franciò, G.; Gordon, C. M.; Meadows, R. E.; Woodward, R.; Leitner, W. Enabling the Scale-Up of a Key Asymmetric Hydrogenation Step in the Synthesis of an API Using Continuous Flow Solid-Supported Catalysis. *Org. Process Res. Dev.* **2016**, *20* (7), 1321–1327.

(118) Ott, D.; Borukhova, S.; Hessel, V. Life Cycle Assessment of Multi-Step Rufinamide Synthesis – from Isolated Reactions in Batch to Continuous Microreactor Networks. *Green Chem.* **2016**, *18* (4), 1096–1116.

(119) Niu, G.; Zhang, L.; Ruditskiy, A.; Wang, L.; Xia, Y. A Droplet-Reactor System Capable of Automation for the Continuous and Scalable Production of Noble-Metal Nanocrystals. *Nano Lett.* **2018**, *18* (6), 3879–3884.

(120) Lisiecki, K.; Czarnocki, Z. Flow Photochemistry as a Tool for the Total Synthesis of (+)-Epigalcatin. *Org. Lett.* **2018**, *20* (3), 605–607.

(121) Uekert, T.; Bajada, M. A.; Schubert, T.; Pichler, C. M.; Reisner, E. Scalable Photocatalyst Panels for Photoreforming of Plastic, Biomass and Mixed Waste in Flow. *ChemSusChem* **2021**, *14* (19), 4190–4197.

(122) Kuijpers, K. P. L.; van Dijk, M. A. H.; Rumeur, Q. G.; Hessel, V.; Su, Y.; Noël, T. A Sensitivity Analysis of a Numbered-up Photomicroreactor System. *React. Chem. Eng.* **2017**, *2* (2), 109–115.

(123) Saptal, V. B.; Ruta, V.; Bajada, M. A.; Vilé, G. Single-Atom Catalysis in Organic Synthesis. *Angew. Chem. Int. Ed.* **2023**, DOI: 10.1002/anie.202219306.

(124) Thomson, C. G.; Lee, A.-L.; Vilela, F. Heterogeneous Photocatalysis in Flow Chemical Reactors. *Beilstein J. Org. Chem.* **2020**, *16*, 1495–1549.

(125) Tsaoulidis, D.; Angeli, P. Effect of Channel Size on Mass Transfer during Liquid–Liquid Plug Flow in Small Scale Extractors. *Chem. Eng. J.* **2015**, *262*, 785–793.

(126) Chapman, M. R.; Kwan, M. H. T.; King, G.; Jolley, K. E.; Hussain, M.; Hussain, S.; Salama, I. E.; González Niño, C.; Thompson, L. A.; Bayana, M. E.; Clayton, A. D.; Nguyen, B. N.; Turner, N. J.; Kapur, N.; Blacker, A. J. Simple and Versatile Laboratory Scale CSTR for Multiphasic Continuous-Flow Chemistry and Long Residence Times. *Org. Process Res. Dev.* **2017**, *21* (9), 1294–1301.

(127) Mo, Y.; Jensen, K. F. A Miniature CSTR Cascade for Continuous Flow of Reactions Containing Solids. *React. Chem. Eng.* **2016**, *1* (5), 501–507.

(128) Savage, T.; Mitchell, J.; Trivedi, V.; Wicks, S.; Waters, L. J. Continuous Tank Reactor Synthesis of Highly Substituted Sulphobutylether β-Cyclodextrins. *Int. J. Pharm.* **2015**, *495* (2), 862–868.

(129) Yang, C.; Li, R.; Zhang, K. A. I.; Lin, W.; Landfester, K.; Wang, X. Heterogeneous Photoredox Flow Chemistry for the Scalable Organosynthesis of Fine Chemicals. *Nat. Commun.* **2020**, *11* (1), 1239.

(130) Hsu, W.-H.; Reischauer, S.; Seeberger, P. H.; Pieber, B.; Cambié, D. Heterogeneous Metallaphotoredox Catalysis in a Continuous-Flow Packed-Bed Reactor. *Beilstein J. Org. Chem.* **2022**, *18*, 1123–1130.

(131) Mazzanti, S.; Manfredi, G.; Barker, A. J.; Antonietti, M.; Savateev, A.; Giusto, P. Carbon Nitride Thin Films as All-In-One Technology for Photocatalysis. *ACS Catal.* **2021**, *11* (17), 11109–11116.

(132) Vilé, G.; Ng, D.; Xie, Z.; Martinez-Botella, I.; Tsanaktsidis, J.; Hornung, C. H. 3D-Printed Structured Reactor with Integrated Single-Atom Catalyst Film for Hydrogenation. *ChemCatChem* **2022**, *14* (14), e202101941.

(133) Li, Y.; Zhang, D.; Ye, J.; Mai, Y.; Wang, C.; Yang, Y.; Li, Y.; Besenbacher, F.; Niemantsverdriet, H.; Rosei, F.; Pan, F.; Su, R. A Modular Tubular Flow System with Replaceable Photocatalyst Membranes for Scalable Coupling and Hydrogenation. *Angew. Chem. Int. Ed.* **2023**, e202302979.

(134) Yadav, M. B.; Kulkarni, S.; Joshi, R. A.; Kulkarni, A. A. Continuous Flow Doebner–Miller Reaction and Isolation Using Continuous Stirred Tank Reactors. *Org. Process Res. Dev.* **2016**, *20* (9), 1621–1625.

(135) Loren, B. P.; Wleklinski, M.; Koswara, A.; Yammine, K.; Hu, Y.; Nagy, Z. K.; Thompson, D. H.; Cooks, R. G. Mass Spectrometric Directed System for the Continuous-Flow Synthesis and Purification of Diphenhydramine. *Chem. Sci.* **2017**, *8* (6), 4363–4370.

(136) Novo, P.; Janasek, D. Current Advances and Challenges in Microfluidic Free-Flow Electrophoresis—A Critical Review. *Anal. Chim. Acta* **2017**, *991*, 9–29.

(137) Grainger, R.; Heightman, T. D.; Ley, S. V.; Lima, F.; Johnson, C. N. Enabling Synthesis in Fragment-Based Drug Discovery by Reactivity Mapping: Photoredox-Mediated Cross-Dehydrogenative Heteroarylation of Cyclic Amines. *Chem. Sci.* **2019**, *10* (8), 2264–2271.

(138) Kenis, S.; D'hooghe, M.; Verniest, G.; Dang Thi, T. A.; Pham The, C.; Van Nguyen, T.; De Kimpe, N. Synthesis of 1-Alkyl-2-

(Trifluoromethyl)Azetidines and Their Regiospecific Ring Opening toward Diverse α-(Trifluoromethyl)Amines via Intermediate Azetidinium Salts. *J. Org. Chem.* **2012**, *77* (14), 5982–5992.

(139) Couty, F.; David, O.; Durrat, F.; Evano, G.; Lakhdar, S.; Marrot, J.; Vargas-Sanchez, M. Nucleophilic Ring-Opening of Azetidinium Ions: Insights into Regioselectivity. *Eur. J. Org. Chem.* **2006**, *2006* (15), 3479–3490.

(140) Drouillat, B.; D'Aboville, E.; Bourdreux, F.; Couty, F. Synthesis of 2-Phenyl- and 2,2-Diarylpyrrolidines through Stevens Rearrangement Performed on Azetidinium Ions. *Eur. J. Org. Chem.* **2014**, *2014* (5), 1103–1109.

(141) Börjesson, M.; Westman, G. Branching of Hemicelluloses through an Azetidinium Salt Ring-Opening Reaction. *Carbohydr. Res.* **2016**, *428*, 23–30.

(142) O'Brien, P.; Phillips, D. W.; Towers, T. D. An Azetidinium Ion Approach to 3-Aryloxy-3-Aryl-1-Propanamines. *Tetrahedron Lett.* **2002**, *43* (41), 7333–7335.

(143) Li, F.; Wang, Y. Methods and Compositions for the Synthesis of Multimerizing Agents. U.S. Patent 9024028, **2015**.

(144) Zheng, B.; Zhang, Y.; Zhang, Z.; Liu, L.; Chen, S.; Zhang, S. Azetidinium-Based Hypergolic Ionic Liquids with High Strain Energy. *ChemistrySelect* **2018**, *3* (1), 284–288.

(145) Bedore, M. W.; Zaborenko, N.; Jensen, K. F.; Jamison, T. F. Aminolysis of Epoxides in a Microreactor System: A Continuous Flow Approach to β-Amino Alcohols. *Org. Process Res. Dev.* **2010**, *14* (2), 432–440.

(146) Abaee, M. S.; Hamidi, V.; Mojtahedi, M. M. Ultrasound Promoted Aminolysis of Epoxides in Aqueous Media: A Rapid Procedure with No PH Adjustment for Additive-Free Synthesis of β-Aminoalcohols. *Ultrason. Sonochem.* **2008**, *15* (5), 823–827.

(147) Procopio, A.; Gaspari, M.; Nardi, M.; Oliverio, M.; Rosati, O. Highly Efficient and Versatile Chemoselective Addition of Amines to Epoxides in Water Catalyzed by Erbium(III) Triflate. *Tetrahedron Lett.* **2008**, *49* (14), 2289–2293.

(148) Chai, Y.; Xie, L.; Yu, Z.; Dai, W.; Wu, G.; Guan, N.; Li, L. Lead-Containing Beta Zeolites as Versatile Lewis Acid Catalysts for the

Aminolysis of Epoxides. *Microporous Mesoporous Mater.* **2018**, *264*, 230–239.

(149) Desai, H.; D'Souza, B.; Foether, D.; Johnson, B.; Lindsay, H. Regioselectivity in a Highly Efficient, Microwave-Assisted Epoxide Aminolysis. *Synthesis* **2007**, *2007* (6), 902–910.

(150) Maheswara, M.; Rao, K. S. V. K.; Do, J. Y. Regioselective Ring-Opening of Epoxides with Amines Using $Zn(ClO_4)_2$–Al_2O_3 as a Heterogeneous and Recyclable Catalyst. *Tetrahedron Lett.* **2008**, *49* (11), 1795–1800.

(151) Li, B.; Bader, S.; Guinness, S. M.; Ruggeri, S. G.; Hayward, C. M.; Hoagland, S.; Lucas, J.; Li, R.; Limburg, D.; McWilliams, J. C.; Raggon, J.; Van Alsten, J. Continuous Flow Aminolysis under High Temperature and Pressure. *J. Flow Chem.* **2020**, *10* (1), 145–156.

(152) Findrik Blažević, Z.; Milčić, N.; Sudar, M.; Majerić Elenkov, M. Halohydrin Dehalogenases and Their Potential in Industrial Application – A Viewpoint of Enzyme Reaction Engineering. *Adv. Synth. Catal.* **2021**, *363* (2), 388–410.

(153) González-Ugarte, A. S.; Hafez, I.; Tajvidi, M. Characterization and Properties of Hybrid Foams from Nanocellulose and Kaolin-Microfibrillated Cellulose Composite. *Sci. Rep.* **2020**, *10* (1), 17459.

(154) Khalil, A. M.; Hashem, T.; Gopalakrishnan, A.; Schäfer, A. I. Cyclodextrin Composite Nanofiber Membrane: Impact of the Crosslinker Type on Steroid Hormone Micropollutant Removal from Water. *ACS Appl. Polym. Mater.* **2021**, *3* (5), 2646–2656.

(155) Sagmeister, P.; Lebl, R.; Castillo, I.; Rehrl, J.; Kruisz, J.; Sipek, M.; Horn, M.; Sacher, S.; Cantillo, D.; Williams, J. D.; Kappe, C. O. Advanced Real-Time Process Analytics for Multistep Synthesis in Continuous Flow. *Angew. Chem. Int. Ed.* **2021**, *133* (15), 8220–8229.

(156) Yoshida, J.; Kim, H.; Nagaki, A. "Impossible" Chemistries Based on Flow and Micro. *J. Flow Chem.* **2017**, *7* (3–4), 60–64.

(157) Ruggeri, M.; Dombrowski, A. W.; Djuric, S. W.; Baxendale, I. R. Rearrangement of 3-Hydroxyazetidines into 2-Oxazolines. *J. Org. Chem.* **2020**, *85* (11), 7276–7286.

(158) Werner, M.; Kuratli, C.; Martin, R. E.; Hochstrasser, R.; Wechsler, D.; Enderle, T.; Alanine, A. I.; Vogel, H. Seamless Integration of Dose-Response Screening and Flow Chemistry: Efficient Generation of

Structure-Activity Relationship Data of β-Secretase (BACE1) Inhibitors. *Angew. Chem. Int. Ed.* **2014**, *53* (6), 1704–1708.

(159) Sivo, A.; Ruta, V.; Vilé, G. Gram-Scale Domino Synthesis in Batch and Flow Mode of Azetidinium Salts. *J. Org. Chem.* **2021**, *86* (20), 14113–14120.

(160) Tokar, A. V. The Quantum-Chemical Investigation of N-Cyclization Reaction Mechanism for Epichlorohydrin Aminolysis Products. *Bulletin of Dnipropetrovsk University* **2014**, *22*, 27– 30.

(161) Sheldon, R. A.; Norton, M. Green Chemistry and the Plastic Pollution Challenge: Towards a Circular Economy. *Green Chem.* **2020**, *22* (19), 6310–6322.

(162) Gade, S. M.; Saptal, V. B.; Bhanage, B. M. Perception of Glycerol Carbonate as Green Chemical: Synthesis and Applications. *Catal. Commun.* **2022**, *172*, 106542.

(163) Bell, B. M.; Briggs, J. R.; Campbell, R. M.; Chambers, S. M.; Gaarenstroom, P. D.; Hippler, J. G.; Hook, B. D.; Kearns, K.; Kenney, J. M.; Kruper, W. J.; Schreck, D. J.; Theriault, C. N.; Wolfe, C. P. Glycerin as a Renewable Feedstock for Epichlorohydrin Production. The GTE Process. CLEAN - Soil, Air, *Water* **2008**, *36* (8), 657–661.

(164) Liu, P. W.; Li, C. I.; Huang, K. C.; Liu, C. S.; Chen, H. L.; Lee, C. C.; Chiou, Y. Y.; Chen, R. J. 3-MCPD and Glycidol Coexposure Induces Systemic Toxicity and Synergistic Nephrotoxicity via NLRP3 Inflammasome Activation, Necroptosis, and Autophagic Cell Death. *J. Hazard. Mater.* **2021**, *405*, 124241.

(165) Craft, B. D.; Chiodini, A.; Garst, J.; Granvogl, M. Fatty Acid Esters of Monochloropropanediol (MCPD) and Glycidol in Refined Edible Oils. *Food Addit. Contam. Part A* **2013**, *30* (1), 46–51.

(166) Singh, G. S.; Mollet, K.; D'hooghe, M.; De Kimpe, N. Epihalohydrins in Organic Synthesis. *Chem. Rev.* **2013**, *113* (3), 1441–1498.

(167) Sonnati, M. O.; Amigoni, S.; Taffin de Givenchy, E. P.; Darmanin, T.; Choulet, O.; Guittard, F. Glycerol Carbonate as a Versatile Building Block for Tomorrow: Synthesis, Reactivity, Properties and Applications. *Green Chem.* **2013**, *15* (2), 283–306.

(168) Ricciardi, M.; Passarini, F.; Vassura, I.; Proto, A.; Capacchione, C.; Cucciniello, R.; Cespi, D. Glycidol, a Valuable Substrate for the Synthesis

of Monoalkyl Glyceryl Ethers: A Simplified Life Cycle Approach. *ChemSusChem* **2017**, *10* (10), 2291–2300.

(169) Seiwert, J.; Leibig, D.; Kemmer-Jonas, U.; Bauer, M.; Perevyazko, I.; Preis, J.; Frey, H. Hyperbranched Polyols via Copolymerization of 1,2-Butylene Oxide and Glycidol: Comparison of Batch Synthesis and Slow Monomer Addition. *Macromolecules* **2016**, *49* (1), 38–47.

(170) Della Monica, F.; Buonerba, A.; Grassi, A.; Capacchione, C.; Milione, S. Glycidol: An Hydroxyl-Containing Epoxide Playing the Double Role of Substrate and Catalyst for CO_2 Cycloaddition Reactions. *ChemSusChem* **2016**, *9* (24), 3457–3464.

(171) Villa, R.; Porcar, R.; Nieto, S.; Donaire, A.; Garcia-Verdugo, E.; Luis, S. V.; Lozano, P. Sustainable Chemo-Enzymatic Synthesis of Glycerol Carbonate (Meth)Acrylate from Glycidol and Carbon Dioxide Enabled by Ionic Liquid Technologies. *Green Chem.* **2021**, *23* (11), 4191–4200.

(172) Chiummiento, L.; Funicello, M.; Lupattelli, P.; Tramutola, F.; Campaner, P. New Indolic Non-Peptidic HIV Protease Inhibitors from (S)-Glycidol: Synthesis and Preliminary Biological Activity. *Tetrahedron* **2009**, *65* (31), 5984–5989.

(173) Hanson, R. M. The Synthetic Methodology of Nonracemic Glycidol and Related 2,3-Epoxy Alcohols. *Chem. Rev.* **1991**, *91* (4), 437–475.

(174) Zheng, Y.; Chen, X.; Shen, Y. Commodity Chemicals Derived from Glycerol, an Important Biorefinery Feedstock. *Chem. Rev.* **2008**, *108* (12) 5253-77.

(175) Alenezi, R.; Baig, M.; Wang, J.; Santos, R.; Leeke, G. A. Continuous Flow Hydrolysis of Sunflower Oil for Biodiesel. *Energy Sources A: Recovery Util. Environ. Eff.* **2010**, *32* (5), 460–468.

(176) Gade, S. M.; Munshi, M. K.; Chherawalla, B. M.; Rane, V. H.; Kelkar, A. A. Synthesis of Glycidol from Glycerol and Dimethyl Carbonate Using Ionic Liquid as a Catalyst. *Catal. Commun.* **2012**, *27*, 184–188.

(177) Kostyniuk, A.; Bajec, D.; Djinović, P.; Likozar, B. One-Step Synthesis of Glycidol from Glycerol in a Gas-Phase Packed-Bed Continuous Flow Reactor over HZSM-5 Zeolite Catalysts Modified by $CsNO_3$. *Chem. Eng. J.* **2020**, *394*, 124945.

(178) Dibenedetto, A.; Angelini, A.; Aresta, M.; Ethiraj, J.; Fragale, C.; Nocito, F. Converting Wastes into Added Value Products: From Glycerol to

Glycerol Carbonate, Glycidol and Epichlorohydrin Using Environmentally Friendly Synthetic Routes. *Tetrahedron* **2011**, *67* (6), 1308–1313.

(179) Choi, J. S.; Simanjuntaka, F. S. H.; Oh, J. Y.; Lee, K. I.; Lee, S. D.; Cheong, M.; Kim, H. S.; Lee, H. Ionic-Liquid-Catalyzed Decarboxylation of Glycerol Carbonate to Glycidol. *J. Catal.* **2013**, *297*, 248–255.

(180) Bolívar-Diaz, C. L.; Calvino-Casilda, V.; Rubio-Marcos, F.; Fernández, J. F.; Bañares, M. A. New Concepts for Process Intensification in the Conversion of Glycerol Carbonate to Glycidol. *Appl. Catal. B Environ.* **2013**, *129*, 575–579.

(181) Wu, P.; Tatsumi, T. A Novel Titanosilicate with MWW Structure: III. Highly Efficient and Selective Production of Glycidol through Epoxidation of Allyl Alcohol with H_2O_2. *J. Catal.* **2003**, *214* (2), 317–326.

(182) Simon, K.; Znidar, D.; Boutet, J.; Guillamot, G.; Lenoir, J.-Y.; Dallinger, D.; Kappe, C. O. Generation of 1,2-Difluorobenzene via a Photochemical Fluorodediazoniation Step in a Continuous Flow Mode. *Org. Process Res. Dev.* **2023**, *27* (2), 322–330.

(183) Sivo, A.; Ruta, V.; Granata, V.; Savateev, O.; Bajada, M. A.; Vilé, G. Nanostructured Carbon Nitride for Continuous-Flow Trifluoromethylation of (Hetero)Arenes. *ACS Sustain. Chem. Eng.* **2023**, *11* (13), 5284–5292.

(184) Kelly, C. B.; Mercadante, M. A.; Leadbeater, N. E. Trifluoromethyl Ketones: Properties, Preparation, and Application. *Chem. Commun.* **2013**, *49* (95), 11133.

(185) Besset, T.; Jubault, P.; Pannecoucke, X.; Poisson, T. New Entries toward the Synthesis of OCF_3-Containing Molecules. *Org. Chem. Front.* **2016**, *3* (8), 1004–1010.

(186) Hura, N.; Naaz, A.; Prassanawar, S. S.; Guchhait, S. K.; Panda, D. Drug-Clinical Agent Molecular Hybrid: Synthesis of Diaryl(Trifluoromethyl)Pyrazoles as Tubulin Targeting Anticancer Agents. *ACS Omega* **2018**, *3* (2), 1955–1969.

(187) Amini-Rentsch, L.; Vanoli, E.; Richard-Bildstein, S.; Marti, R.; Vilé, G. A Novel and Efficient Continuous-Flow Route To Prepare Trifluoromethylated N -Fused Heterocycles for Drug Discovery and Pharmaceutical Manufacturing. *Ind. Eng. Chem. Res.* **2019**, *58* (24), 10164–10171.

(188) Le, C.; Chen, T. Q.; Liang, T.; Zhang, P.; MacMillan, D. W. C. A Radical Approach to the Copper Oxidative Addition Problem: Trifluoromethylation of Bromoarenes. *Science* **2018**, *360*, 1010–1014.

(189) Straathof, N. J. W.; Cramer, S. E.; Hessel, V.; Noël, T. Practical Photocatalytic Trifluoromethylation and Hydrotrifluoromethylation of Styrenes in Batch and Flow. *Angew. Chem. Int. Ed.* **2016**, *55* (50), 15549–15553.

(190) Dubinina, G. G.; Furutachi, H.; Vicic, D. A. Active Trifluoromethylating Agents from Well-Defined Copper(I)−CF$_3$ Complexes. *J. Am. Chem. Soc.* **2008**, *130* (27), 8600–8601.

(191) Kremlev, M. M.; Mushta, A. I.; Tyrra, W.; Yagupolskii, Y. L.; Naumann, D.; Möller, A. Me$_3$SiCF$_3$/AgF/Cu—A New Reagents Combination for Selective Trifluoromethylation of Various Organic Halides by Trifluoromethylcopper, CuCF$_3$. *J. Fluor. Chem.* **2012**, *133*, 67–71.

(192) Wang, X.; Xu, Y.; Mo, F.; Ji, G.; Qiu, D.; Feng, J.; Ye, Y.; Zhang, S.; Zhang, Y.; Wang, J. Silver-Mediated Trifluoromethylation of Aryldiazonium Salts: Conversion of Amino Group into Trifluoromethyl Group. *J. Am. Chem. Soc.* **2013**, *135* (28), 10330–10333.

(193) Miyagawa, M.; Ishikawa, T.; Shinkai, K.; Akiyama, T. Ligand-Free Trifluoromethylation of Iodoarenes by Use of 2-Aryl-2-Trifluoromethylbenzimidazoline as New Trifluoromethylating Reagent. *J. Fluor. Chem.* **2019**, *219*, 29–31.

(194) Loy, R. N.; Sanford, M. S. Palladium-Catalyzed C–H Perfluoroalkylation of Arenes. *Org. Lett.* **2011**, *13* (10), 2548–2551.

(195) Vilé, G.; Sharma, P.; Nachtegaal, M.; Tollini, F.; Moscatelli, D.; Sroka-Bartnicka, A.; Tomanec, O.; Petr, M.; Filip, J.; Pieta, I. S.; Zbořil, R.; Gawande, M. B. An Earth-Abundant Ni-Based Single-Atom Catalyst for Selective Photodegradation of Pollutants. *Sol. RRL* **2021**, *5* (7), 2100176.

(196) Marzo, L.; Pagire, S. K.; Reiser, O.; König, B. Visible-Light Photocatalysis: Does It Make a Difference in Organic Synthesis? *Angew. Chem. Int. Ed.* **2018**, *57* (32), 10034–10072.

(197) Kumar, A.; Kumar, A.; Krishnan, V. Perovskite Oxide Based Materials for Energy and Environment-Oriented Photocatalysis. *ACS Catal.* **2020**, *10* (17), 10253–10315.

(198) Ismael, M. Structure, Properties, and Characterization of Mullite-Type Materials $Bi_2M_4O_9$ and Their Applications in Photocatalysis: A Review. *J. Environ. Chem. Eng.* **2022**, *10* (6), 108640.

(199) Ruffoni, A.; Juliá, F.; Svejstrup, T. D.; McMillan, A. J.; Douglas, J. J.; Leonori, D. Practical and Regioselective Amination of Arenes Using Alkyl Amines. *Nat. Chem.* **2019**, *11* (5), 426–433.

(200) Riente, P.; Fianchini, M.; Llanes, P.; Pericàs, M. A.; Noël, T. Shedding Light on the Nature of the Catalytically Active Species in Photocatalytic Reactions Using Bi_2O_3 Semiconductor. *Nat. Commun.* **2021**, *12* (1), 625.

(201) Seo, H.; Liu, A.; Jamison, T. F. Direct β-Selective Hydrocarboxylation of Styrenes with CO_2 Enabled by Continuous Flow Photoredox Catalysis. *J. Am. Chem. Soc.* **2017**, *139* (40), 13969–13972.

(202) Meanwell, M.; Lehmann, J.; Eichenberger, M.; Martin, R. E.; Britton, R. Synthesis of Acyl Fluorides via Photocatalytic Fluorination of Aldehydic C–H Bonds. *Chem. Commun.* **2018**, *54* (71), 9985–9988.

(203) Ruggeri, M.; Dombrowski, A. W.; Djuric, S. W.; Baxendale, I. R. Photochemical Flow Synthesis of 3-Hydroxyazetidines. *ChemPhotoChem* **2019**, *3* (12), 1212–1218.

(204) Xie, J.; Yuan, X.; Abdukader, A.; Zhu, C.; Ma, J. Visible-Light-Promoted Radical C–H Trifluoromethylation of Free Anilines. *Org. Lett.* **2014**, *16* (6), 1768–1771.

(205) Beatty, J. W.; Douglas, J. J.; Cole, K. P.; Stephenson, C. R. J. A Scalable and Operationally Simple Radical Trifluoromethylation. *Nat. Commun.* **2015**, *6* (1), 7919.

(206) Chang, B.; Shao, H.; Yan, P.; Qiu, W.; Weng, Z.; Yuan, R. Quinone-Mediated Trifluoromethylation of Arenes and Heteroarenes with Visible Light. *ACS Sustain. Chem. Eng.* **2017**, *5* (1), 334–341.

(207) Baar, M.; Blechert, S. Graphitic Carbon Nitride Polymer as a Recyclable Photoredox Catalyst for Fluoroalkylation of Arenes. *Chem. Eur. J.* **2015**, *21* (2), 526–530.

(208) Wang, L.; Liu, M.; Zha, W.; Wei, Y.; Ma, X.; Xu, C.; Lu, C.; Qin, N.; Gao, L.; Qiu, W.; Sa, R.; Fu, X.; Yuan, R. Mechanistic Study of Visible Light-Driven CdS or $g\text{-}C_3N_4$-Catalyzed C H Direct Trifluoromethylation of (Hetero)Arenes Using CF_3SO_2Na as the Trifluoromethyl Source. *J. Catal.* **2020**, *389*, 533–543.

(209) Pieber, B.; Malik, J. A.; Cavedon, C.; Gisbertz, S.; Savateev, A.; Cruz, D.; Heil, T.; Zhang, G.; Seeberger, P. H. Semi-heterogeneous Dual Nickel/Photocatalysis Using Carbon Nitrides: Esterification of Carboxylic Acids with Aryl Halides. *Angew. Chem. Int. Ed.* **2019**, *58* (28), 9575–9580.

(210) Huang, C.; Wen, Y.; Ma, J.; Dong, D.; Shen, Y.; Liu, S.; Ma, H.; Zhang, Y. Unraveling Fundamental Active Units in Carbon Nitride for Photocatalytic Oxidation Reactions. *Nat. Commun.* **2021**, *12* (1), 320.

(211) Ma, J.; Peng, X.; Zhou, Z.; Yang, H.; Wu, K.; Fang, Z.; Han, D.; Fang, Y.; Liu, S.; Shen, Y.; Zhang, Y. Extended Conjugation Tuning Carbon Nitride for Non-sacrificial H_2O_2 Photosynthesis and Hypoxic Tumor Therapy. *Angew. Chem. Int. Ed.* **2022**, *61* (43), e202210856.

(212) Liu, J.; Zou, Y.; Cruz, D.; Savateev, A.; Antonietti, M.; Vilé, G. Ligand–Metal Charge Transfer Induced via Adjustment of Textural Properties Controls the Performance of Single-Atom Catalysts during Photocatalytic Degradation. *ACS Appl. Mater. Interfaces* **2021**, *13* (22), 25858–25867.

(213) Lau, V. W.; Moudrakovski, I.; Botari, T.; Weinberger, S.; Mesch, M. B.; Duppel, V.; Senker, J.; Blum, V.; Lotsch, B. V. Rational Design of Carbon Nitride Photocatalysts by Identification of Cyanamide Defects as Catalytically Relevant Sites. *Nat. Commun.* **2016**, *7* (1), 12165.

(214) Wang, Y.; Wang, X.; Antonietti, M. Polymeric Graphitic Carbon Nitride as a Heterogeneous Organocatalyst: From Photochemistry to Multipurpose Catalysis to Sustainable Chemistry. *Angew. Chem. Int. Ed.* **2012**, *51* (1), 68–89.

(215) Nagib, D. A.; MacMillan, D. W. C. Trifluoromethylation of Arenes and Heteroarenes by Means of Photoredox Catalysis. *Nature* **2011**, *480* (7376), 224–228.

(216) Ruta, V.; Sivo, A.; Bonetti, L.; Bajada, M. A.; Vilé, G. Structural Effects of Metal Single-Atom Catalysts for Enhanced Photocatalytic Degradation of Gemfibrozil. *ACS Appl. Nano Mater.* **2022**, *5* (10), 14520–14528.

(217) Chen, Z.; Mitchell, S.; Vorobyeva, E.; Leary, R. K.; Hauert, R.; Furnival, T.; Ramasse, Q. M.; Thomas, J. M.; Midgley, P. A.; Dontsova, D.; Antonietti, M.; Pogodin, S.; López, N.; Pérez-Ramírez, J. Stabilization of Single Metal Atoms on Graphitic Carbon Nitride. *Adv. Funct. Mater.* **2017**, *27* (8), 1605785.

(218) Zhang, J.; Cai, W.; Hu, F. X.; Yang, H.; Liu, B. Recent Advances in Single Atom Catalysts for the Electrochemical Carbon Dioxide Reduction Reaction. *Chem. Sci.* **2021**, *12* (20), 6800–6819.

(219) Vilé, G.; Di Liberto, G.; Tosoni, S.; Sivo, A.; Ruta, V.; Nachtegaal, M.; Clark, A. H.; Agnoli, S.; Zou, Y.; Savateev, A.; Antonietti, M.; Pacchioni, G. Azide-Alkyne Click Chemistry over a Heterogeneous Copper-Based Single-Atom Catalyst. *ACS Catal.* **2022**, *12* (5), 2947–2958.

(220) Jiang, L.; Yuan, X.; Pan, Y.; Liang, J.; Zeng, G.; Wu, Z.; Wang, H. Doping of Graphitic Carbon Nitride for Photocatalysis: A Reveiw. *Appl. Catal. B Environ.* **2017**, *217*, 388–406.

(221) Pieber, B.; Shalom, M.; Antonietti, M.; Seeberger, P. H.; Gilmore, K. Continuous Heterogeneous Photocatalysis in Serial Micro-Batch Reactors. *Angew. Chem. Int. Ed.* **2018**, *57* (31), 9976–9979.

(222) Gu, H.; Liu, X.; Liu, X.; Ling, C.; Wei, K.; Zhan, G.; Guo, Y.; Zhang, L. Adjacent Single-Atom Irons Boosting Molecular Oxygen Activation on MnO_2. *Nat. Commun.* **2021**, *12* (1), 5422.

(223) Ferlin, F.; Lanari, D.; Vaccaro, L. Sustainable Flow Approaches to Active Pharmaceutical Ingredients. *Green Chem.* **2020**, *22* (18), 5937–5955.

(224) Espro, C.; Paone, E.; Mauriello, F.; Gotti, R.; Uliassi, E.; Bolognesi, M. L.; Rodríguez-Padrón, D.; Luque, R. Sustainable Production of Pharmaceutical, Nutraceutical and Bioactive Compounds from Biomass and Waste. *Chem. Soc. Rev.* **2021**, *50* (20), 11191–11207.

(225) Bao, X.; Li, H.; Wang, Z.; Tong, F.; Liu, M.; Zheng, Z.; Wang, P.; Cheng, H.; Liu, Y.; Dai, Y.; Fan, Y.; Li, Z.; Huang, B. TiO_2/Ti_3C_2 as an Efficient Photocatalyst for Selective Oxidation of Benzyl Alcohol to Benzaldehyde. *Appl. Catal. B Environ.* **2021**, *286*, 119885.

(226) Wang, Q.; Zhang, M.; Chen, C.; Ma, W.; Zhao, J. Photocatalytic Aerobic Oxidation of Alcohols on TiO_2: The Acceleration Effect of a Brønsted Acid. *Angew. Chem. Int. Ed.* **2010**, *49* (43), 7976–7979.

(227) Mallat, T.; Baiker, A. Oxidation of Alcohols with Molecular Oxygen on Solid Catalysts. *Chem. Rev.* **2004**, *104* (6), 3037–3058.

(228) Hao, H.; Zhang, L.; Wang, W.; Qiao, S.; Liu, X. Photocatalytic Hydrogen Evolution Coupled with Efficient Selective Benzaldehyde Production from Benzyl Alcohol Aqueous Solution over $ZnS-Ni_xS_y$ Composites. *ACS Sustain. Chem. Eng.* **2019**, *7* (12), 10501–10508.

(229) Krivtsov, I.; Vazirani, A.; Mitoraj, D.; Beranek, R. Benzaldehyde-Promoted (Auto)Photocatalysis under Visible Light: Pitfalls and Opportunities in Photocatalytic H_2O_2 Production. *ChemCatChem* **2023**, *15* (3), e202201215.

(230) ElMetwally, A. E.; Sayed, M. S.; Shim, J.-J.; Knecht, M. R.; Bachas, L. G. Plasmon-Enhanced Photocatalytic Oxidation of Benzyl Alcohol to Benzaldehyde Using $BiVO_4$/BiOBr/Au Nanosheets. *ACS Appl. Nano Mater.* **2023**, *6* (7), 5909–5917.

(231) Colmenares, J. C.; Ouyang, W.; Ojeda, M.; Kuna, E.; Chernyayeva, O.; Lisovytskiy, D.; De, S.; Luque, R.; Balu, A. M. Mild Ultrasound-Assisted Synthesis of TiO_2 Supported on Magnetic Nanocomposites for Selective Photo-Oxidation of Benzyl Alcohol. *Appl. Catal. B Environ.* **2016**, *183*, 107–112.

(232) Villa, A.; Ferri, D.; Campisi, S.; Chan-Thaw, C. E.; Lu, Y.; Kröcher, O.; Prati, L. Operando Attenuated Total Reflectance FTIR Spectroscopy: Studies on the Different Selectivity Observed in Benzyl Alcohol Oxidation. *ChemCatChem* **2015**, *7* (16), 2534–2541.

(233) Tiburcio, E.; Greco, R.; Mon, M.; Ballesteros-Soberanas, J.; Ferrando-Soria, J.; López-Haro, M.; Hernández-Garrido, J. C.; Oliver-Meseguer, J.; Marini, C.; Boronat, M.; Armentano, D.; Leyva-Pérez, A.; Pardo, E. Soluble/MOF-Supported Palladium Single Atoms Catalyze the Ligand-, Additive-, and Solvent-Free Aerobic Oxidation of Benzyl Alcohols to Benzoic Acids. *J. Am. Chem. Soc.* **2021**, *143* (6), 2581–2592.

(234) Huang, K.; Fu, H.; Shi, W.; Wang, H.; Cao, Y.; Yang, G.; Peng, F.; Wang, Q.; Liu, Z.; Zhang, B.; Yu, H. Competitive Adsorption on Single-Atom Catalysts: Mechanistic Insights into the Aerobic Oxidation of Alcohols over Co N C. *J. Catal.* **2019**, *377*, 283–292.

(235) Sun, N.; Song, J.; Tao, Q.; Kan, E.; Kuai, L. High-Loading Single-Atom Pt/TiO_2 Mesoporous Catalysts for Superior Photocatalytic Oxidation of Benzyl Alcohol. Microporous Mesoporous Mater. **2022**, *337*, 111949.

(236) Vilé, G. Photocatalytic Materials and Light-Driven Continuous Processes to Remove Emerging Pharmaceutical Pollutants from Water and Selectively Close the Carbon Cycle. *Catal. Sci. Technol.* **2021**, *11* (1), 43–61.

(237) Huang, H.; Zhou, C.; Jiao, X.; Yuan, H.; Zhao, J.; He, C.; Hofkens, J.; Roeffaers, M. B. J.; Long, J.; Steele, J. A. Subsurface Defect Engineering

in Single-Unit-Cell Bi_2WO_6 Monolayers Boosts Solar-Driven Photocatalytic Performance. *ACS Catal.* **2020**, *10* (2), 1439–1443.

(238) Debruyne, M.; Van Speybroeck, V.; Van Der Voort, P.; Stevens, C. V. Porous Organic Polymers as Metal Free Heterogeneous Organocatalysts. *Green Chem.* **2021**, *23* (19), 7361–7434.

(239) Krishnaraj, C.; Sekhar Jena, H.; Bourda, L.; Laemont, A.; Pachfule, P.; Roeser, J.; Chandran, C. V.; Borgmans, S.; Rogge, S. M. J.; Leus, K.; Stevens, C. V.; Martens, J. A.; Van Speybroeck, V.; Breynaert, E.; Thomas, A.; Van Der Voort, P. Strongly Reducing (Diarylamino)Benzene-Based Covalent Organic Framework for Metal-Free Visible Light Photocatalytic H_2O_2 Generation. *J. Am. Chem. Soc.* **2020**, *142* (47), 20107–20116.

(240) Kresse, G.; Furthmüller, J. Efficiency of Ab-Initio Total Energy Calculations for Metals and Semiconductors Using a Plane-Wave Basis Set. *Comput. Mater. Sci.* **1996**, *6* (1), 15–50.

(241) Perdew, J. P.; Burke, K.; Ernzerhof, M. Generalized Gradient Approximation Made Simple. *Phys. Rev. Lett.* **1996**, *77* (18), 3865–3868.

(242) Grimme, S.; Antony, J.; Ehrlich, S.; Krieg, H. A Consistent and Accurate Ab Initio Parametrization of Density Functional Dispersion Correction (DFT-D) for the 94 Elements H-Pu. *J. Chem. Phys.* **2010**, *132* (15), 154104.

(243) Kresse, G.; Joubert, D. From Ultrasoft Pseudopotentials to the Projector Augmented-Wave Method. *Phys. Rev. B* **1999**, *59* (3), 1758–1775.

(244) Barlocco, I.; Cipriano, L. A.; Di Liberto, G.; Pacchioni, G. Does the Oxygen Evolution Reaction Follow the Classical OH*, O*, OOH* Path on Single Atom Catalysts? *J. Catal.* **2023**, *417*, 351–359.

(245) Di Liberto, G.; Cipriano, L. A.; Pacchioni, G. Single Atom Catalysts: What Matters Most, the Active Site or The Surrounding? *ChemCatChem* **2022**, *14* (19), e202200611.

(246) Nørskov, J. K.; Christensen, C. H. Toward Efficient Hydrogen Production at Surfaces. *Science* **2006**, *312*, 1322–1323.

(247) Nørskov, J. K.; Bligaard, T.; Rossmeisl, J.; Christensen, C. H. Towards the Computational Design of Solid Catalysts. *Nat. Chem.* **2009**, *1* (1), 37–46.

(248) Fina, F.; Callear, S. K.; Carins, G. M.; Irvine, J. T. S. Structural Investigation of Graphitic Carbon Nitride via XRD and Neutron Diffraction. *Chem. Mater.* **2015**, *27* (7), 2612–2618.

(249) Camp, J. E. Bio-Available Solvent Cyrene: Synthesis, Derivatization, and Applications. *ChemSusChem* **2018**, *11* (18), 3048–3055.

(250) Sherwood, J.; De bruyn, M.; Constantinou, A.; Moity, L.; McElroy, C. R.; Farmer, T. J.; Duncan, T.; Raverty, W.; Hunt, A. J.; Clark, J. H. Dihydrolevoglucosenone (Cyrene) as a Bio-Based Alternative for Dipolar Aprotic Solvents. *Chem. Commun.* **2014**, *50* (68), 9650–9652.

(251) Carless, J. E.; Swarbrick, J. The Solubility of Benzaldehyde in Water as Determined by Refractive Index Measurements. *J. Pharm. Pharmacol.* **2011**, *16* (9), 633–634.

(252) Wang, H.; Guo, L.-N.; Duan, X.-H. Silver-Catalyzed Oxidative Coupling/Cyclization of Acrylamides with 1,3-Dicarbonyl Compounds. *Chem. Commun.* **2013**, *49* (88), 10370–10372.

(253) Hua, H.-L.; Zhang, B.-S.; He, Y.-T.; Qiu, Y.-F.; Wu, X.-X.; Xu, P.-F.; Liang, Y.-M. Silver-Catalyzed Oxidative Cyclization of Propargylamide-Substituted Indoles: Synthesis of Phosphorated Indoloazepinones Derivatives. *Org. Lett.* **2016**, *18* (2), 216–219.

(254) Brady, B.; Steenhof, V.; Nickel, B.; Blackburn, A. M.; Vehse, M.; Brolo, A. G. Plasmonic Light-Trapping Concept for Nanoabsorber Photovoltaics. *ACS Appl. Energy Mater.* **2019**, *2* (3), 2255–2262.

(255) Luo, H.; Barrio, J.; Sunny, N.; Li, A.; Steier, L.; Shah, N.; Stephens, I. E. L.; Titirici, M. Progress and Perspectives in Photo- and Electrochemical-Oxidation of Biomass for Sustainable Chemicals and Hydrogen Production. *Adv. Energy Mater.* **2021**, *11* (43), 2101180.

(256) Tan, H. L.; Abdi, F. F.; Ng, Y. H. Heterogeneous Photocatalysts: An Overview of Classic and Modern Approaches for Optical, Electronic, and Charge Dynamics Evaluation. *Chem. Soc. Rev.* **2019**, *48* (5), 1255–1271.

(257) Colmenares, J. C.; Luque, R. Heterogeneous Photocatalytic Nanomaterials: Prospects and Challenges in Selective Transformations of Biomass-Derived Compounds. *Chem. Soc. Rev.* **2014**, *43* (3), 765–778.

(258) Ciriminna, R.; Delisi, R.; Xu, Y.-J.; Pagliaro, M. Toward the Waste-Free Synthesis of Fine Chemicals with Visible Light. *Org. Process Res. Dev.* **2016**, *20* (2), 403–408.

(259) Cui, X.; Li, W.; Ryabchuk, P.; Junge, K.; Beller, M. Bridging Homogeneous and Heterogeneous Catalysis by Heterogeneous Single-Metal-Site Catalysts. *Nat. Catal.* **2018**, *1* (6), 385–397.

(260) Wang, X.; Blechert, S.; Antonietti, M. Polymeric Graphitic Carbon Nitride for Heterogeneous Photocatalysis. *ACS Catal.* **2012**, *2* (8), 1596–1606.

(261) Lovato, K.; Fier, P. S.; Maloney, K. M. The Application of Modern Reactions in Large-Scale Synthesis. *Nat. Rev. Chem.* **2021**, *5* (8), 546–563.

(262) Tanimu, A.; Jaenicke, S.; Alhooshani, K. Heterogeneous Catalysis in Continuous Flow Microreactors: A Review of Methods and Applications. *Chem. Eng. J.* **2017**, *327*, 792–821.

(263) Kolb, G.; Hessel, V. Micro-Structured Reactors for Gas Phase Reactions. *Chem. Eng. J.* **2004**, *98* (1–2), 1–38.

(264) Dudukovic, M. P. Frontiers in Reactor Engineering. *Science* **2009**, *325* (5941), 698–701.

(265) Zhang, H.; Liu, Y.; Liu, N.; Kang, S. Understanding the Interface Properties of Photocatalytic Reactors for Rational Engineering Applications. *Chem. Eng. J.* **2023**, *472*, 145057.

(266) Udepurkar, A. P.; Nandiwale, K. Y.; Jensen, K. F.; Kuhn, S. Heterogeneous Photochemical Reaction Enabled by an Ultrasonic Microreactor. *React. Chem. Eng.* **2023**, *8* (8), 1930–1936.

(267) Tian, J.; Zhang, Y.; Du, L.; He, Y.; Jin, X.-H.; Pearce, S.; Eloi, J.-C.; Harniman, R. L.; Alibhai, D.; Ye, R.; Phillips, D. L.; Manners, I. Tailored Self-Assembled Photocatalytic Nanofibres for Visible-Light-Driven Hydrogen Production. *Nat. Chem.* **2020**, *12* (12), 1150–1156.

(268) Chaudhuri, A.; Kuijpers, K. P. L.; Hendrix, R. B. J.; Shivaprasad, P.; Hacking, J. A.; Emanuelsson, E. A. C.; Noël, T.; van der Schaaf, J. Process Intensification of a Photochemical Oxidation Reaction Using a Rotor-Stator Spinning Disk Reactor: A Strategy for Scale Up. *Chem. Eng. J.* **2020**, *400*, 125875.

(269) Hu, H.; Wang, Z.; Cao, L.; Zeng, L.; Zhang, C.; Lin, W.; Wang, C. Metal–Organic Frameworks Embedded in a Liposome Facilitate Overall Photocatalytic Water Splitting. *Nat. Chem.* **2021**, *13* (4), 358–366.

(270) Khan, M. A.; Sprockel, A. J.; Macmillan, K. A.; Alting, M. T.; Kharal, S. P.; Boakye-Ansah, S.; Haase, M. F. Nanostructured, Fluid-Bicontinuous Gels for Continuous-Flow Liquid–Liquid Extraction. *Adv. Mater.* **2022**, *34*

(18), 2109547.

(271) Haase, M. F.; Jeon, H.; Hough, N.; Kim, J. H.; Stebe, K. J.; Lee, D. Multifunctional Nanocomposite Hollow Fiber Membranes by Solvent Transfer Induced Phase Separation. *Nat. Commun.* **2017**, *8* (1), 1234.

(272) Tavacoli, J. W.; Thijssen, J. H. J.; Schofield, A. B.; Clegg, P. S. Novel, Robust, and Versatile Bijels of Nitromethane, Ethanediol, and Colloidal Silica: Capsules, Sub-Ten-Micrometer Domains, and Mechanical Properties. *Adv. Funct. Mater.* **2011**, *21* (11), 2020–2027.

(273) Lee, M. N.; Mohraz, A. Hierarchically Porous Silver Monoliths from Colloidal Bicontinuous Interfacially Jammed Emulsion Gels. *J. Am. Chem. Soc.* **2011**, *133* (18), 6945–6947.

(274) Huang, C.; Forth, J.; Wang, W.; Hong, K.; Smith, G. S.; Helms, B. A.; Russell, T. P. Bicontinuous Structured Liquids with Sub-Micrometre Domains Using Nanoparticle Surfactants. *Nat. Nanotechnol.* **2017**, *12* (11), 1060–1063.

(275) Wu, D. H.; Chen, A. D.; Johnson, C. S. An Improved Diffusion-Ordered Spectroscopy Experiment Incorporating Bipolar-Gradient Pulses. *J. Magn. Reson. Ser. A* **1995**, *115* (2), 260–264.

(276) Bajada, M. A.; Di Liberto, G.; Tosoni, S.; Ruta, V.; Mino, L.; Allasia, N.; Sivo, A.; Pacchioni, G.; Vilé, G. Light-Driven C–O Coupling of Carboxylic Acids and Alkyl Halides over a Ni Single-Atom Catalyst. *Nat. Synth.* **2023**, DOI: 10.1038/s44160-023-00341-3.

(277) Hu, Y.; Shim, Y.; Oh, J.; Park, S.; Park, S.; Ishii, Y. Synthesis of 13 C-, 15 N-Labeled Graphitic Carbon Nitrides and NMR-Based Evidence of Hydrogen-Bonding Assisted Two-Dimensional Assembly. *Chem. Mater.* **2017**, *29* (12), 5080–5089.

(278) Pepels, M. P. F.; Hansen, M. R.; Goossens, H.; Duchateau, R. From Polyethylene to Polyester: Influence of Ester Groups on the Physical Properties. *Macromolecules* **2013**, *46* (19), 7668–7677.

(279) Xiang, Q.; Yu, J.; Jaroniec, M. Preparation and Enhanced Visible-Light Photocatalytic H_2 -Production Activity of Graphene/C_3N_4 Composites. *J. Phys. Chem. C* **2011**, *115* (15), 7355–7363.

(280) Groves, P. Diffusion Ordered Spectroscopy (DOSY) as Applied to Polymers. *Polym. Chem.* **2017**, *8* (44), 6700–6708.

(281) Holz, M.; Heil, S. R.; Sacco, A. Temperature-Dependent Self-Diffusion

Coefficients of Water and Six Selected Molecular Liquids for Calibration in Accurate ^{1}H NMR PFG Measurements. *Phys. Chem. Chem. Phys.* **2000**, *2* (20), 4740–4742.

(282) Casado, C.; Marugán, J.; Timmers, R.; Muñoz, M.; van Grieken, R. Comprehensive Multiphysics Modeling of Photocatalytic Processes by Computational Fluid Dynamics Based on Intrinsic Kinetic Parameters Determined in a Differential Photoreactor. *Chem. Eng. J.* **2017**, *310*, 368–380.

(283) Mo, Y.; Rughoobur, G.; Nambiar, A. M. K.; Zhang, K.; Jensen, K. F. A Multifunctional Microfluidic Platform for High-Throughput Experimentation of Electroorganic Chemistry. *Angew. Chem. Int. Ed.* **2020**, *132* (47), 21076–21080.

(284) Ley, S. V. The Engineering of Chemical Synthesis: Humans and Machines Working in Harmony. *Angew. Chemie Int. Ed.* **2018**, *57* (19), 5182–5183.

(285) Wan, T.; Capaldo, L.; Laudadio, G.; Nyuchev, A. V.; Rincón, J. A.; García-Losada, P.; Mateos, C.; Frederick, M. O.; Nuño, M.; Noël, T. Decatungstate-Mediated C(Sp3)–H Heteroarylation via Radical-Polar Crossover in Batch and Flow. *Angew. Chem. Int. Ed.* **2021**, *133* (33), 18037–18041.

(286) Musci, P.; Keutz, T.; Belaj, F.; Degennaro, L.; Cantillo, D.; Kappe, C. O.; Luisi, R. Flow Technology for Telescoped Generation, Lithiation and Electrophilic (C3) Functionalization of Highly Strained 1-Azabicyclo[1.1.0]Butanes. *Angew. Chem. Int. Ed.* **2021**, *133* (12), 6465–6469.

(287) Lovato, K.; Fier, P. S.; Maloney, K. M. The Application of Modern Reactions in Large-Scale Synthesis. *Nat. Rev. Chem.* **2021**, *5* (8), 546–563.

(288) Kearnes, S. M.; Maser, M. R.; Wleklinski, M.; Kast, A.; Doyle, A. G.; Dreher, S. D.; Hawkins, J. M.; Jensen, K. F.; Coley, C. W. The Open Reaction Database. *J. Am. Chem. Soc.* **2021**, *143* (45), 18820–18826.

(289) Davies, I. W. The Digitization of Organic Synthesis. *Nature* **2019**, *570* (7760), 175–181.

(290) Imbrogno, J.; Rogers, L.; Thomas, D. A.; Jensen, K. F. Continuous Purification of Active Pharmaceutical Ingredients Utilizing Polymer Membrane Surface Wettability. *Chem. Commun.* **2018**, *54* (1), 70–73.

(291) Weeranoppanant, N.; Adamo, A. In-Line Purification: A Key Component to Facilitate Drug Synthesis and Process Development in Medicinal Chemistry. *ACS Med. Chem. Lett.* **2020**, *11* (1), 9–15.

(292) Doyle, B. J.; Elsner, P.; Gutmann, B.; Hannaerts, O.; Aellig, C.; Macchi, A.; Roberge, D. M. Mini-Monoplant Technology for Pharmaceutical Manufacturing. *Org. Process Res. Dev.* **2020**, *24* (10), 2169–2182.

(293) Testa, C. J.; Shvedova, K.; Hu, C.; Wu, W.; Born, S. C.; Takizawa, B.; Mascia, S. Heterogeneous Crystallization as a Process Intensification Technology in an Integrated Continuous Manufacturing Process for Pharmaceuticals. *Org. Process Res. Dev.* **2021**, *25* (2), 225–238.

(294) O'Brien, A. G.; Horváth, Z.; Lévesque, F.; Lee, J. W.; Seidel-Morgenstern, A.; Seeberger, P. H. Continuous Synthesis and Purification by Direct Coupling of a Flow Reactor with Simulated Moving-Bed Chromatography. *Angew. Chem. Int. Ed.* **2012**, *51* (28), 7028–7030.

(295) Örkényi, R.; Éles, J.; Faigl, F.; Vincze, P.; Prechl, A.; Szakács, Z.; Kóti, J.; Greiner, I. Continuous Synthesis and Purification by Coupling a Multistep Flow Reaction with Centrifugal Partition Chromatography. *Angew. Chem. Int. Ed.* **2017**, *56* (30), 8742–8745.

(296) Fitzpatrick, D. E.; Mutton, R. J.; Ley, S. V. In-Line Separation of Multicomponent Reaction Mixtures Using a New Semi-Continuous Supercritical Fluid Chromatography System. *React. Chem. Eng.* **2018**, *3* (5), 799–806.

(297) Thomson, C. G.; Banks, C.; Allen, M.; Barker, G.; Coxon, C. R.; Lee, A.-L.; Vilela, F. Expanding the Tool Kit of Automated Flow Synthesis: Development of In-Line Flash Chromatography Purification. *J. Org. Chem.* **2021**, *86* (20), 14079–14094.

(298) Sivo, A.; Kim, T. K.; Ruta, V.; Luisi, R.; Osorio-Tejada, J.; Escriba-Gelonch, M.; Hessel, V.; Sponchioni, M.; Vilé, G. Enhanced Flow Synthesis of Small Molecules by In-Line Integration of Sequential Catalysis and Benchtop Twin-Column Continuous Chromatography. *React. Chem. Eng.* **2022**, *7* (12), 2650–2658.

(299) Feidl, F.; Vogg, S.; Wolf, M.; Podobnik, M.; Ruggeri, C.; Ulmer, N.; Wälchli, R.; Souquet, J.; Broly, H.; Butté, A.; Morbidelli, M. Process-wide Control and Automation of an Integrated Continuous Manufacturing Platform for Antibodies. *Biotechnol. Bioeng.* **2020**, *117* (5), 1367–1380.

(300) Karst, D. J.; Steinebach, F.; Morbidelli, M. Continuous Integrated Manufacturing of Therapeutic Proteins. *Curr. Opin. Biotechnol.* **2018**, *53*, 76–84.

(301) Environmental Management — Life Cycle Assessment — Principles and Framework, Https://Www.Iso.Org/Standard/37456.Html, 2006.

(302) ReCiPe 2016 v1.1 Endpoint Method, Hierarchist Version.

(303) Huijbregts, M. A. J.; Steinmann, Z. J. N.; Elshout, P. M. F.; Stam, G.; Verones, F.; Vieira, M.; Zijp, M.; Hollander, A.; van Zelm, R. ReCiPe2016: A Harmonised Life Cycle Impact Assessment Method at Midpoint and Endpoint Level. Int. J. *Life Cycle Assess* **2017**, *22* (2), 138–147.

(304) Ecoinvent LCA Database, Https://Ecoinvent.Org/, 2022.

(305) B. S. Furniss, A. J. Hannaford, P. W. G. S. and A. R. T. Vogel's Textbook of Practical Organic Chemistry, 5th ed.; Technical, L. S. &, Ed.; London, 1989.

(306) Osorio-Tejada, J.; Ferlin, F.; Vaccaro, L.; Hessel, V. Life Cycle Assessment of Multistep Benzoxazole Synthesis: From Batch to Waste-Minimised Continuous Flow Systems. *Green Chem.* **2022**, *24* (1), 325–337.

(307) Hischier, R.; Hellweg, S.; Capello, C.; Primas, A. Establishing Life Cycle Inventories of Chemicals Based on Differing Data Availability (9 Pp). *Int. J. Life Cycle Assess* **2005**, *10* (1), 59–67.

(308) PRé Consultants, Https://Pre-Sustainability.Com/Solutions/Tools/Simapro/ 2022.

(309) Frischknecht, R.; Jungbluth, N.; Althaus, H.-J.; Hischier, R.; Doka, G.; Bauer, C.; Dones, R.; Wernet, G.; Nemecek, T.; Primas, A. Code of Practice. Data v2.0. Ecoinvent Report No. 2, 2007.

(310) The Ellen MacArthur Foundation Circularity Indicators, Https://Ellenmacarthurfoundation.Org/Resources/Circulytics/Overview (Accessed August 2022).

(311) Simoens, A.; Scattolin, T.; Cauwenbergh, T.; Pisanò, G.; Cazin, C. S. J.; Stevens, C. V.; Nolan, S. P. Continuous Flow Synthesis of Metal–NHC Complexes. *Chem. Eur. J.* **2021**, *27* (18), 5653–5657.

(312) Govaerts, S.; Nyuchev, A.; Noel, T. Pushing the Boundaries of C–H Bond Functionalization Chemistry Using Flow Technology. *J. Flow Chem.* **2020**, *10* (1), 13–71.

(313) Noël, T.; Buchwald, S. L. Cross-Coupling in Flow. *Chem. Soc. Rev.* **2011**, *40* (10), 5010.

(314) Shahbazali, E.; Billaud, E. M. F.; Fard, A. S.; Meuldijk, J.; Bormans, G.; Noel, T.; Hessel, V. Photo Isomerization of Cis -cyclooctene to Trans -cyclooctene: Integration of a Micro-flow Reactor and Separation by Specific Adsorption. *Angew. Chem. Int. Ed.* **2021**, *67* (1), e17067.

(315) Angarita, M.; Müller-Späth, T.; Baur, D.; Lievrouw, R.; Lissens, G.; Morbidelli, M. Twin-Column CaptureSMB: A Novel Cyclic Process for Protein A. *J. Chromatogr. A* **2015**, *1389*, 85–95.

(316) Kim, T. K.; Botti, C.; Angelo, J.; Xu, X.; Ghose, S.; Li, Z. J.; Morbidelli, M.; Sponchioni, M. Experimental Design of the Multicolumn Countercurrent Solvent Gradient Purification (MCSGP) Unit for the Separation of PEGylated Proteins. *Ind. Eng. Chem. Res.* **2021**, *60* (29), 10764–10776.

(317) Escribà-Gelonch, M.; de Leon Izeppi, G. A.; Kirschneck, D.; Hessel, V. Multistep Solvent-Free 3 m 2 Footprint Pilot Miniplant for the Synthesis of Annual Half-Ton Rufinamide Precursor. *ACS Sustain. Chem. Eng.* **2019**, *7* (20), 17237–17251.

Appendix A

Annexes

Chapter 2

Table A.2.1. *Vis-à-vis comparison between batch and flow data.*

Entry	Solvent	T (°C)	t (min)	Batch yield (%)[a,b]	Flow yield (%)[a,c]
1	EtOH	25	60	2	0
2	EtOH	60	60	30	63
3	EtOH	80	60	51	66

[a]Calculated by NMR, using dibromomethane as internal standard. [b]Carried out following the 'General procedure for batch synthesis of 3-hydroxyazetidinium chloride' detailed in the experimental section of the manuscript. [c]Carried out following the 'General procedure for the continuous-flow synthesis of 3-hydroxyazetidinium chloride' detailed in the experimental section of the manuscript.

A.2.2. Compounds Characterization

1,1-Diethyl-3-hydroxyazetidin-1-ium (4)

Colorless oil (66%, 3.0 g); ^{1}H NMR (400 MHz, DMSO-d_6) δ 6.65 (d, J = 7.0 Hz, 1H), 4.66–4.57 (m, 1H), 4.44 (dd, J = 12.0, 7.2 Hz, 2H), 4.12 (dd, J = 12.0, 7.2 Hz, 2H), 3.52–3.47 (q, J = 7.2 Hz, 2H), 3.38–3.33 (q, J = 7.2 Hz, 3H), 1.12 (t, J = 7.2 Hz, 6H); ^{13}C NMR (101 MHz, DMSO-d6) δ 70.3, 56.0, 55.8, 53.9, 23.6, 8.3, 7.9; HRMS (ESI-QIT) m/z calcd for $C_7H_{16}NO^+$ $[M]^+$ 130.1226, found 130.2485.

1,1-Dibutyl-3-hydroxyazetidin-1-ium (5)

Colorless oil (29%, 0.7 g); ^{1}H NMR (400 MHz, CDCl₃) δ 6.85 (s, 1H), 4.89–4.86 (m, 1H), 4.59 (dd, J = 11.6, 7.1 Hz, 2H), 4.39 (dd, J = 11.6, 7.1 Hz, 2H), 2.52–2.34 (m, 4H), 1.28–1.10 (m, 8H), 0.85 (t, J = 7.2 Hz, 6H); ^{13}C NMR (101 MHz, CDCl₃) δ 70.6, 54.1, 29.3, 20.5, 14.0; HRMS (ESI-QIT) m/z calcd for $C_{11}H_{24}NO^+$ $[M]^+$ 186.1852, found 186.2336.

3-Hydroxy-1,1-diisopropylazetidin-1-ium (6)

Colorless oil (66%, 2.5 g); ^{1}H NMR (400 MHz, D₂O) δ 4.64 (dd, J = 13.5, 6.4 Hz, 1H), 4.35 (dd, J = 13.9, 7.5 Hz, 2H), 4.15 (dd, J = 13.9, 6.0 Hz, 2H), 3.80 (dtt, J = 12.9, 6.5, 3.1 Hz, 2H), 1.38 (t, J = 6.6 Hz, 12H); ^{13}C NMR (101 MHz, D₂O) δ 61.14, 60.93, 60.08, 57.43, 16.24; HRMS (ESI-QIT) m/z calcd for $C_9H_{20}NO^+$ $[M]^+$ 158.1539, found 158.2225.

2-Hydroxy-4-azaspiro[3.4]octan-4-ium (7)

Colorless oil (49%, 3.5 g); ^{1}H NMR (400 MHz, DMSO-d_6) δ 6.62 (s, 1H), 4.65–4.6 (m, 1H), 4.50 (dd, J = 11.6, 6.9 Hz, 2H), 4.24 (dd, J = 11.6, 5.7 Hz, 2H), 3.68–3.64 (m, 2H), 3.61–3.55 (m, 2H), 1.97–1.93 (m, 4H); ^{13}C NMR (101 MHz, DMSO-d_6) δ 71.27, 64.41, 62.98, 21.51, 21.29; HRMS (ESI-QIT) m/z calcd for $C_7H_{14}NO^+$ $[M]^+$ 128.1070, found 128.2299.

2-Hydroxy-4-azaspiro[3.5]nonan-4-ium (8)

Yellow oil (75%, 3.0 g); ^{1}H NMR (400 MHz, DMSO-d_6) δ 6.61 (d, J = 6.7 Hz, 1H), 4.69–4.57 (m, 1H), 4.50–4.38 (m, 2H), 4.10 (dd, J = 11.9, 5.5 Hz, 2H), 3.54 (dd, J = 11.2, 5.7 Hz, 3H), 3.39 (dd, J = 17.9, 12.2 Hz, 3H), 2.67–2.33 (m, J = 45.7, 25.3, 21.0 Hz, 6H), 1.72–1.63 (m, J = 9.9, 5.1 Hz, 4H), 1.59–1.51 (m, 3H), 1.46–1.32 (m, 4H); ^{13}C NMR (101 MHz, DMSO-d_6) δ 70.98, 62.16, 60.40, 58.25, 54.65, 25.19; HRMS (ESI-QIT) m/z calcd for $C_8H_{16}NO^+$ $[M]^+$ 142.1226, found 142.2198.

2-Hydroxy-7-oxa-4-azaspiro[3.5]nonan-4-ium (9)

Orange oil (28%, 1.4 g); ^{1}H NMR (400 MHz, DMSO-d_6) δ 6.65 (s, 1H), 4.70–4.63 (m, 1H), 4.58 (dd, J = 11.9, 6.6 Hz, 2H), 4.24 (dd, J = 11.6, 5.2 Hz, 2H), 3.93–3.85 (m, 2H), 3.79 (dd, J = 9.2, 3.6 Hz, 4H), 3.64 (dd, J = 9.3, 4.5 Hz, 13H), 3.58 (dd, J = 7.7, 3.2 Hz, 8H), 3.54 (t, J = 4.8 Hz, 3H), 2.79–2.54 (m, 12H), 2.44 (ddd, J = 19.1, 9.9, 4.0 Hz, 13H); ^{13}C NMR (101 MHz, DMSO-d_6) δ 61.85, 60.82, 58.29, 54.24, 53.76; HRMS (ESI-QIT) m/z calcd for $C_7H_{14}NO_2^+$ [M]$^+$ 144.1019, found 144.1926.

1-Chloro-3-[methyl(phenyl)amino]propan-2-ol (11)

Dark green oil (55%, 3.0 g); ^{1}H NMR (400 MHz, DMSO-d_6) δ 7.18 (t, J = 7.8 Hz, 1H), 6.74 (d, J = 8.1 Hz, 1H), 6.63 (t, J = 7.1 Hz, 1H), 3.97–3.91 (m, 1H), 3.65 (dd, J = 11.1, 4.5 Hz, 1H), 3.59 (dd, J = 11.2, 5.4 Hz, 1H), 3.49 (dd, J = 14.9, 5.2 Hz, 1H), 3.29 (dd, J = 14.9, 7.1 Hz, 1H); ^{13}C NMR (101 MHz, DMSO-d_6) δ 149.34, 129.43, 116.32, 112.40, 68.67, 56.19, 48.60; HRMS (ESI-QIT) m/z calcd for $C_{10}H_{15}ClNO^+$ [M+H$^+$]$^+$ 200.0837, found 200.1086; HRMS (ESI-QIT) m/z calcd for $C_{10}H_{14}ClNNaO^+$ [M+Na$^+$]$^+$ 222.0656, found 222.0811.

1-[(3-Bromobenzyl)(methyl)amino]-3-chloropropan-2-ol (12)

Colorless oil (51%, 3.9 g); ^{1}H NMR (400 MHz, CDCl$_3$) δ 7.39 (s, 1H), 7.37–7.31 (m, 1H), 7.21–7.09 (m, 1H), 3.95–3.89 (m, 1H), 3.62 (d, J = 5.5 Hz, 1H), 3.58 (s, 1H), 3.50 (d, J = 4.6 Hz, 2H), 2.56–2.47 (m, 3H), 2.22 (s, 3H); ^{13}C NMR (101 MHz, CDCl$_3$) δ 139.99, 132.02, 130.69, 130.08, 127.71, 122.49, 67.39, 61.88, 60.22, 47.18, 42.20; HRMS (ESI-QIT) m/z calcd for $C_{11}H_{16}BrClNO$ [M+H$^+$]$^+$ 292.0098, found 292.0002.

A.2.2. Determination of the activation energy

According to Arrhenius' equation, the activation energy has been calculated plotting the natural logarithm of the azetidinium salt formation as a function of $1/T$. The slope of the obtained line, interpolated in Excel, represents the $-E_a/R$ value, where R is the universal gas constant and E_a is the activation energy.

Chapter 3

A.3.1. Compounds Characterization

Glycerol (1)

^{1}H NMR (400 MHz, D_2O) δ 3.73 (tt, J = 6.4, 4.4 Hz, 1H), 3.60 (dd, J = 11.8, 4.4 Hz, 2H), 3.51 (dd, J = 11.7, 6.5 Hz, 2H).

Glycidol (3a)

^{1}H NMR (400 MHz, D_2O) δ 3.90 (dd, J = 12.8, 2.7 Hz, 1H), 3.49 (dd, J = 12.9, 5.8 Hz, 1H), 3.25 (ddt, J = 5.7, 4.3, 2.9 Hz, 1H), 2.91 (t, J = 4.4 Hz, 1H), 2.76 (dd, J = 4.3, 3.0 Hz, 1H).

Glycidyl tosylate (5)

^{1}H NMR (400 MHz, $CDCl_3$) δ 7.82 (d, J = 8.3 Hz, 2H), 7.43 – 7.34 (m, 2H), 4.95 (s, 3H), 4.27 (dd, J = 11.4, 3.5 Hz, 1H), 3.98 (dd, J = 11.4, 6.0 Hz, 1H), 3.29 – 3.16 (m, 1H), 2.86 – 2.80 (m, 1H), 2.61 (dd, J = 4.8, 2.6 Hz, 1H).

Chapter 4

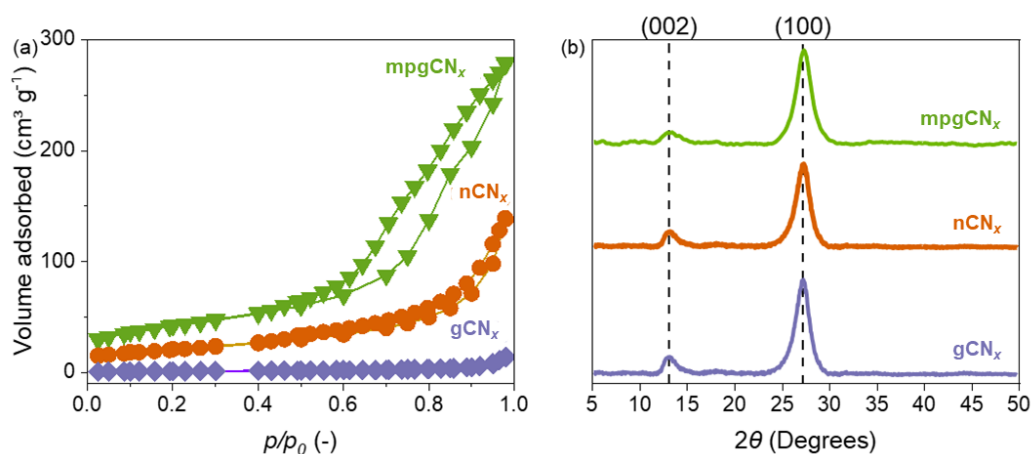## A.4.1. Characterization of metal-free CN_x

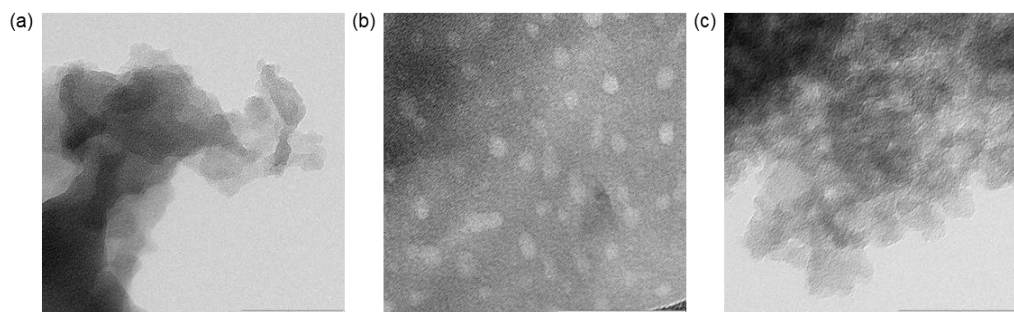**Figure A.4.1.** *N_2 physisorption (a) and X-ray diffraction (b) analysis of CN_x-based catalysts.*

Figure A.4.2. *HRTEM analysis of gCN_x (a), nCN_x (b), and $mpgCN_x$ (c).*

Table A.4.1. *Elemental composition and textural properties of CN_x-based catalysts.*

Catalyst	C^a (wt %)	N^a (wt %)	H^a (wt %)	C/N (-)	S_{BET}^b ($m^2\,g^{-1}$)	V_{pore}^c ($cm^3\,g^{-1}$)
gCN_x	34.84	56.65	1.10	0.61	5	0
nCN_x	32.15	47.92	2.12	0.67	72	0.21
$mpgCN_x$	31.90	48.75	2.43	0.65	157	0.46

^{a}CHNS. ^{b}N_2 isotherm collected at 77 K. ^{c}Quenched solid density functional theory model assuming

cylindrical-shaped pores.

A.4.2. Synthesis and characterization of metal-doped CN_x

Ag, Zn, and Cu-based $mpgCN_x$ preparation

To prepare $Zn@mpgCN_x$, $Cu@mpgCN_x$ and $Ag@mpgCN_x$ materials, a solution of the corresponding chlorinated salt (0.01 mol) in 10 mL of water was stirred with a solution 1 M of sodium tricyanomethanide (1.13 g, 0.01 mol; Sigma-Aldrich, 99%) in water (10 mL) for 3 h. The resulting mixture was centrifuged to obtain the metal tricyanomethanide as white solid after three washes with water. Solid cyanamide (3 g; Sigma Aldrich, 99%) and metal tricyanomethanide (0.15 mol) were added to SiO_2 Ludox HS40 with 12 nm particles (7.5 g; Sigma Aldrich, 40% aqueous dispersion) and heated under stirring for 16 h. The resulting white solid was heated for 8 h at 550 °C into an alumina crucible (heating ramp: 2.2 °C min^{-1}). The resulting yellow solid was added to a solution of NH_4HF_2 4.2 M (12 g in 50 mL of water; Sigma-Aldrich, 95%), mixed for 24 h, and centrifuged to obtain the product after three washes with water and ethanol.

Catalysts characterization

Porosity, pore distribution, and surface area data of the metal-doped materials were deduced via N_2 physisorption experiments (Figure A.4.3 a). The material crystallinity was evaluated through X-ray powder diffraction (XRD) studies. XRD spectra showed two characteristic diffraction peaks at $2\theta = 13°$ and $28°$, which, in accordance with the literature, correspond to the (100) and (002) planes, respectively (Figure A.4.3 b). The photoluminescence (PL) spectra (Figure A.4.3 c) were recorded using an FP-8300 fluorescence spectrometer, setting the excitation wavelength to 365 nm.
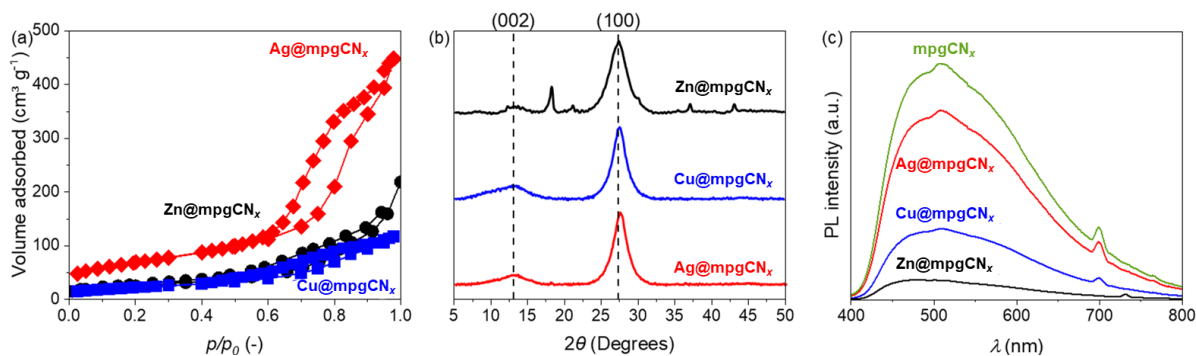
Figure A.4.3. *N_2 physisorption (a), X-ray diffraction (b), and photoluminescence (c) analysis of metal-doped CN_x catalysts.*
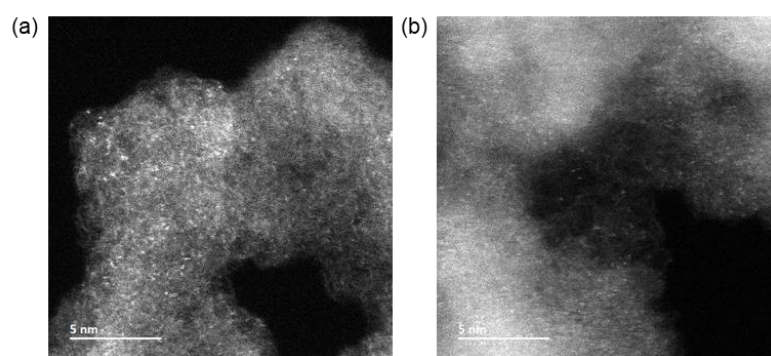

Figure A.4.4. *HRTEM analysis of Cu@mpgCN_x (a) and Ag@mpgCN_x (b).*

Table A.4.2. *Elemental composition and textural properties of metal-based CN_x catalysts.*

Catalyst	C[a] (wt %)	N[a] (wt %)	H[a] (wt %)	C/N (-)	Metal[b] (wt.%)	S_{BET}[c] (m² g⁻¹)	V_{pore}[d] (cm³ g⁻¹)
Zn@mpgCN_x	28.38	28.38	2.75	0.54	0.65	87	0.26
Cu@mpgCN_x	31.37	48.78	2.20	0.64	0.50	241	0.69
Ag@mpgCN_x	31.01	47.43	2.40	0.65	0.30	174	0.53

[a]CHNS. [b]ICP-OES [c]N_2 isotherm collected at 77 K. [d]Quenched solid density functional theory model assuming cylindrical-shaped pores.

A.4.3. Traditional photocatalytic set-up with LED stripes

A traditional photocatalytic set-up was assembled to operate the trifluoromethylation process. A LED stripe (length = 5 m) was wrapped around a transparent bottle (i.d. = 5 cm, length = 18 cm) and the blue light (457 nm, 18 W) irradiates the reaction flask placed inside the bottle.
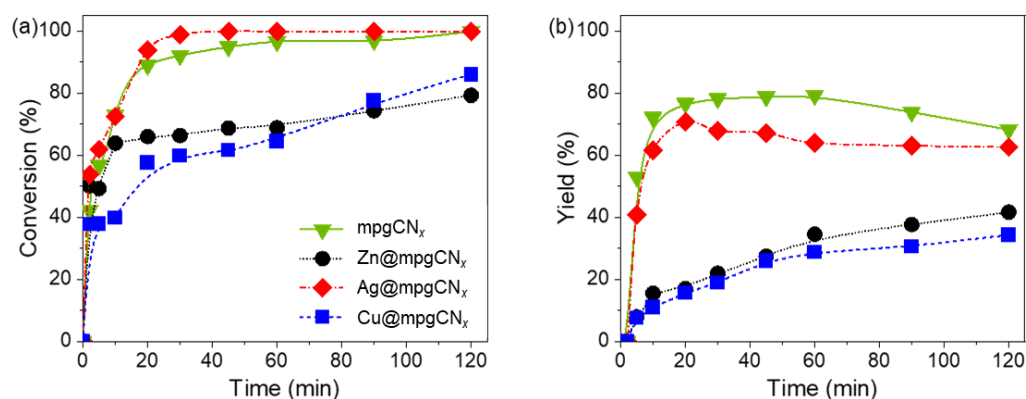
A.4.4. Photocatalytic tests

Figure A.4.5. *Synthesis of trifluoromethylpyrrole using different CN$_x$-based catalysts, showing conversion (a) and selectivity (b) trends over time. The color codes in (a) apply to (b). Reaction conditions: 1 (1 mmol), 2 (1.3 mmol), catalyst (100 mg), K$_2$HPO$_4$ (3 mmol), MeCN (8 mL), light source (PhotoCube™, blue light, λ = 457 nm), 45 °C, 1 atm.*
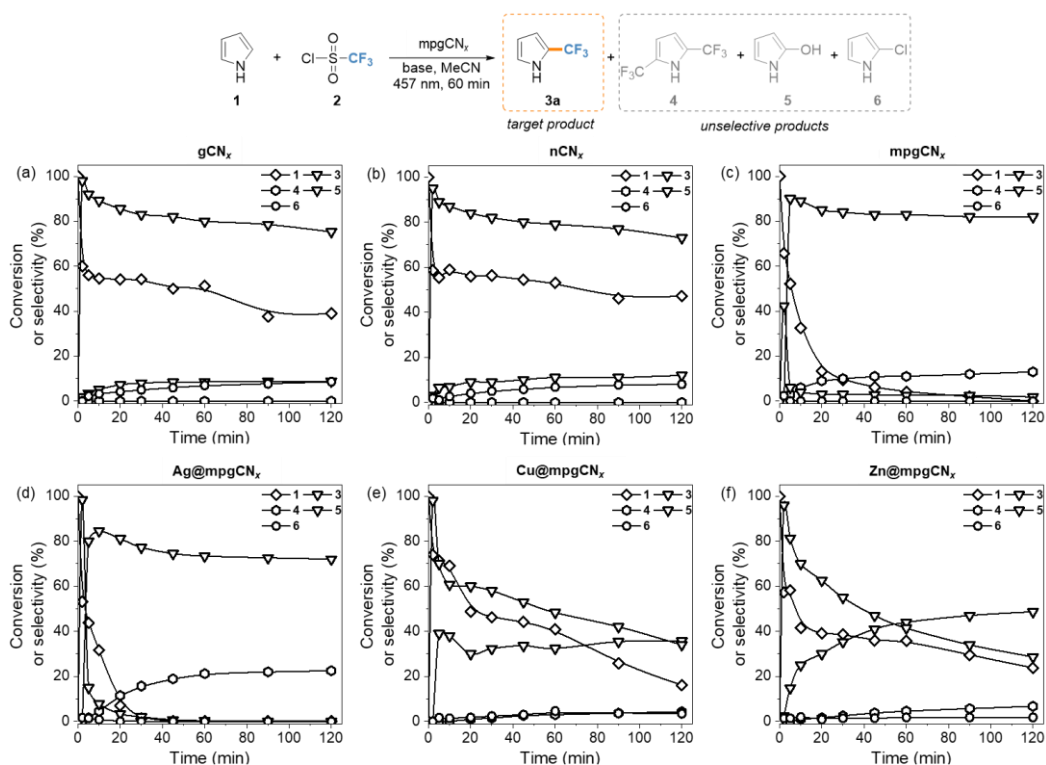

Figure A.4.6. *Synthesis of trifluoromethylpyrrole using different CN$_x$-based catalysts. Above, conversion and selectivity trends for metal-free catalysts, namely gCN$_x$ (a), nCN$_x$ (b), mpgCN$_x$ (c); below, conversion and selectivity trends for*

metal-doped catalysts, namely Ag@mpgCN$_x$ (d), Cu@mpgCN$_x$ (e), Zn@mpgCN$_x$ (f). Reaction conditions: 1 (1 mmol), 2 (1.3 mmol), catalyst (100 mg), K$_2$HPO$_4$ (3 mmol), MeCN (8 mL), light source (PhotoCube™, blue light, λ = 457 nm), 45 °C, 1 atm.

A.4.5. Comparison between batch and flow data

Table A.4.3. Vis-à-vis comparison between batch and flow synthesis of trifluoromethylpyrrole.

Entry	t (min)	Batch yield (%)[a]	Flow yield (%)[b]
1	10	23	72
2	20	77	77
3	30	64	78

[a]Carried out following the general procedure for batch synthesis: 1 (1 mmol), 2 (1.3 mmol), catalyst (100 mg), K$_2$HPO$_4$ (3 mmol), MeCN (8 mL), light source (PhotoCube™, blue light, λ = 457 nm), 45 °C. [b]Carried out following the general procedure for flow synthesis: 1 (1 mmol, 0.25 M in MeCN), TfCl (1,3 mmol, 0.25 M in MeCN), light source (PhotoCube™, blue light, λ = 457 nm), 45 °C, 1 bar, packed-bed reactor filled with mpgCN$_x$ (50 mg), K$_2$HPO$_4$ (3 mmol), and glass beads (2 g).
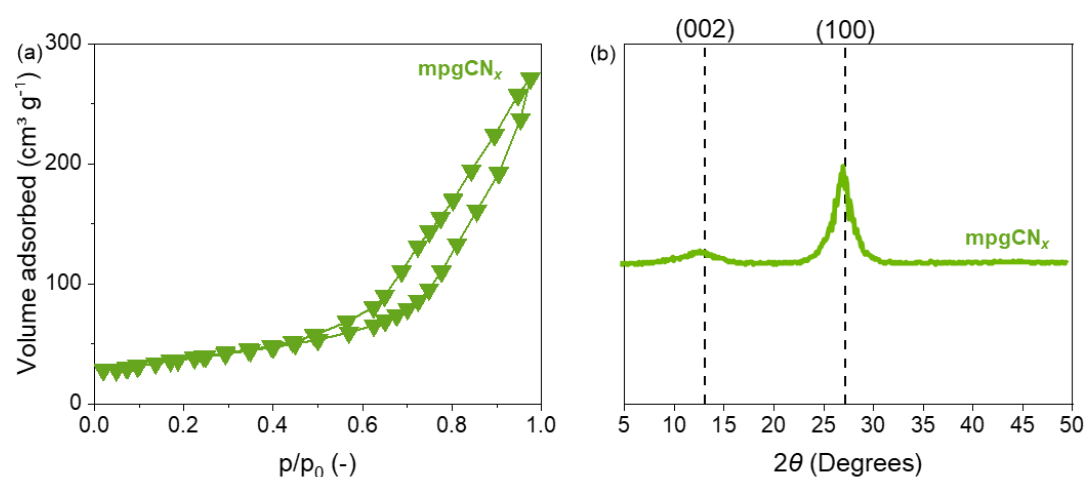
A.4.6. Catalyst characterization after usage

Figure A.4.7. N$_2$ physisorption (a) and X-ray diffraction (b) analysis of CN$_x$-based catalysts.

A.4.7. Compounds Characterization

2-(trifluoromethyl)-1H-pyrrole (or "trifluoromethylpyrrole", 3a)

^{1}H NMR (400 MHz, CD$_3$CN): δ 9.80 (s, 1H), 6.97 (dd, J = 4.0, 2.5 Hz, 1H), 6.61 (dd, J = 2.2, 1.1 Hz, 1H), 6.21 (t, J = 10.2 Hz, 1H). ^{19}F NMR (376 MHz, CD$_3$CN): δ -59.51 (s).

2-methyl-5-(trifluoromethyl)-1H-pyrrole (3b)

^{1}H NMR (400 MHz, CD$_3$CN): δ 5.85 – 5.81 (m, 1H), 5.78 – 5.73 (m, 1H), 2.19 – 2.17 (s, 3H). ^{19}F NMR (376 MHz, CD$_3$CN): δ -59.32 (s, J = 4.1 Hz).

methyl 2-(trifluoromethyl)-1H-pyrrole-3-carboxylate (3c)

^{1}H NMR (400 MHz, CD$_3$CN): δ 10.92 – 10.25 (m, 1H), 6.92 (t, J = 2.9 Hz, 1H), 6.69 (t, J = 3.0 Hz, 1H), 3.81 (s, 3H). ^{19}F NMR (376 MHz, CD$_3$CN): δ -60.48.

1-methyl-2-(trifluoromethyl)-1H-pyrrole (3d)

^{1}H NMR (400 MHz, CD$_3$CN): δ 6.88 (t, J = 2.0 Hz, 1H), 6.60 (dd, J = 2.0, 1.0 Hz, 1H), 6.14 – 6.10 (m, 1H), 3.74 (s, 3H). ^{19}F NMR (376 MHz, CD$_3$CN): δ -59.21 (s).

1-(methoxymethyl)-2-(trifluoromethyl)-1H-pyrrole (3e)

^{1}H NMR (400 MHz, CD$_3$CN): δ 7.12 – 7.06 (m, 1H), 6.70 (dt, J = 10.0, 5.1 Hz, 1H), 6.21 (dd, J = 7.5, 4.3 Hz, 1H), 5.31 (s, 2H), 3.26 (s, 3H). ^{19}F NMR (376 MHz, CD$_3$CN): δ -58.23 (s).

1-benzyl-2-(trifluoromethyl)-1H-pyrrole (3f)

^{1}H NMR (400 MHz, CD$_3$CN): δ 7.42 – 7.28 (m, 3H), 7.15 – 7.09 (m, 2H), 6.97 (t, J = 2.3 Hz, 1H), 6.71 – 6.65 (m, 1H), 6.22 (t, J = 3.3 Hz, 1H), 5.26 (s, 2H). ^{19}F NMR (376 MHz, CD$_3$CN): δ -59.52 (s).

1-phenyl-2-(trifluoromethyl)-1H-pyrrole (3g)

^{1}H NMR (400 MHz, CD$_3$CN): δ 7.47 – 7.42 (m, 4H), 7.41 – 7.33 (m, 1H), 7.04 (dd, J = 2.8, 1.9 Hz, 1H), 6.83 – 6.80 (m, 1H), 6.37 – 6.34 (m, 1H). ^{19}F NMR (376 MHz, CD$_3$CN): δ -59.52 (s).

2-(trifluoromethyl)-1H-pyrrol-1-amine (3h)

^{1}H NMR (400 MHz, CD$_3$CN): δ 6.93 – 6.86 (m, 1H), 6.49 – 6.43 (m, 1H), 6.06 – 6.00 (m, 1H). ^{19}F NMR (376 MHz, CD$_3$CN): δ -59.20.

tert-butyl 2-(trifluoromethyl)-1H-pyrrole-1-carboxylate (3i)

^{1}H NMR (400 MHz, CD$_3$CN): δ 7.52 (dd, J = 3.3, 1.9 Hz, 1H), 6.91 – 6.79 (m, 1H), 6.29 (t, J = 3.5 Hz, 1H), 1.62 (s, 9H). ^{19}F NMR (376 MHz, CD$_3$CN): δ -58.77.

2-(trifluoromethyl)-1H-indole (3l)

^{1}H NMR (400 MHz, CD$_3$CN): δ 7.63 – 7.58 (m, 1H), 7.54 (dd, J = 8.4, 0.7 Hz, 1H), 7.30 – 7.27 (m, 1H), 7.19 – 7.13 (m, 1H), 6.99 (dd, J = 5.8, 4.8 Hz, 1H). ^{19}F NMR (376 MHz, CD$_3$CN): δ -57.39 (s).

4-methyl-2-(trifluoromethyl)-1H-imidazole (3m)

^{1}H NMR (400 MHz, CD$_3$CN): δ 8.06 (s, 1H), 7.71 (s, 1H), 7.27 (s, 1H), 2.35 (d, J = 1.0 Hz, 9H). ^{19}F NMR (376 MHz, CD$_3$CN): δ -60.53 (s).
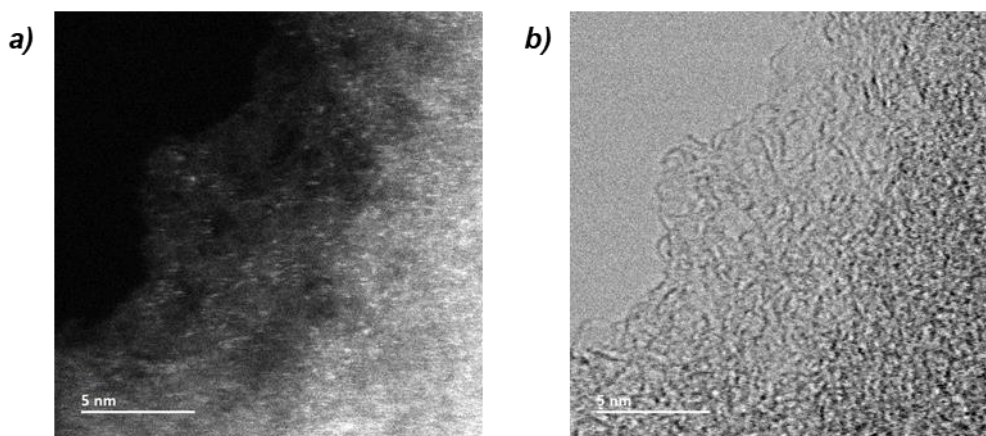
Chapter 5

A.5.1. Catalyst Characterization

Figure A.5.1. *High-resolution transmission electron micrograph (HR-TEM).*

A.5.2. Compounds Characterization

Benzaldehyde (2a)

Prepared according to the general procedure, using benzyl alcohol (19.5 mg, 0.18 mmol). The reaction was carried out for 4 h, affording the product in 69% yield and 100% conversion. ^{1}H NMR (400 MHz, CD$_3$CN): δ 10.04 (s, 1H), 7.95 – 7.90 (m, 2H), 7.74 – 7.68 (m, 1H), 7.64 – 7.58 (m, 2H).

4-nitrobenzaldehyde (2b)

Prepared according to the general procedure, using (4-nitrophenyl)methanol (27.6 mg, 0.18 mmol). The reaction was carried out for 6 h, affording the product in 20% yield and 89% conversion. ^{1}H NMR (400 MHz, CD$_3$CN): δ 10.10 (s, 1H), 8.34 (d, J = 8.7 Hz, 2H), 8.07 (d, J = 8.8 Hz, 2H).

benzo[d][1,3]dioxole-5-carbaldehyde (2c)

Prepared according to the general procedure, using benzo[d][1,3]dioxol-5-ylmethanol (27.4 mg, 0.18 mmol). The reaction was carried out for 6 h, affording

the product in 13% yield and 88% conversion. ^{1}H NMR (400 MHz, CD$_3$CN): δ 9.82 (s, 1H), 7.49 (dd, J = 8.0, 1.6 Hz, 1H), 7.32 (d, J = 1.6 Hz, 1H), 7.02 (d, J = 7.9 Hz, 1H), 6.11 (s, 2H).

4-methylbenzaldehyde (2d)

Prepared according to the general procedure, using *p*-tolylmethanol (22.0 mg, 0.18 mmol). The reaction was carried out for 6 h, affording the product in 37% yield and 90% conversion. ^{1}H NMR (400 MHz, CD$_3$CN): δ 9.97 (s, 1H), 7.81 (d, J = 8.1 Hz, 2H), 7.42 (d, J = 7.8 Hz, 2H), 2.46 (s, 3H).

3-(dimethylamino)benzaldehyde (2e)

Prepared according to the general procedure, using 3-(dimethylamino)phenylmethanol (27.2 mg, 0.18 mmol). The reaction was carried out for 6 h, affording the product in 13% yield and 69% conversion. ^{1}H NMR (400 MHz, CD$_3$CN): δ 8.50 (s, 1H), 7.41 (t, J = 7.7 Hz, 1H), 6.61 (d, J = 7.3 Hz, 2H), 6.53 – 6.47 (m, 1H), 3.08 (s, 6H).

2-phenylacetaldehyde (2f)

Prepared according to the general procedure, using 2-phenylethan-1-ol (22.0 mg, 0.18 mmol). The reaction was carried out for 14 h, affording the product in 13% yield and 31% conversion. ^{1}H NMR (400 MHz, CD$_3$CN): δ 10.04 (s, 1H), 7.76 – 7.69 (m, 1H), 7.64 – 7.59 (m, 2H), 7.43 – 7.35 (m, 2H), 3.71 (s, 2H).

thiophene-2-carbaldehyde (2g)

Prepared according to the general procedure, using thiophen-2-ylmethanol (20.5 mg, 0.18 mmol). The reaction was carried out for 6 h, affording the product in 40% yield and 85% conversion. ^{1}H NMR (400 MHz, CD$_3$CN): δ 9.96 (d, J = 1.3 Hz, 1H), 8.12 – 7.83 (m, 1H), 7.46 – 7.19 (m, 1H), 7.00 (s, 1H).

furan-2-carbaldehyde (2h)

Prepared according to the general procedure, using furan-2-ylmethanol (16.6 mg, 0.18 mmol). The reaction was carried out for 12 h, affording the product in 40% yield and 85% conversion. ^{1}H NMR (400 MHz, CD$_3$CN): δ 9.63 (d, J = 0.8 Hz, 1H), 7.87 – 7.81 (m, 1H), 7.38 (dd, J = 3.6, 0.8 Hz, 1H), 6.70 (dd, J = 3.6, 1.7 Hz, 1H).

Picolinaldehyde (2i)

Prepared according to the general procedure, using pyridin-2-ylmethanol (19.6

mg, 0.18 mmol). The reaction was carried out for 6 h, affording the product in 26% yield and 89% conversion. ^{1}H NMR (400 MHz, CD$_3$CN): δ 10.04 (d, J = 0.8 Hz, 1H), 8.82 (d, J = 4.8 Hz, 1H), 8.03 – 7.92 (m, 2H), 7.68 – 7.59 (m, 1H).

Acetophenone (2l)

Prepared according to the general procedure, using 1-phenylethan-1-ol (22.0 mg, 0.18 mmol). The reaction was carried out for 6 h, affording the product in 33% yield and 93% conversion. ^{1}H NMR (400 MHz, CD$_3$CN): δ 8.04 – 7.95 (m, 2H), 7.69 – 7.58 (m, 1H), 7.58 – 7.50 (m, 2H), 2.60 (s, 3H).

Chapter 6

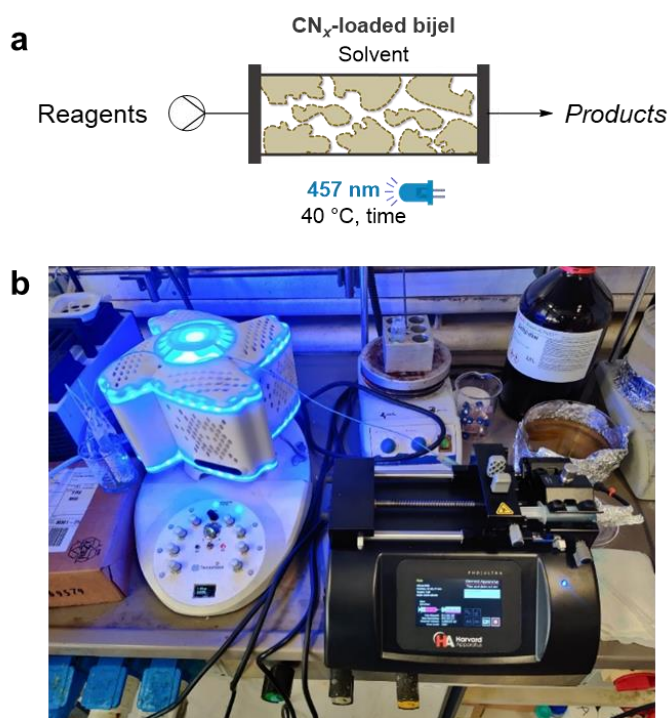## A.6.1. Preparation of photocatalytic reactor

Figure A.6.1. *Schematic representation (a) and picture (b) of the photocatalytic flow set-up.*

A.6.2. Materials characterization

Table A.6.1. *Elemental composition and textural properties of CN$_x$-based catalysts.*

Catalyst	C^a (wt %)	N^a (wt %)	H^a (wt %)	C/N (-)	Metal^b (wt.%)	S_{BET}^c ($m^2 g^{-1}$)	V_{pore}^d ($cm^3 g^{-1}$)
gCN$_x$	34.84	56.65	1.10	0.61	-	5	0
mpgCN$_x$	31.90	48.75	2.43	0.65	-	157	0.46
Mn@mpgCN$_x$	30.99	53.59	3.11	0.58	0.18	-	-
Zn@mpgCN$_x$	28.38	28.38	2.75	0.54	0.65	87	0.26

Ni@mpgCN$_x$	32.77	53.84	1.69	0.61	1.08	-	-

[a]CHNS. [b]ICP-OES [c]N$_2$ isotherm collected at 77 K. [d]Quenched solid density functional theory model assuming cylindrical-shaped pores.
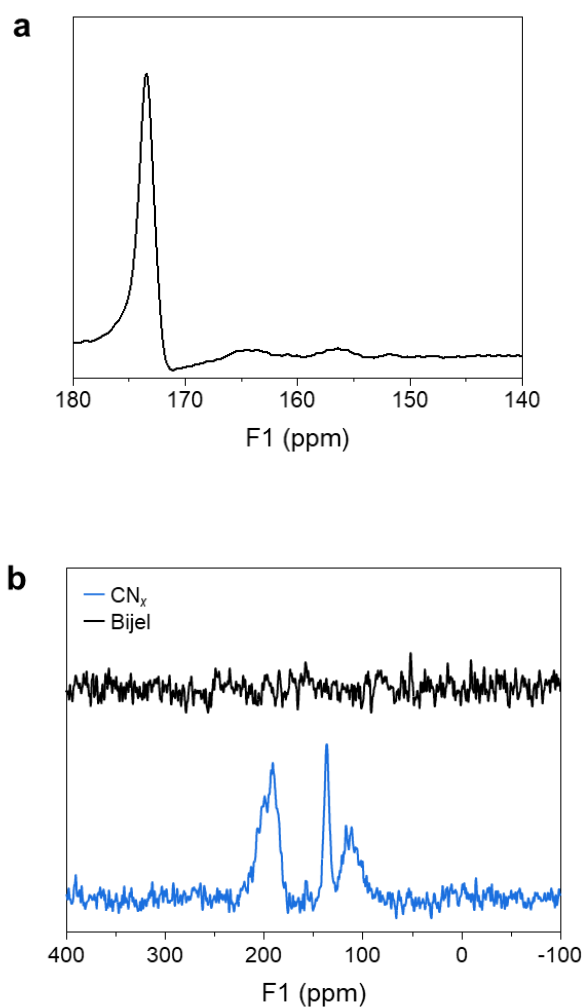

Figure A.6.2. *Zoomed region (180 – 140 ppm) of the* ^{13}C *CP-MAS NMR spectrum of bijel, highlighting the presence of carbon nitride within the bijel structure (a). Solid-state* ^{15}N *CP-MAS NMR spectra of CN$_x$ (in blue) and bijel structure (in black) (b).*
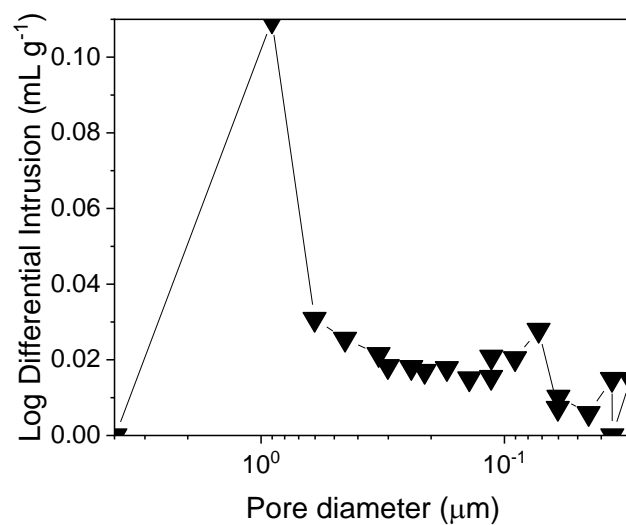
Figure A.6.3. *Porosimetry test on the prepared polymeric material.*

A.6.3. Control experiments

Table A.6.2. *Reaction scheme: standard conditions and control experiments.*
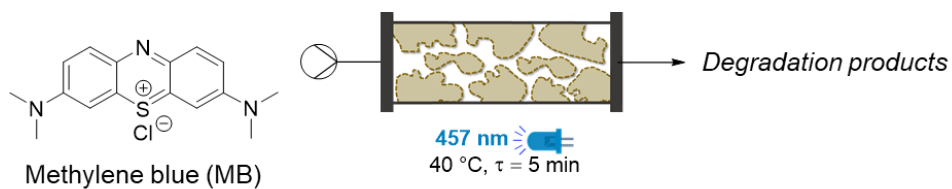
Entry	Control experiment	Degradation[d] (%)
1.	100 μM[a,b]	50
2.	No photocatalyst[a,c]	-
3.	As shown[a,b,c]	85

[a]Photoreactor set to blue light irradiation. [b]mpgCN$_x$ used as photocatalyst. [c]MB concentration = 44 μM. [d]Conversion and yield were computed via GC, with a calibration curve.

A.6.4. Control experiments

CFD simulations were carried out by means of the Ansys Fluent 19.1 suite of programs. The geometry is shown in Figure S6 and it consists of a cylindrical reactor with a diameter equal to D=0.5 cm and a height equal to H=8 cm; to reproduce the disordered geometry of the sponge, starting from the TEM images of Figure 6.3 b, the geometry was reproduced by a series of channels of various shape and diameters.
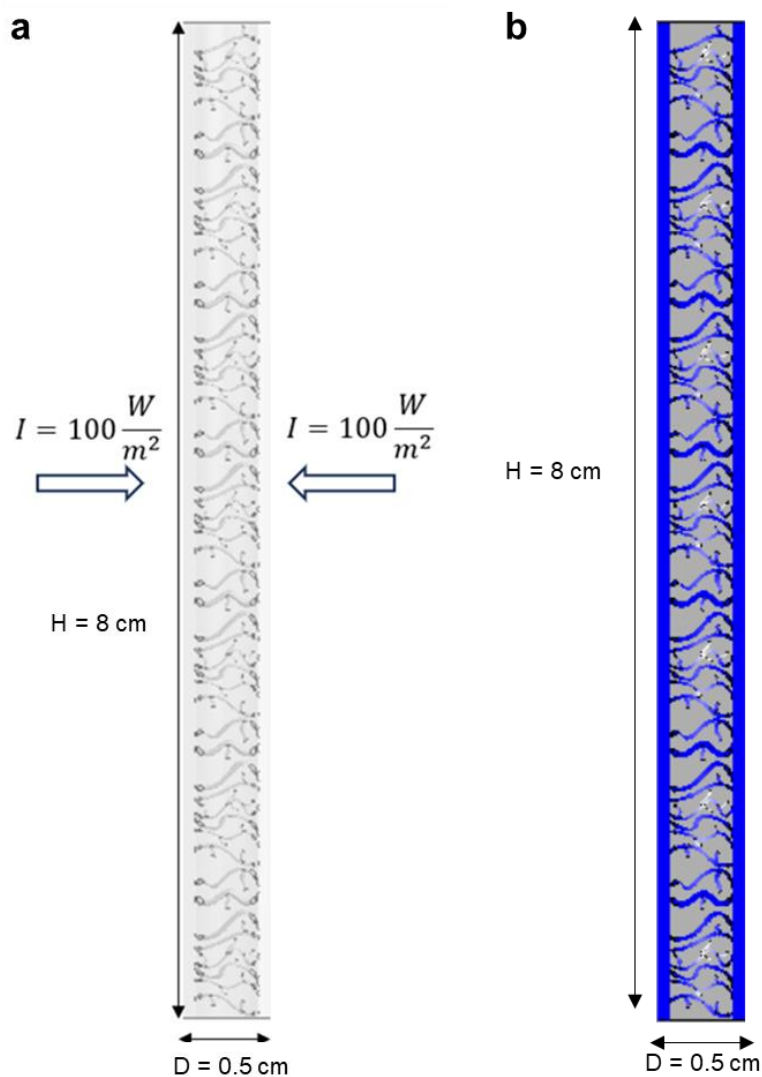

Figure A. 6.4. *Schematic representation of the reactor geometry (a) and light distribution inside the reactor (b).*

To study the light distribution inside the photoreactor it is necessary to solve the radiant transfer equation (RTE):

$$\frac{dI(\vec{r},\vec{s})}{ds} + (k + \sigma_s)I(\vec{r},\vec{s}) = kn^2\frac{\sigma T^4}{\pi} + \frac{\sigma_s}{4\pi}\int_0^{4\pi} I(\vec{r},\vec{s}')\,\Phi(\vec{s}\cdot\vec{s}')d\Omega'$$

where $\vec{\sigma}$ and $\vec{r}$ are the position vectors, $\vec{\sigma}'$ is the scattering direction vector, s is the path length, n is the refracting index, σ_s is the scattering coefficient, k is the absorption coefficient, σ is the Stefan-Boltzmann constant, I is the radiation intensity, T is the local temperature, Φ is the phase function and Ω' is the solid angle. Among the various methods available to solve the RTE, the Discrete Ordinate Model (DOM) was chosen because of its enhanced accuracy. This method solves the RTE dividing by a finite number of discrete solid angles, each associated with a vector direction fixed in the global Cartesian system $(\vec{x},\vec{y},\vec{z})$. To avoid undesired phenomena such as the ray effect and angle overhanging, a sufficiently high value of angular discretization and pixelization must be chosen; from previous works, it was found that a value of angular discretization equal to 8x8 and pixelization equal to 3x3 suffices to ensure reliable results. The external walls of the domain are modelled as semi-transparent and with an incoming diffusive irradiation equal to $I = 100\frac{W}{m^2}$.

A.6.5. Compounds Characterization

Benzaldehyde

Prepared according to the General Procedure B, affording the product in 27% yield. ^{1}H NMR (400 MHz, CD$_3$CN): δ 10.04 (s, 1H), 7.95 – 7.90 (m, 2H), 7.74 – 7.68 (m, 1H), 7.64 – 7.58 (m, 2H).

***p*-aminobenzonitrile**

Prepared according to the General Procedure C, affording the product in 24% yield. ^{1}H NMR (400 MHz, CDCl$_3$): δ 7.67 – 7.58 (m, 2H), 6.62 – 6.55 (m, 2H).

N-benzyl-1-phenylmethanimine

Prepared according to the General Procedure D, affording the product in 30%

yield. ^{1}H NMR (400 MHz, CD$_3$CN): δ 8.50 (s, 1H), 7.88 – 7.49 (m, 2H), 7.40 – 7.33 (m, 8H), 4.80 (s, 2H).

Chapter 7

A.7.1. Purification process parameters

Table A.7.1. *Buffer concentration for purification process.*

Phase	Buffer
Equilibration	40% CH_3CN, 60% 14 mM Na_2CO_3
Loading	40% CH_3CN, 60% 14 mM Na_2CO_3
Washing	100% 14 mM Na_2CO_3
Elution	100% CH_3CN
Storage	40% CH_3CN, 60% 14 mM Na_2CO_3

A.7.2. Reaction oprimization
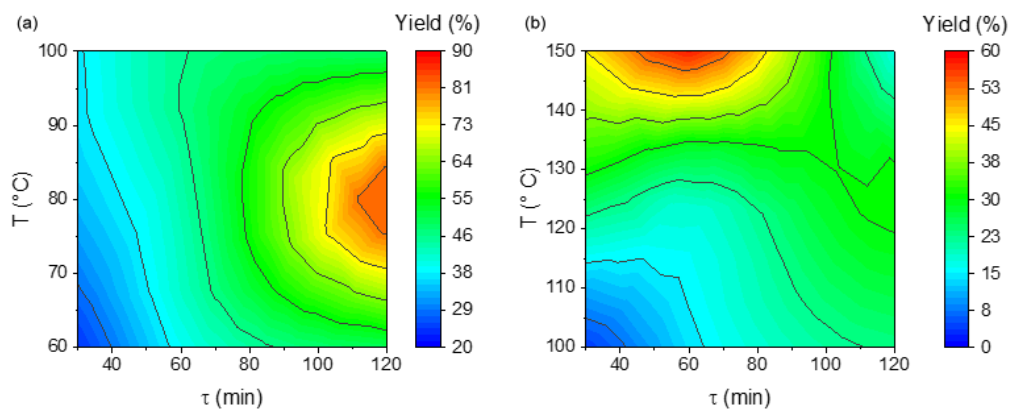
Figure A.7.1. *Contour plot showing the influence of temperature (T) and residence time (t) on the yield of phenylboronic acid (a) and biphenyl (b). As shown in this contour plot, several experiments were performed to optimize the two reactions under flow conditions. Analysis of the collected data allowed us to generate the contour map reported in this figure. In particular, the highest yields of phenylboronic acid **2** (a) could be obtained at longer residence times (120 min) and at relatively low temperature (80 °C). In fact, increasing the temperature*

*above this value, and reaching 100 °C, competitive formation of side products could be observed. The optimization of the Suzuki cross-coupling reaction has been conducted between 100 and 150 °C (b), finding the optimum with a temperature of 150 °C and a residence time of 60 min. Lowering temperatures resulted in a substantial decrease of product yield. Moreover, increasing the residence time above 80 min provided biphenyl **3** in remarkable lower yield, probably due to concurrent degradation mechanisms.*

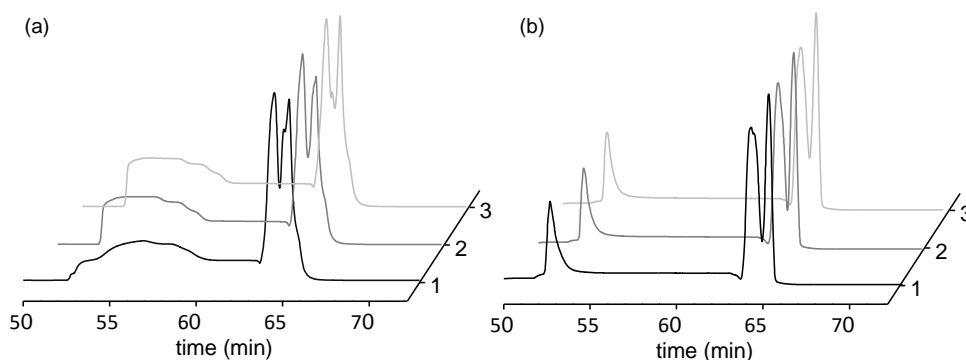## A.7.3. Continuous purification process

Figure A.7.2. *Superimposed wash and elution phases of the chromatograms obtained from the continuous chromatography for aminoalcohol (a) and diphenylether (b). To show the broad applicability of the integrated synthesis-purification method, two additional small molecules, aminoalcohol and diphenylether, were synthesized and purified. In each batch purification, the breakthrough of the product was not observed during the load phase, which indicated the complete adsorption of the product. The wash phase was then operated with a step gradient of 50% acetonitrile to remove weakly bound impurities. Lastly, the elution phase with a step gradient of 100% acetonitrile desorbed the product completely, which was then analyzed with at-line HPLC on a C18 column (see Experimental section) to determine the purity and concentration. To assess the benefits introduced by a continuous process, the continuous chromatographic process was applied to the two molecules. The*

process parameters implemented in the continuous process are reported above. Since, after completion, the columns are brought back to their initial states, multiple cycles can be performed consecutively to realize a periodically continuous process. The superimposed UV traces of the first column for three cycles in the wash and elution phases are shown here. Despite differences in the crude loaded, the elution profiles of the two molecules resembled each other in terms of the desorption of the weakly bound impurity at 54 min and that of the product at 70 min. Such good overlay of the product elution profile indicates that the continuous operation reached a steady state.

Table A.7.2. *Comparison between batch and continuous purification processes (Product **4**).*

	Solvent consumption (L g^{-1})	Yield (%)	Productivity (g h^{-1} L^{-1})	Purity (%)
Batch	3.1	64	5.6	92
Continuous	2.4	68	7.5	92

Table A.7.3. *Comparison between batch and continuous purification processes (Product **5**).*

	Solvent consumption (L g^{-1})	Yield (%)	Productivity (g h^{-1} L^{-1})	Purity (%)
Batch	3.4	77	6.0	97
Continuous	2.4	71	7.1	92

A.7.4. Circularity analysis

Table A.7.4. *Circularity summary per 100 mg of purified biphenyl. The process is analysed for three designs, including both synthesis and purification in batch (Batch+Batch), continuous synthesis followed by a batch purification (Conti+Batch), and continuous synthesis and purification (Conti+Conti). For each design two scenarios are proposed: (A) not considering reactant recycling; (B) considering reactant recycling.*

Appendix A

Indicator[1]	Using chloride derivatives						Using bromide derivatives						Using Iodine derivatives					
	Batch + Batch		Conti + Batch		Conti + Conti		Batch + Batch		Conti + Batch		Conti + Conti		Batch + Batch		Conti + Batch		Conti + Conti	
	A	B	A	B	A	B	A	B	A	B	A	B	A	B	A	B	A	B
M (mg)[a]	3071	3071	1463	1463	1323	1323	3326	3326	1661	1661	1447	1447	3586	3586	1863	1863	1574	1574
F_R[b]	0.00	0.17	0.52	0.75	0.68	0.81	0.00	0.18	0.46	0.68	0.62	0.75	0.00	0.19	0.41	0.63	0.57	0.71
V (mg)[c]	3071	2548	697	369	426	257	3326	2733	895	526	550	355	3586	2921	1097	685	677	455
C_U[d]	0.00	0.17	0.52	0.75	0.68	0.81	0.00	0.18	0.46	0.68	0.62	0.75	0.00	0.19	0.41	0.63	0.57	0.71
E_F[e]	1.00	1.00	1.00	1.00	1.00	1.00	1.00	1.00	1.00	1.00	1.00	1.00	1.00	1.00	1.00	1.00	1.00	1.00
W (mg)[f]	2971	2449	597	269	326	157	3226	2633	795	425	450	255	3491	2826	1000	588	580	358
LFI[g]	0.98	0.81	0.44	0.22	0.28	0.16	0.98	0.81	0.51	0.29	0.35	0.21	0.99	0.80	0.56	0.34	0.40	0.26
$F(X)$[h]	0.9	0.9	0.9	0.9	0.9	0.9	0.9	0.9	0.9	0.9	0.9	0.9	0.9	0.9	0.9	0.9	0.9	0.9
MCI[i]	0.115	0.268	0.602	0.804	0.744	0.859	0.114	0.274	0.542	0.742	0.689	0.810	0.112	0.279	0.493	0.693	0.641	0.768

[a]Mass load entering the process (M); [b]recycled fraction (FR); [c]use of virgin materials (V); [d]reuse fraction (CU); [e]extraction efficiency (EF); [f]unrecoverable waste (W); [g]linear flow indicator (LFI); [h]utility factor F(X); [i]material circular indicator (MCI).

A.7.1. Compounds Characterization

Phenylboronic acid (2)

^{1}H NMR (400 MHz, CDCl$_3$) δ 8.19 – 8.12 (d, 2H), 7.55 – 7.45 (t, 1H), 7.45 – 7.37 (t, 2H).; ^{13}C NMR (101 MHz, CDCl$_3$) δ 135.66, 133.48, 132.71, 131.23, 128.03.

Biphenyl (3)

^{1}H NMR (400 MHz, CDCl$_3$) δ 7.56 – 7.47 (d, 2H), 7.37 (t, 2H), 7.32 – 7.22 (t, 1H); ^{13}C NMR (101 MHz, CDCl$_3$) δ 141.31, 128.81, 127.30, 127.22.

1,3-bis[methyl(phenyl)amino]propan-2-ol (4)

^{1}H NMR (400 MHz, DMSO-d_6) δ 7.16 – 7.05 (t, 4H), 6.69 – 6.62 (d, 4H), 6.57 (t, 2H), 4.93 (d, 1H), 4.01 (m, 1H), 3.41 (dd, J = 14.8, 4.7 Hz, 2H), 3.22 (dd, J = 14.8, 7.5 Hz, 2H), 2.96 (s, 6H); ^{13}C NMR (101 MHz, DMSO-d_6) δ 149.33, 129.42, 129.40; 116.35, 112.41, 68.68, 65.19, 48.60.
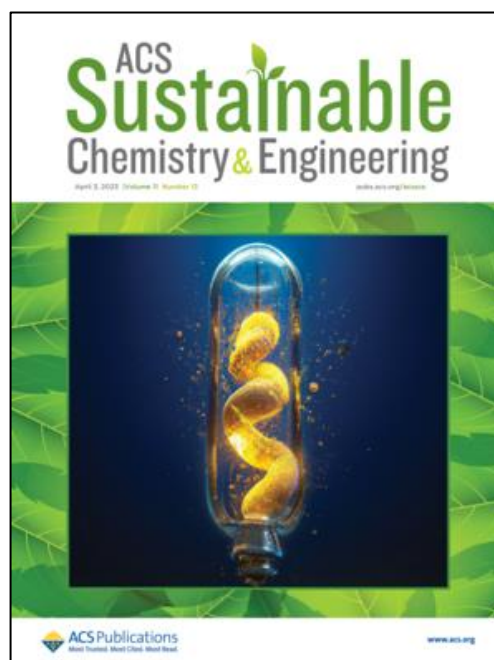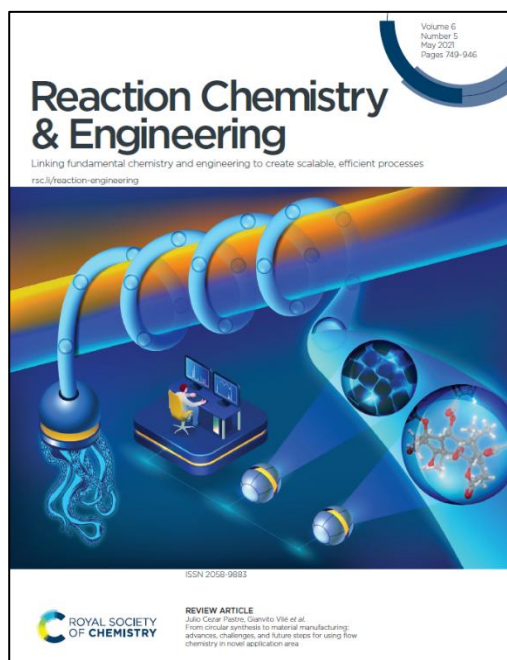
Diphenyl ether (5)

^{1}H NMR (400 MHz, CDCl$_3$) δ 7.30 – 7.22 (t, 4H), 7.06 – 6.99 (t, 2H), 6.97 – 6.91 (d, 4H); ^{13}C NMR (101 MHz, CDCl$_3$) δ 157.01, 128.40, 121.82, 118.81.

Appendix B

Cover Gallery

The work embodied in this thesis has been selected and featured on the front cover of several journals. The created artworks are collected in this page.

Appendix C

Curriculum Vitae

PERSONAL INFORMATION

Name	Alessandra Sivo
Date of birth	March 01st, 1995
Place of birth	Bitonto, Italy
Nationality	Italian
E-mail	alessandra.sivo@polimi.it
ORCID	0000-0003-0641-8590

EDUCATION

2020 - 2023	Doctoral studies in Industrial Chemistry and Chemical Engineering
	Department of Chemistry, Materials, and Chemical Engineering "Giulio Natta", Politecnico di Milano, Italy
	Thesis title: "Novel methodologies for the flow synthesis of organic scaffolds"
	PhD advisor: Prof. Gianvito Vilé

2014 - 2020   Master's Degree in Medicinal Chemistry, 110/110

Department of Pharmaceutical Sciences, University of Bari "A. Moro", Italy

Thesis title: "Flow synthesis of chloroaldehydes via lithium dihalocarbenoid"

Advisors: <u>Prof. Renzo Luisi</u>, <u>Prof. Leonardo Degennaro</u>

VISITING PERIODS

2022   Visiting PhD Student in the group of <u>Prof. Timothy Noël</u>

Van't Hoff Institute for Molecular Sciences, University of Amsterdam, The Netherlands

FELLOWSHIPS AND AWARDS

2022   Scholarship, XXII National Congress on Catalysis 2022

2022   Erasmus Scholarship, European Union

2020-2023   PhD Scholarship, Bracco Imaging spa

SUPERVISION OF GRADUATE STUDENTS

2020 - 2023   Supervisor of 13 Master Thesis students in Chemical Engineering

Department of Chemistry, Materials, and Chemical Engineering "Giulio Natta", Politecnico di Milano, Italy

REVIEWING ACTIVITIES

Reviewer   Green Processes and Synthesis

Chemical Engineering and Processing: Process Intensification

Catalysis Science & Technology

Appendix D

List of Publications

Doctoral Publications

M. A. Bajada, G. Di Liberto, S. Tosoni, V. Ruta, L. Mino, N. Allasia, **A. Sivo**, G. Pacchioni, G. Vilé. "Light-driven C–O coupling of carboxylic acids and alkyl halides over a Ni single-atom catalyst". *Nat. Synth* **2023**. DOI: 10.1038/s44160-023-00341-3.

L. Wesenberg, **A. Sivo**, G. Vilé, T. Noël. "Ni-catalyzed electro-reductive cross-electrophile couplings of alkyl amine-derived radical precursors with aryl iodides". *J. Org. Chem.* **2023**. DOI: 10.1021/acs.joc.3c00859.

A. Sivo, V. Ruta, V. Granata, A. Savateev, M. A. Bajada, G. Vilé. "Nanostructured Carbon Nitride for Continuous-Flow Trifluoromethylation of (Hetero)Arenes". *ACS Sustainable Chem. Eng.* **2023**, *13*, 5284–5292 (Selected *Front Cover*).

V. Ruta, **A. Sivo**, L. Bonetti, M.A Bajada, G. Vilé. "Structural effects of metal single-atom catalysts for enhanced photocatalytic degradation of Gemfibrozil". *ACS Appl. Nano Mater.* **2022**, *5*, 14520-14528.

A. Sivo, T. K. Kim, V. Ruta, R. Luisi, J. Osorio-Tejada, M. Escriba-Gelonch, V. Hessel, M. Sponchioni, G. Vilé. "Enhanced flow synthesis of small molecules by in-line integration of sequential catalysis and benchtop twin-column continuous chromatography". *React. Chem. Eng*. **2022**, *7*, 2650-2658 (Selected for the

Emerging Investigators Series).

G. Vilé, G. Di Liberto, S. Tosoni, **A. Sivo**, V. Ruta, M. Nachtegaal, A. Clark, S. Agnoli, Y. Zou, A. Savateev, M. Antonietti, G. Pacchioni. "Azide-alkyne click chemistry over a heterogeneous copper-based single-atom catalyst". *ACS Catal.* **2022**, *12*, 2947-2958.

A. Sivo, V. Ruta, G. Vilé. "Gram-scale domino synthesis in batch and flow mode of azetidinium salts". *J. Org. Chem.* **2021**, *86*, 14113-14120 (Special Issue *'Enabling Techniques for Organic Synthesis'*; Highlighted in *Synfacts* **2022**, *18*, 0221).

A. Sivo, N. Manfredini, J. M. G. Alcântara, J. Ilare, M. Maraldi, D. Moscatelli, G. Vilé. "Flow chemistry e catalisi "a singolo sito attivo". Risorse per la sintesi farmaceutica". *La Chimica e l'Industria* **2021**, DOI: 10.17374/CI.2021.103.1.28.

A. Sivo, R. Souza Galaverna, G. Rodrigues Gomes, J.C. Pastre, G. Vilé. "From circular applications to materials manufacturing: advances, challenges, and future steps for using flow chemistry in novel application areas". *React. Chem. Eng.* **2021**, *6*, 756-786 (Invited *Front Cover*).

Pre-Doctoral Publications

P. Musci, M. Colella, **A. Sivo**, G. Romanazzi, R. Luisi, L. Degennaro. "Flow Microreactor Technology for Taming Highly Reactive Chloroiodo-methyllithium Carbenoid: Straightforward and Chemoselective Synthesis of α-Chloroaldehydes". *Org. Lett.* **2020**, *22*, 3623-3627.

Appendix **E**

List of Presentations

A. Sivo, V. Ruta, M.A Bajada, G. Vilé. "Polymeric Microphotoreactor Functionalized with Carbon Nitride for Continuous-Flow Organic Synthesis". The 15th European Congress on catalysis (August 2023) – *Oral Presentation.*

A. Sivo, V. Ruta, M.A Bajada, G. Vilé. "Polymeric Microphotoreactor Functionalized with Carbon Nitride for Continuous-Flow Organic Synthesis". The 28th North American Catalysis Society Meeting (June 2023) - *Oral Presentation.*

A. Sivo, G. Vilé. "Metal-free mesoporous graphitic carbon nitride for visible-light-driven photoredox trifluoromethylation of (hetero)aromatics under flow conditions". New trends in organic synthesis 2022 - XXXVI SYMPOSIUM (November 2022) - *Poster Presentation.*

A. Sivo, G. Vilé. "Metal-free mesoporous graphitic carbon nitride for visible-light-driven photoredox trifluoromethylation of (hetero)aromatics under flow conditions". 19th edition of Ischia Advanced School of Organic Chemistry (September 2022) - *Poster Presentation.*

A. Sivo, G. Vilé. "Metal-free mesoporous graphitic carbon nitride for visible-light-driven photoredox trifluoromethylation of (hetero)aromatics under flow conditions". XXII National Congress on Catalysis - GIC 2022 (September 2022) - *Oral Presentation* (funded by the "Interdisciplinary catalysis group" of the Italian chemical society).

A. Sivo, V. Ruta, G. Vilé. "Metal-free mesoporous graphitic carbon nitride for visible-light-driven photoredox trifluoromethylation of (hetero)aromatics under flow conditions". 8th EuChemS Chemistry Congress (August 2022) - *Poster Presentation.*

A. Sivo, V. Ruta, G. Vilé. "Integrating 'single-atom' catalysis with flow chemistry and continuous chromatography for greener Suzuki cross-couplings". 13th European Congress of Chemical Engineering and 6th European Congress of Applied Biotechnology (September 2021) - *Oral presentation.*

A. Sivo, V. Ruta, G. Vilé. "A novel and automated continuous-flow platform for the sustainable and integrated synthesis of azetidinium salts". 13th European Congress of Chemical Engineering and 6th European Congress of Applied Biotechnology (September 2021) - *Oral presentation.*